

Double helicity asymmetry of inclusive neutral pion production in polarized pp collisions at $\sqrt{s} = 62.4$ GeV

Kazuya Aoki



A dissertation submitted in partial fulfillment of
the requirements for the degree of Doctor of Science



Abstract

We present the results of double helicity asymmetry A_{LL} of inclusive π^0 production in polarized pp collisions at $\sqrt{s} = 62.4$ GeV.

Polarized lepton-nucleon deep-inelastic scatterings (DIS) have revealed that the quark spin carries only $\sim 25\%$ of the proton spin, which contradict our naive expectation. It stimulated various effort towards the understanding of the proton spin. Despite of the wide effort, there remains large uncertainty especially on gluon spin contribution to the proton. The double helicity asymmetry A_{LL} of π^0 production in polarized pp collisions is sensitive to the gluon contribution to the proton since the production is dominated by quark-gluon and gluon-gluon scatterings in the initial protons. The gluons interact at leading order in these processes unlike the DIS where gluons only contribute through higher order.

The measurement was performed with the PHENIX detector at the Relativistic Heavy Ion Collider (RHIC) at Brookhaven National Laboratory (BNL) in the United States in Run 2006. The polarized proton beams collided at $\sqrt{s} = 62.4$ GeV at RHIC and the integrated luminosity of analyzed data sample is 40 nb^{-1} with an average polarization of 48%. We have measured π^0 via two photon decay, $\pi^0 \rightarrow \gamma\gamma$, and the decay photons were detected with electromagnetic calorimeters (EMCal) of the PHENIX detector.

The measured kinematic range for A_{LL} of π^0 is $p_T = 1 - 4 \text{ GeV}/c$, over a pseudorapidity range of $|\eta| < 0.35$. The probed Bjorken x roughly scales with $x_T = 2p_T/\sqrt{s}$. Thus the results probe the higher range of Bjorken x of the gluon, x_g , with better statistical precision than our previous measurements at $\sqrt{s} = 200$ GeV in Run 2005. The measurements are sensitive to the gluon polarization in the proton for $0.06 < x_g < 0.4$. The measured A_{LL} is consistent with zero within the uncertainties. The data do not support a large gluon polarization scenario, such as GRSV-max. The results were included in recent global analysis of polarized PDFs by the DSSV group. An truncated integral of $\Delta g(x)$ was obtained to be $\int_{0.001}^1 \Delta g(x) dx = 0.013_{-0.120}^{+0.106}$ for $\Delta\chi^2 = 1$. The uncertainties are much smaller than the range previously allowed by the analysis which only includes DIS data.

In addition to A_{LL} , the cross sections of π^0 production were measured to confirm the applicability of perturbative QCD (pQCD) framework which the argument of Δg extraction is based on. The results are consistent with the pQCD calculation. Single spin asymmetry A_L , which is expected to be negligible at $\sqrt{s} = 62.4$ GeV was measured and was consistent with zero within the uncertainties. Double transverse spin asymmetry A_{TT} was measured to obtain a systematic uncertainty which come from the residual transverse components of the beam polarizations. The maximal possible A_{TT} effect on A_{LL} was found to be $< 0.15 \cdot \delta A_{LL}$, where δA_{LL} denotes the statistical uncertainty of A_{LL} .

Contents

1	Introduction	1
2	Physics	4
2.1	π^0 production in pp collisions	4
2.2	Deep inelastic scattering formalism	6
2.3	DGLAP equations and factorization	9
2.4	Factorization theorem	13
2.5	Sum rules for PDFs	14
2.5.1	Sum rules for unpolarized PDFs	14
2.5.2	Sum rule for polarized PDFs	14
2.6	Unpolarized PDFs	15
2.7	Polarized PDFs	16
2.8	Probing Δg in polarized pp collisions	20
2.9	x_T and probed x range	21
3	Experimental Setup	25
3.1	Overview	25
3.2	Relativistic Heavy Ion Collider (RHIC)	25
3.2.1	Polarized proton source	29
3.2.2	Polarization of proton beams	30
3.2.3	Polarimeters	36
3.3	PHENIX overview	39
3.4	PHENIX global detectors	44
3.4.1	Beam Beam Counter (BBC)	44
3.4.2	Zero Degree Calorimeter (ZDC) and shower max detector (SMD)	46
3.5	PHENIX central arms	50
3.5.1	Electromagnetic calorimeter (EMCal)	50
3.5.2	EMCal front end electronics	56
3.6	PHENIX trigger system	58
3.7	PHENIX DAQ system	58

4	Analysis	60
4.1	Overview	60
4.2	Run selection	61
4.3	Beam polarization	63
4.4	Relative Luminosity	64
4.4.1	Overview	65
4.4.2	Bunch selection criteria	65
4.4.3	Vertex width	66
4.4.4	A method to estimate the uncertainty on the relative luminosity	67
4.4.5	Results of relative luminosity analysis	71
4.4.6	Event overlap	71
4.4.7	Single beam background	73
4.5	π^0 reconstruction	73
4.5.1	High- p_T photon trigger performance	74
4.5.2	Clustering algorithm	77
4.5.3	Quality assurance of the EMCal towers	78
4.5.4	Energy calibration of EMCal	78
4.5.5	Absolute energy scale	80
4.5.6	Reconstruction of π^0	83
4.5.7	EMCal stability	84
4.5.8	Discussion on the background peak	86
4.5.9	Cosmic ray event under π^0 signal window	87
4.5.10	Vertex cut difference in π^0 and BBC trigger	89
4.6	Spin asymmetries	93
4.6.1	Calculation of the asymmetries	93
4.6.2	Background ratio in signal window	95
4.6.3	Average p_T	96
4.6.4	Asymmetries	97
4.7	Systematic uncertainties	100
4.7.1	Beam polarizations	101
4.7.2	Beam polarization orientations	101
4.7.3	Relative luminosity	102
4.7.4	Bunch shuffling	102
4.7.5	Double collision effect	102
4.7.6	Summary of the systematic uncertainties	104
5	Results and discussions	105
5.1	The cross section results	105
5.2	Results of the double helicity asymmetries	107
5.3	Global analysis of polarized PDFs	108
5.3.1	AAC global analysis	108

5.3.2	DSSV global analysis	111
5.4	Further study on the spin structure of the proton	114
6	Conclusion	116
A	z-dependent BBC-efficiency	120
A.1	Overview	120
A.2	z -dependent BBC-efficiency at $\sqrt{s} = 62.4$ GeV	120
A.2.1	Procedure with WCM and vernier scan	120
A.2.2	Results at $\sqrt{s} = 62.4$ GeV	121
B	EMC clustering algorithm	124
B.1	PbSc	124
B.2	PbGl	126
C	Some information on pol-PDFs	127
C.1	Q^2 evolutions of parton contributions to the proton spin	127
C.2	DSSV polarized PDFs	128
C.3	GRSV	128
D	Subprocess cross sections for $gg \rightarrow q\bar{q}$ and $gg \rightarrow gg$	130

Chapter 1

Introduction

The proton is a very fundamental particle since all materials in the universe including ourselves are made of it. Thus it is natural desire as an intellectual being, to understand it. The proton turned out to be composed of quarks and gluons, which are the elementary particles to our best knowledge at present. Therefore, proton's fundamental properties (such as charge, spin, magnetic moment and mass) should be understood in terms of their components.

The proton has spin $1/2$. Polarized lepton-nucleon deep inelastic scattering (DIS) experiments have revealed that only $\sim 25\%$ of the proton spin is carried by quark and anti-quark spin [1, 2, 3, 4], which contradict our naive expectation that most of the proton spin is carried by quarks. It is called "spin crisis." One may complain it since the fact does not necessarily mean a breaking of a fundamental conservation law. Indeed, other components such as gluon spin and/or orbital angular momentum can carry the rest of the proton spin. It is sometimes called "spin puzzle" instead. Regardless of what we call it, it initiated various effort towards the understanding of the proton spin structure. Despite the wide efforts, the spin structure is still not well understood. There still remains large uncertainty, especially on gluon spin contribution to the proton, Δg . The main subject of this thesis is to put constraint on it.

The spin structure have been studied mainly with lepton-nucleon DIS, where the major contribution comes from the electromagnetic interaction. The gluons, however, are the mediator of strong interaction and do not react to electromagnetic interaction. Thus the gluons in the proton only participates at higher order processes in DIS, with the help of quarks which react to both strong and electromagnetic interactions. That is the reason why we don't have much information on the polarization of gluon. There are other efforts to explore gluon polarization in DIS by identifying final state hadrons and enhancing the gluon participating processes (Semi-inclusive DIS). The following experiments have measured helicity asymmetry of SDIS events with two high transverse momentum hadrons in the final state and extracted $\Delta g/g$. The HERMES experiment at HERA used 7.5 GeV polarized positron beam and a polarized hydrogen target [5, 6].

The Spin Muon Collaboration (SMC) at CERN used 190 GeV polarized muon beam scattered on polarized proton and deuteron targets [7]. The COMPASS experiment at CERN utilized 160 GeV polarized muon beam scattered on a polarized ${}^6\text{LiD}$ target [8]. The COMPASS experiment has also measured SDIS events with D^* mesons (open charm) tagged [9]. These measurements probe x region of $0.06 \sim 0.4$. However, the analyses are based on Monte Carlo simulations at leading order (LO). Next-to-leading order (NLO) calculations are not complete, and they suffer from large theoretical uncertainties.

Hard scatterings in polarized pp collisions are ideal tools to explore Δg since the gluons in the proton participate the interaction directly at the leading order. However, it is technically difficult to maintain the polarizations of proton beams through the acceleration. The difficulty was overcome by the invention of Siberian snakes [10, 11]. Relativistic Heavy Ion Collider (RHIC) was given the ability to accelerate and collide polarized protons by Siberian snakes and it has been providing us an unique opportunity to explore gluon spin in the proton directly through strong interactions [12]. Double helicity asymmetry (A_{LL}) of inclusive π^0 production in polarized pp collisions is sensitive to Δg since π^0 production is dominated by gluon-gluon (gg) and quark-gluon (qg) scattering for the currently accessible range of p_T . Since 2002, the PHENIX experiment at RHIC has been measuring A_{LL} of π^0 at $\sqrt{s} = 200$ GeV [13, 14, 15, 16] and has put constraint on Δg . However, there still remains large uncertainty on Δg at large Bjorken x .

In Run 2006, we performed polarized pp experiment not only at $\sqrt{s} = 200$ GeV, but also at $\sqrt{s} = 62.4$ GeV. Probed Bjorken x roughly scales with the scaling variable x_T , which is defined as $x_T = 2p_T/\sqrt{s}$. At fixed x_T , the cross section of π^0 is two orders of magnitude larger at $\sqrt{s} = 62.4$ GeV compared to that at $\sqrt{s} = 200$ GeV. Thus the lower center of mass energy have an advantage to probe large x gluons.

Originally low energy experiment at $\sqrt{s} = 62.4$ GeV was motivated by heavy ion experiment. A new state of dense matter is formed in Au-Au collisions at $\sqrt{s_{NN}} = 200$ GeV at RHIC. Parton energy loss in the produced dense medium results in high p_T leading hadron suppression. Measurements of high p_T data at lower energies are of great importance in identifying the energy range at which the suppression sets in. They require solid measurements of the cross section in pp collisions as a baseline for medium effects. PHENIX has measured particle production in Au+Au and Cu+Cu collisions at $\sqrt{s_{NN}} = 62.4$ GeV and discussed them with the results of pp collisions as a baseline which were obtained at Intersecting Storage Rings (ISR) at CERN. The energy $\sqrt{s} = 62$ GeV is the highest collision energy available at the ISR, the world's first (unpolarized) pp collider. At the ISR, inclusive neutral and charged pion cross sections were measured several times at $\sqrt{s} \sim 62$ GeV, but they have large uncertainties and have a large variation [17]. Having both heavy-ion and baseline pp measurements with the same experiment is advantageous as it leads to a reduction of the systematic uncertainties and, thus, to a more precise relative comparison of the data. The π^0 measurements at $\sqrt{s} = 62.4$ GeV is advantageous for both heavy-ion and spin physics.

Measurements of other final states in polarized pp collisions have also been performed.

PHENIX has obtained preliminary results for A_{LL} of charged pions (π^+ , π^-) [18], η [19], and direct photon [20, 21] at $\sqrt{s} = 200$ GeV. The STAR experiment at RHIC has published jet A_{LL} at $\sqrt{s} = 200$ GeV [22] and presented preliminary results for charged pions A_{LL} [23]. These measurements are complementary to the results of π^0 A_{LL} since they have different systematics. Measurements of π^0 A_{LL} have disadvantage in determining the sign of Δg since Δg contributes to A_{LL} as a quadratic function (since gg and gq are the dominant subprocesses). The $(\Delta g)^2$ contribution cancels in the difference of π^+ and π^- thus they are important complementary measurements. However, their drawback is the statistics due to the fact that an efficient trigger is not available. Direct photon production is dominated by $qg \rightarrow q\gamma$ and is also sensitive to the sign however, the drawback is the low statistics.

In Chap. 2, we introduce the theoretical framework. In the framework, the spin structure of the proton is described in terms of the polarized parton distribution functions (PDFs). The current experimental knowledge on the unpolarized and polarized PDFs is also described in the chapter. The double helicity asymmetry A_{LL} which is the measured quantity in this thesis, is defined. In Chap. 3, the experimental setup is explained. RHIC, which is the collider that provides polarized pp collisions, is introduced. and the PHENIX detector, which is used in this thesis to detect π^0 from pp collisions, is explained. The detailed analysis procedure is discussed in Chap. 4. In Chap. 5, the results of A_{LL} of π^0 production at $\sqrt{s} = 62.4$ GeV, together with the results of cross section, are shown and the impact of the results on the gluon polarization in the proton is discussed. We summarize our conclusion in Chap. 6.

The gluon spin contribution to the proton is written in either the upper or the lower cases, ΔG or Δg in the literature. There is a tendency to express integral of Δg as ΔG . Some experimentalists use ΔG instead of Δg to show that their data is not sensitive to the functional form of Δg . However, there is no strict rule about it. Mostly the lower case Δg is used and these are not strictly distinguished in this thesis. When x dependence is of interest, it is written as $\Delta g(x)$. The upper case is used for the labels of some PDF models (such as $\Delta G = 0$), and an integral of Δg .

Chapter 2

Physics - theoretical framework and present status of spin structure functions

The goal of the thesis is to obtain information on the spin structure of the proton through π^0 production in polarized pp collisions. The spin (and unpolarized) structure is expressed by the parton model, in terms of the parton distribution functions (PDFs).

The parton model interpretation of π^0 production in pp collision is explained in Sec. 2.1. Although this thesis is based on pp collisions, the structure of the proton has been studied with deep inelastic scatterings (DIS) before our experiment started. In Sec. 2.2, the formalism for DIS experiment for unpolarized and polarized targets are introduced. An improvement of the parton model given by DGLAP equations, and factorization is introduced in Sec. 2.3. The factorization theorem, which validates the framework is explained in Sec. 2.4. Some useful sum rules for the 1st moment of PDFs are known and are introduced in Sec. 2.5. Experimental knowledge (before our experiment started) on unpolarized and polarized PDFs are shown in Sec. 2.6 and Sec. 2.7. The double helicity asymmetry A_{LL} which is the measured quantity in this thesis, is discussed in Sec. 2.8. A scaling variable x_T is introduced and the probed kinematical range are explained in Sec. 2.9.

2.1 π^0 production in pp collisions

π^0 production in pp collisions is understood by the parton model [24]. The proton is considered to be a collection of point-like particles called “partons” and the interaction is understood as the incoherent sum of the partons’. This is so-called an impulse approximation. The partons in the proton are identified as quarks and gluons. Figure 2.1 illustrates π^0 production in pp collisions. A parton “a” from a proton and a parton “b”

from another proton interact and the final state parton “c” fragments into π^0 .

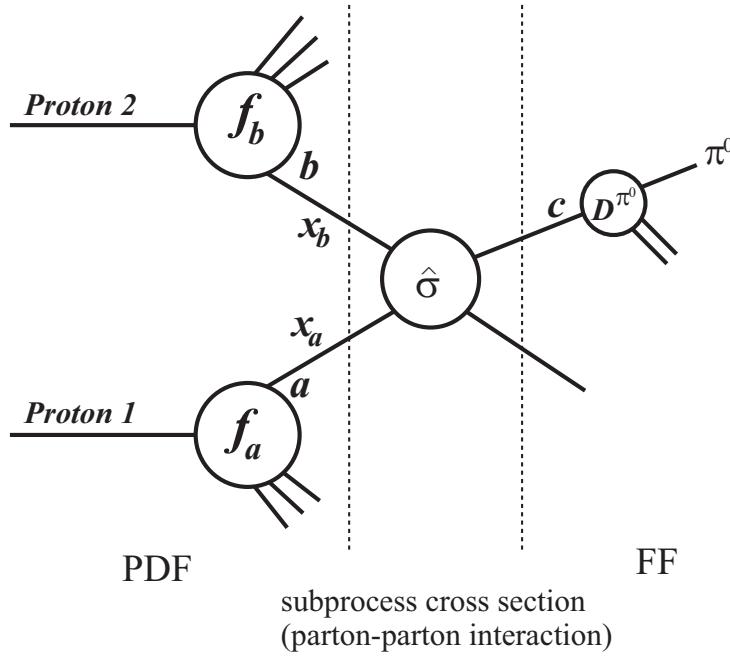


Figure 2.1: π^0 production in pp collisions. The process is divided into three parts: PDFs, subprocess cross sections, and FFs.

The unpolarized differential cross section is written as

$$d\sigma = \Sigma_{a,b,c} \int dx_a \int dx_b \int dz_c f_a(x_a, \mu^2) f_b(x_b, \mu^2) [d\hat{\sigma}_{ab}^c(x_a P, x_b P, \mu^2) D_c^\pi(z, \mu^2)] \quad (2.1)$$

$f_a(x_a, \mu^2)$ is the parton distribution function (PDF) of a parton species “a” to have a momentum fraction x_a of the parent proton with momentum P , and $f_b(x_b, \mu^2)$ is for a parton “b” with a momentum fraction x_b . $d\hat{\sigma}_{ab}^c(x_a P, x_b P, \mu^2)$ represents the cross section of parton-parton interaction (partonic cross section). $D(z, \mu^2)$ is the probability for a parton “c” to fragment into π^0 , with π^0 having a fraction z of the parton’s momentum. It is called the fragmentation function (FF). μ^2 represents equally chosen renormalization and factorization scale ($\mu^2 = \mu_R^2 = \mu_F^2$). In this framework, π^0 production is divided into three parts: PDFs, subprocess (or partonic) cross sections, and FFs. PDFs and FFs cannot be calculated with perturbative QCD (pQCD) and have to be determined by experiments. The subprocess cross sections can be calculated with pQCD. The factorization scale μ_F^2 was introduced to renormalize the unperturbative soft physics part into PDFs and FFs. The treatment is called the factorization and is discussed in Sec. 2.3 and 2.4.

The polarized differential cross-section is written in similar way,

$$d\Delta\sigma \equiv d\sigma_{++} - d\sigma_{+-}$$

$$= \Sigma_{a,b,c} \int dx_a \int dx_b \int dz_c \Delta f_a(x_a, \mu^2) \Delta f_b(x_b, \mu^2) [d\Delta \hat{\sigma}_{ab}^c(x_a P, x_b P, \mu^2) D_c^\pi(z, \mu^2)] \quad (2.2)$$

where σ_{++} (σ_{+-}) denote the cross section for same (opposite) helicity combination of the initial protons, and $\Delta f_a(x_a, \mu)$ is the spin-dependent PDF of the parton a which is defined as

$$\Delta f_a(x_a, \mu) = f_a^+(x_a, \mu) - f_a^-(x_a, \mu). \quad (2.3)$$

$f_a^+(x_a, \mu)$ ($f_a^-(x_a, \mu)$) is the PDF for parton a to have the same (opposite) helicity as the parent proton's. $\Delta f_b(x_b, \mu)$ is defined in the same way for parton b . $\Delta \hat{\sigma}_{ab}^c(x_a P, x_b P, \mu^2)$ represents the polarized cross section of parton-parton interaction. which is defined as

$$\Delta \hat{\sigma}_{ab}^c(x_a P, x_b P, \mu^2) = [\hat{\sigma}_{ab}^c(x_a P, x_b P, \mu^2)]_{++} - [\hat{\sigma}_{ab}^c(x_a P, x_b P, \mu^2)]_{+-}, \quad (2.4)$$

where the subscripts $++$ and $+-$ denote the spin states of the interacting partons.

2.2 Deep inelastic scattering formalism

The unpolarized and polarized structure of the proton has been studied with deep inelastic scattering (DIS). Thus we introduce its formalism in this section, and discuss higher order corrections in the next section. Its derivation and detailed discussion on the formalism can be found in [25, 26].

DIS is a high-energy inelastic scattering between leptons and nucleons. We take electron proton deep inelastic scattering as an example. Let $k^\mu = (E, \mathbf{k})$ be the four-vector of the incident electron, $k'^\mu = (E', \mathbf{k}')$ be that of the scattered electron. In a similar way, let $P^\mu = (M, 0)$ be the four-vector of the target proton, where M denotes the proton mass. The invariant mass of the final state hadron(s) is defined as W . The process can be described as:

$$e(E, \mathbf{k}) + P(M, 0) \rightarrow e(E', \mathbf{k}') + X(W, P_X), \quad (2.5)$$

and can be illustrated as Fig. 2.2a).

Bjorken scaling variable x is defined as

$$x \equiv \frac{-q^2}{2P \cdot q} = \frac{Q^2}{2P \cdot q}, \quad (2.6)$$

where Q^2 is defined as $Q^2 = -q^2$ so that $Q^2 > 0$. It can be interpreted as the fractional momentum of parton as described later. A Lorentz invariant variable ν is introduced as $\nu = \frac{P \cdot q}{M}$ which is equal to the energy loss of the lepton ($E - E'$) in the laboratory frame. Another Lorentz invariant variable y is defined as $y = \frac{P \cdot q}{p \cdot k}$ and is equal to the fractional

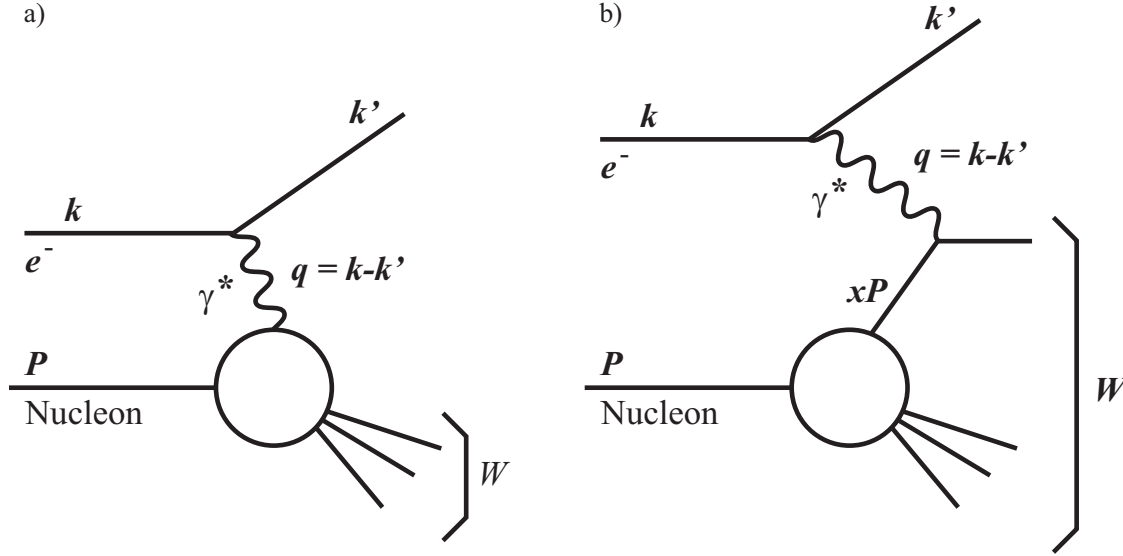


Figure 2.2: a) Deep inelastic scattering (DIS). b) DIS interpreted by the parton model.

energy loss of the lepton ν/E in the laboratory frame. The introduced variables are summarized in Table. 2.1

The exact calculation of cross section is not possible due to the lack of the knowledge on the structure of the proton, but the structure can be parametrized with structure functions since the form is restricted by the Quantum Chromodynamics (QCD).

With the help of the Lorentz invariance of the matrix element, parity conservation, and current conservation, the unpolarized cross section is written as

$$\frac{d^2\sigma}{dx dQ^2} = \frac{2\pi\alpha^2}{xQ^4} [Y_+ F_2(x, Q^2) - y^2 F_L(x, Q^2)], \quad (2.7)$$

where $Y_+ = 1 + (1 - y)^2$, F_2 and F_L are the structure functions. Some use another structure function F_1 ($F_L \equiv F_2 - 2xF_1$) to describe the cross section.

The formalism introduced so far does not depend on the parton model. Here we interpret the process in the parton model, as in the case of pp collisions. It can be shown that the Bjorken x (defined in Eq. 2.6) is interpreted as the fractional longitudinal momentum of the participating parton when the Q^2 is high enough to neglect the proton and the parton masses. (In the parton model, initial transverse momentum of the parton, which is called the intrinsic k_T , is also neglected in the PDF parametrization.) Let ξP be the momentum of the parton, so that ξ is the fractional momentum of the parton. Since the parton and the proton masses are neglected,

$$(\xi P + q)^2 = 0$$

$$\begin{aligned}
2\xi P \cdot q + q^2 &= 0 \\
\xi &= \frac{-q^2}{2P \cdot q}.
\end{aligned} \tag{2.8}$$

Therefore, $\xi = x$ and the Bjorken x can be interpreted as the fractional momentum of parton. Figure 2.2b) illustrates the parton model interpretation of DIS, where a parton with momentum fraction of x interact with the virtual photon. Let $q_i(x)$ be the parton distribution function for a parton i . Here $q_i(x)$ is used instead of $f_i(x)$ to indicate that the participating partons are quarks. The polarized quark distribution $\Delta q_i(x)$ is defined in a similar way as Eq. 2.3. The cross section can be calculated as an incoherent sum of parton-photon scatterings. Then the structure functions F_2 and F_L are identified as

$$F_2(x, Q^2) = \sum_i e_i^2 x q_i(x) \tag{2.9}$$

$$F_L(x, Q^2) = 0. \tag{2.10}$$

The first equation indicates that $F_2(x, Q^2)$ is independent of Q^2 . The scaling behavior was derived for $Q^2 \rightarrow \infty$ at fixed x (DIS limit) by Bjorken [27] and is called the Bjorken scaling. The 2nd equation is the Callan-Gross relationship, $F_2 = 2xF_1$, as a consequence of scattering from spin 1/2 partons [28]. Early SLAC data showed that the relation holds. [29]

The cross sections for polarized DIS are parametrized as

$$\frac{d^2 \Delta \sigma_{\parallel}}{dx dQ^2} \equiv \frac{d^2 \sigma_{\leftarrow}^{\rightarrow}}{dx dQ^2} - \frac{d^2 \sigma_{\rightarrow}^{\rightarrow}}{dx dQ^2} \tag{2.11}$$

$$= \frac{16\pi\alpha^2 y}{Q^4} \left[\left(1 + \frac{y}{2} - \gamma^2 \frac{y^2}{4}\right) g_1(x, Q^2) - \gamma^2 \frac{y}{2} g_2(x, Q^2) \right], \tag{2.12}$$

$$\frac{d^2 \Delta \sigma_{\perp}}{dx dQ^2} \equiv \frac{d^2 \sigma_{\uparrow}^{\rightarrow}}{dx dQ^2} - \frac{d^2 \sigma_{\downarrow}^{\rightarrow}}{dx dQ^2} \tag{2.13}$$

$$= -\cos\phi \frac{8\alpha^2 y}{Q^4} \gamma \sqrt{1 - y - \gamma^2 \frac{y^2}{4}} \left[\frac{y}{2} g_1(x, Q^2) + g_2(x, Q^2) \right], \tag{2.14}$$

where \Rightarrow and \Leftarrow (\Uparrow and \Downarrow) denote the nucleon helicity (transverse spin) state, \rightarrow and \leftarrow denote the incident lepton's helicity state, $\gamma = 4m^2 x^2 / Q^2$, and g_1 and g_2 are the polarized structure functions.

The polarized structure functions are found to be

$$g_1(x, Q^2) = \frac{1}{2} \sum_i e_i^2 \Delta q_i(x) \tag{2.15}$$

$$g_2(x, Q^2) = 0, \tag{2.16}$$

in the zeroth order parton model. $g_2(x)$ was measured by several groups [30, 31] and $g_2 = 0$ holds approximately.

variable	description
x	$= \frac{Q^2}{2P \cdot q} = \frac{Q^2}{2M\nu}$. Bjorken scaling variable.
ν	$= \frac{p \cdot q}{M} (= E - E')$. The energy loss of the lepton in the laboratory frame.
y	$= \nu/E = p \cdot q/p \cdot k$. The fractional energy loss of the lepton.
q	$= k - k'$. The four-momentum transfer.
Q^2	$= -q^2 > 0$. The four-momentum transfer squared.
Y_+	$= 1 + (1 - y)^2$

Table 2.1: Variables commonly used in DIS description. Please note that x, ν, y , and Q^2 are written in terms of Lorentz invariant variables, but some of them are interpreted in the laboratory frame.

The introduced structure functions and their interpretation in the parton model are summarized in Table. 2.2.

structure func.	interpretation in the parton model.
$F_1(x, Q^2)$	$= \sum_i e_i^2 x q_i(x)$ $= \frac{4}{9}\{xu(x) + x\bar{u}(x)\} + \frac{1}{9}\{xd(x) + x\bar{d}(x)\} + \frac{1}{9}\{xs(x) + x\bar{s}(x)\}$
$F_L(x, Q^2)$	$= 0$
$g_1(x, Q^2)$	$= \frac{1}{2} \sum_i e_i^2 \Delta q_i(x)$ $= \frac{1}{2} \left[\frac{4}{9}\{\Delta u(x) + \Delta\bar{u}(x)\} + \frac{1}{9}\{\Delta d(x) + \Delta\bar{d}(x)\} + \frac{1}{9}\{\Delta s(x) + \Delta\bar{s}(x)\} \right]$
$g_2(x, Q^2)$	$= 0$

Table 2.2: The structure functions in DIS and their interpretation in the parton model. The quarks heavier than s are neglected.

2.3 DGLAP equations and factorization

An improvement of parton model beyond the zeroth order was developed by Dokshitzer, Gribov, Lipatov, Altarelli and Parisi, collectively known as DGLAP. The improvement is referred to as the DGLAP evolutions or Q^2 evolutions.

Figure 2.3a) shows a zeroth order process where a parton (quark) in the proton with momentum xP directly absorb virtual photon. However, the parton may emit gluon before

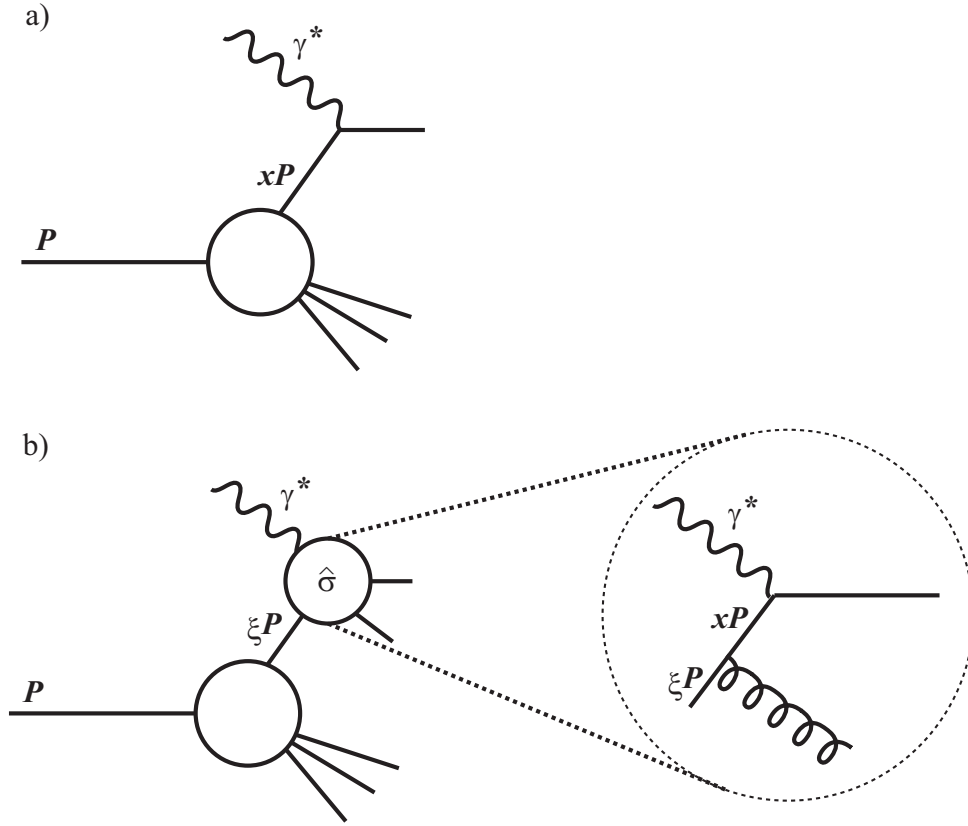


Figure 2.3: a) Zeroth order parton model. b) Improved parton model.

(or after) absorbing the virtual photon, as in Fig. 2.3b). In Fig. 2.3b), ξP describes the initial quark momentum, and it evolves to the quark with momentum xP . A variable z is defined as $z = Q^2/(2\xi P \cdot q)$, in the analog of Bjorken x . z is the fractional momentum of the evolved parton compared to the initial parton, $xP = z \cdot \xi P$.

The cross section is obtained by integrating over all possible gluon emissions. However, the cross section of such process is divergent in the limit of collinear gluon emission, where the angle between the quark and the emitted gluon reaches zero. The divergence is regulated by introducing an arbitrary cut-off κ^2 . The cross section becomes to have a large log term $\ln(Q^2/\kappa^2)$. It is divided into two parts, by introducing a factorization scale μ_F , as $\ln(Q^2/\kappa^2) \rightarrow \ln(Q^2/\mu_F^2) + \ln(\mu_F^2/\kappa^2)$. The term $\ln(\mu_F^2/\kappa^2)$ are put into PDFs and the arbitrary cut-off κ^2 is hidden under PDFs. The other term which is free from the arbitrary cut-off, is put into the subprocess cross sections. The treatment is called the factorization.

After the factorization, PDF (and partonic cross sections) becomes dependent on a factorization scale μ_F^2 . The final cross section should not depend on μ_F^2 , but the scale

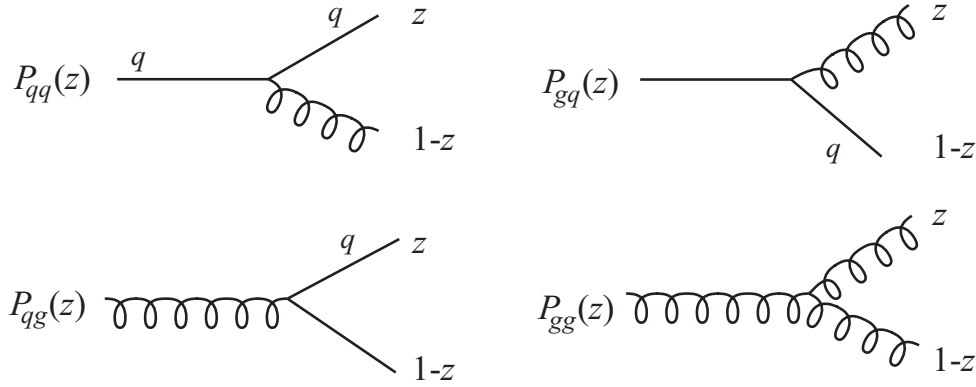


Figure 2.4: The splitting functions.

should be larger than the arbitrary cut-off and should not be too large to make a term $\ln(Q^2/\mu_F^2)$ moderate size which appear in partonic cross section. The factorization scale is usually chosen as $\mu_F^2 = Q^2$ for deep inelastic scatterings, and $\mu_F^2 = p_T^2$ for π^0 production in pp collisions. Although the factorization scale μ_F^2 and the renormalization scale μ_R^2 don't have to be equal, both are often chosen as $\mu_F^2 = \mu_R^2$. The obtained cross-section should not depend on the choice of the scale, but it does due to the truncation in perturbative expansion. The dependence on the scale is often used as a guide for the theoretical uncertainty.

The renormalized PDF cannot be calculated perturbatively as it includes the non-perturbative part. However, once PDFs are known for a certain scale, their evolutions with $\ln \mu^2$ can be calculated as

$$\frac{\partial}{\partial \ln \mu^2} \begin{pmatrix} q_i(x, \mu^2) \\ g(x, \mu^2) \end{pmatrix} = \frac{\alpha_s(\mu^2)}{2\pi} \sum_j \int_x^1 \frac{d\xi}{\xi} \begin{pmatrix} P_{q_i q_j}(\frac{x}{\xi}, \alpha_s(\mu^2)) & P_{q_i g}(\frac{x}{\xi}, \alpha_s(\mu^2)) \\ P_{g q_j}(\frac{x}{\xi}, \alpha_s(\mu^2)) & P_{g g}(\frac{x}{\xi}, \alpha_s(\mu^2)) \end{pmatrix} \begin{pmatrix} q_j(\xi, \mu^2) \\ g(\xi, \mu^2) \end{pmatrix}, \quad (2.17)$$

where $P_{qq}(z)$ is the probability distribution for $q(\xi) \rightarrow q(z\xi)g((1-z)\xi)$ splitting, $P_{qg}(z)$ for $g(\xi) \rightarrow q(z\xi)g((1-z)\xi)$ splitting, which are called splitting functions. Other two splitting functions are defined in similar way. The four types of the splitting functions in Eq. 2.17 are summarized graphically in Fig. 2.4.

The splitting functions are expanded as power series in $\alpha_s(\mu^2)$,

$$P_{q_i q_j}(z, \mu^2) = \delta_{ij} P_{qq}^{(0)}(z) + \frac{\alpha_s}{2\pi} P_{q_i q_j}^{(1)}(z) + \dots \quad (2.18)$$

$$P_{qg}(z, \mu^2) = P_{qg}^{(0)}(z) + \frac{\alpha_s}{2\pi} P_{qg}^{(1)}(z) + \dots \quad (2.19)$$

P_{gq} and P_{gg} are expanded in similar way as Eq. 2.19. The δ_{ij} in the leading term of Eq. 2.18 indicates that one needs higher order term beyond LO to change the quark flavor. Because of charge conjugation and the flavor independence of the QCD Lagrangian, P_{qg} and P_{gq} are independent of quark flavor and the same for q and \bar{q} . The $P_{q_i q_j}$ satisfy $P_{q_i q_j} = P_{\bar{q}_i \bar{q}_j}$ and $P_{q_i \bar{q}_j} = P_{\bar{q}_i q_j}$ and the leading order term vanishes unless $q_i = q_j$.

A non-singlet combination is the difference of q_i and q_j . Among the non-singlets, an useful combination is

$$q_i^-(x, \mu^2) = q_i(x, \mu^2) - \bar{q}_i(x, \mu^2), \quad (2.20)$$

which is the valence quark distribution for flavor i . The evolution of non-singlet distribution does not involve the gluon density since it cancels. The splitting functions are known to NNLO accuracies.

Similar equations are obtained for polarized case and can be written as:

$$\frac{\partial}{\partial \ln \mu^2} \begin{pmatrix} \Delta q(x, \mu^2) \\ \Delta g(x, \mu^2) \end{pmatrix} = \frac{\alpha_s(\mu^2)}{2\pi} \int_x^1 \frac{d\xi}{\xi} \begin{pmatrix} \Delta P_{qq}(\frac{x}{\xi}, \alpha_s(\mu^2)) & \Delta P_{qg}(\frac{x}{\xi}, \alpha_s(\mu^2)) \\ \Delta P_{gq}(\frac{x}{\xi}, \alpha_s(\mu^2)) & \Delta P_{gg}(\frac{x}{\xi}, \alpha_s(\mu^2)) \end{pmatrix} \begin{pmatrix} \Delta q(\xi, \mu^2) \\ \Delta g(\xi, \mu^2) \end{pmatrix} \quad (2.21)$$

The splitting functions have been calculated at NLO accuracy [32, 33]. Non singlet combinations $\Delta q - \Delta \bar{q}$, and $\Delta q_i + \Delta \bar{q}_i - \Delta q_j - \Delta \bar{q}_j$ does not couple to gluon in evolution. In LO, quark helicity is conserved before and after the splitting thus $\Delta P_{qq} = P_{qq}$, $\Delta P_{qg} = P_{qg}$, $\Delta P_{gq} = P_{gq}$. The 1st moment $\Delta \Sigma$ does not depend on μ^2 at all at LO.

Beyond the leading order

The subprocess cross sections and DGLAP evolutions are expanded in power series of the strong coupling constant α_s . The leading order partonic processes are $2 \rightarrow 2$ reactions thus the perturbative expansion starts at $\mathcal{O}(\alpha_s^2)$. Next to leading order (NLO) calculations include terms at $\mathcal{O}(\alpha_s^3)$. In this section, α_s^2 is factored out and omitted as in the literature, since the factor α_s^2 is common for the process of strong interactions.

When the initial partons have just enough energy to produce a high-transverse momentum parton (which subsequently fragments into the observed hadron), the phase space available for gluon bremsstrahlung vanishes, resulting in large logarithmic corrections to the partonic cross section. We define

$$\hat{x}_T = 2\hat{p}_T/\sqrt{\hat{s}}, \quad (2.22)$$

where \hat{p}_T is the transverse momentum of scattered parton which fragments into observed hadron, \hat{s} is the center of mass energy of the partonic processes. If \hat{x}_T reaches unity, leading large contributions arise as $\alpha_s^k \ln^{2k}(1 - \hat{x}_T^2)$ at the k th order in perturbative expansion.

Such terms can be taken into account to all orders in α_s by threshold resummation [34]. It is called leading log (LL) calculations. One step higher order correction is called the next to leading log (NLL) calculations which includes terms appear in the form $\alpha_s^k \ln^{2k-1}(1-\hat{x}_T^2)$ at k th order perturbative expansion, to all orders. The relation between the fixed order perturbative expansions (LO, NLO, NNLO, ...) and the resummations (LL, NLL, NNLL, ...) is illustrated in Fig. 2.5.

The log terms become significant when $\hat{x}_T \rightarrow 1$. Therefore, they are significant in fixed target experiments, while they are small at collider energies. In fact, calculations show that the NLL corrections are necessary for fixed target experiment at $\sqrt{s} \sim 20$ GeV to describe the measured cross section [35], while NLL corrections are smaller at $\sqrt{s} = 200$ GeV [36].

The unpolarized and polarized cross sections for inclusive hadron production in pp collisions at $\sqrt{s} = 62.4$ GeV, which is this thesis is based on, are also calculated at both NLO and NLL accuracies [36]. They are compared with the results obtained at PHENIX experiment and discussed in Sec. 5.1.

LO	1				
NLO	$\alpha_s L^2$	$\alpha_s L$	α_s	+...	
NNLO	$\alpha_s^2 L^4$	$\alpha_s^2 L^3$	$\alpha_s^2 L^2$	$\alpha_s^2 L$	+...
	$\alpha_s^3 L^6$	$\alpha_s^3 L^5$	$\alpha_s^3 L^4$	$\alpha_s^3 L^3$	+...
	$\alpha_s^4 L^8$	$\alpha_s^4 L^7$	$\alpha_s^4 L^6$	$\alpha_s^4 L^5$	+...
	\vdots	\vdots	\vdots	\vdots	
N ^k LO	$\alpha_s^k L^{2k}$	$\alpha_s^k L^{2k-1}$	$\alpha_s^k L^{2k-2}$	$\alpha_s^k L^{2k-3}$	+...

LL
NLL
NNLL

Figure 2.5: Fixed order perturbative expansion (LO, NLO, NNLO, ...) and resummation (LL, NLL, NNLL, ...). L represents the large log term.

2.4 Factorization theorem

We introduced the framework to deal with particle production in pp collisions, and ep deep inelastic scatterings. π^0 production in pp collisions is written as a convolution of PDFs, cross section of parton parton interactions, and FFs (Eq. 2.1). Factorization

theorem [37] plays an important role in this framework as it ensures that the cross section of parton-parton interaction, $d\hat{\sigma}_{ab}^c(x_a P, x_b P, \mu^2)$, only depend on the parton species a , b and c , and not depend on the choice of the initial state hadron (proton in this case), nor the choice of the final state hadron (π^0 in this case). All the non perturbative phenomena are carried by PDFs and FFs and the theorem ensures that PDFs and FFs are universal. The same PDFs can be used for both pp collisions and ep deep inelastic scatterings. The FFs are the same for pp collisions and other processes such as ee collisions. In fact, most of the information on FFs are derived from hadron production in ee collisions.

The proofs of the factorizations are very technical and difficult tasks and rigorous proofs are only given for a few processes such as DIS and Drell-Yan. However, we assume that it holds for inclusive hadron production in pp collisions, which is the process that this thesis is based on. And the cross sections calculated in the formalism agree with experimental data as will be seen later.

2.5 Sum rules for PDFs

There are useful sum rules for the 1st moment of unpolarized and polarized PDFs. They are summarized in this section.

2.5.1 Sum rules for unpolarized PDFs

Since QCD Lagrangian conserves fermion number and flavor, the following sum rules must be obeyed by the parton densities for valence quarks in the proton:

$$\int_0^1 dx [u(x, \mu^2) - \bar{u}(x, \mu^2)] \equiv \int_0^1 dx u_v(x, \mu^2) = 2 \quad (2.23)$$

$$\int_0^1 dx [d(x, \mu^2) - \bar{d}(x, \mu^2)] \equiv \int_0^1 dx d_v(x, \mu^2) = 1 \quad (2.24)$$

$$\int_0^1 dx [s(x, \mu^2) - \bar{s}(x, \mu^2)] \equiv \int_0^1 dx s_v(x, \mu^2) = 0 \quad (2.25)$$

$$\int_0^1 dx [c(x, \mu^2) - \bar{c}(x, \mu^2)] \equiv \int_0^1 dx c_v(x, \mu^2) = 0, \quad (2.26)$$

and overall momentum conservation gives

$$\int_0^1 dx x \left[\sum_i (q_i(x, \mu^2) + \bar{q}_i(x, \mu^2) + g(x, \mu^2)) \right] = 1, \quad (2.27)$$

2.5.2 Sum rule for polarized PDFs

Total angular momentum conservation gives the important spin sum rule for the proton:

$$\frac{1}{2} = \frac{1}{2} \Delta\Sigma(\mu^2) + \Delta G(\mu^2) + L_z(\mu^2), \quad (2.28)$$

where

$$\Delta\Sigma(\mu^2) = \int_0^1 dx \sum_i \left(\Delta q_i(x, \mu^2) + \Delta \bar{q}_i(x, \mu^2) \right), \quad (2.29)$$

$$\Delta G(\mu^2) = \int_0^1 dx \Delta g(x, \mu^2), \quad (2.30)$$

and $L_z(\mu^2)$ is the orbital angular momentum of quarks and gluons. $\Delta\Sigma(\mu^2)$ does not evolve with μ^2 at LO while $\Delta G(\mu^2)$ depends logarithmically on μ^2 and the evolution of $\Delta G(\mu^2)$ is compensated by that of $L_z(\mu^2)$. A toy model calculation of the evolutions of the first moments is presented in Appendix C.1.

2.6 Unpolarized PDFs

Unpolarized PDFs are extensively studied by deep inelastic scattering (DIS). The strategy for the determination of PDFs is the following. Assume a reasonable functional forms for PDFs at a certain input scale μ^2 , then calculate structure functions and search for best parameters to describe the data.

There are many groups such as CTEQ [38], MRST [39], and GRV [40] working on PDFs with slightly different assumptions and functional forms. Parametrization is often done for valence and anti-quarks, rather than quarks and anti-quarks since valence distributions are non-singlets and are independent of gluon distribution.

We introduce the MRST2002 PDF set since the polarized and unpolarized cross section of π^0 production which this thesis is based on, are calculated with it [36]. PDFs are parametrized at input scale of $\mu^2 = 1$ (GeV/c)². Each of the valence quarks and the total sea quark contribution are parametrized in the form

$$xq(x) = A(1-x)^\eta(1 + \varepsilon x^{0.5} + \gamma x)x^\delta \quad (2.31)$$

where A is determined by the sum rule for the number of valence quarks of each type (Eq. 2.24-2.26). The gluon distribution is parametrized as

$$xg(x) = A_g(1-x)^{\eta_g}(1 + \varepsilon_g x^{0.5} + \gamma_g x)x^\delta - A_-(1-x)^{\eta_-}x^{-\delta_-} \quad (2.32)$$

where A_g is determined by the momentum sum rule (Eq. 2.27). The combination $\bar{u}(x) - \bar{d}(x)$ is parametrized as

$$x(\bar{u}(x) - \bar{d}(x)) = A(1-x)^\eta(1 + \gamma x + \delta x^2)x^\delta \quad (2.33)$$

The functional form $x^\delta(1-x)^\eta$ is assumed according the behavior in the limits at $x \rightarrow 0, 1$, suggested by Regge theory and the constituent counting rules[41], respectively. The major ingredients for the determination of unpolarized PDFs are the structure functions

$F_2(x, Q^2)$ for the proton and the neutron (deuteron) targets with wide range of x and Q^2 . The structure function $F_2(x, Q^2)$ for proton targets is shown in Fig. 2.6. Although Bjorken scaling predicts that the structure function is independent of Q^2 , the scaling violation is visible. The scaling violation comes from the running coupling constant and Q^2 evolutions. F_2 for the proton and the neutron can be used for flavor separation, and its Q^2 dependence for gluons. Neutrino induced DIS and W boson charge asymmetry at Tevatron help flavor separations.

Figure 2.7 shows the MRST2002 results of the PDF at NLO at $Q^2 = 4$ (GeV/c)². u and d distributions have a peak around $x \sim 0.1 - 0.2$, since they are the valence quark flavors. (The valence quarks are $u - \bar{u}$ and $d - \bar{d}$ to be exact.) The rise in low x cancels for valence distribution, which come from the coupling to gluon evolution. $s(= \bar{s})$ and $c(= \bar{c})$ quark distributions are suppressed compared to other flavors because of their large mass.

2.7 Polarized PDFs

Polarized PDFs are also investigated by many groups such as AAC [43, 44], GRSV [45], LSS [46], and so forth. Here we show AAC03 results of polarized PDFs which is the results obtained before our experiment started. AAC PDFs are obtained separately for the valence u -quarks $\Delta u_v(x)$, the valence d -quarks $\Delta d_v(x)$, the sea quarks $\Delta \bar{q}(x)$ (with the assumption of flavor symmetric sea), and the gluons $\Delta g(x)$. The functional form for PDFs in the analysis is:

$$\Delta f(x) = [\delta x^\nu - \kappa(x^\nu - x^\mu)]f(x), \quad (2.34)$$

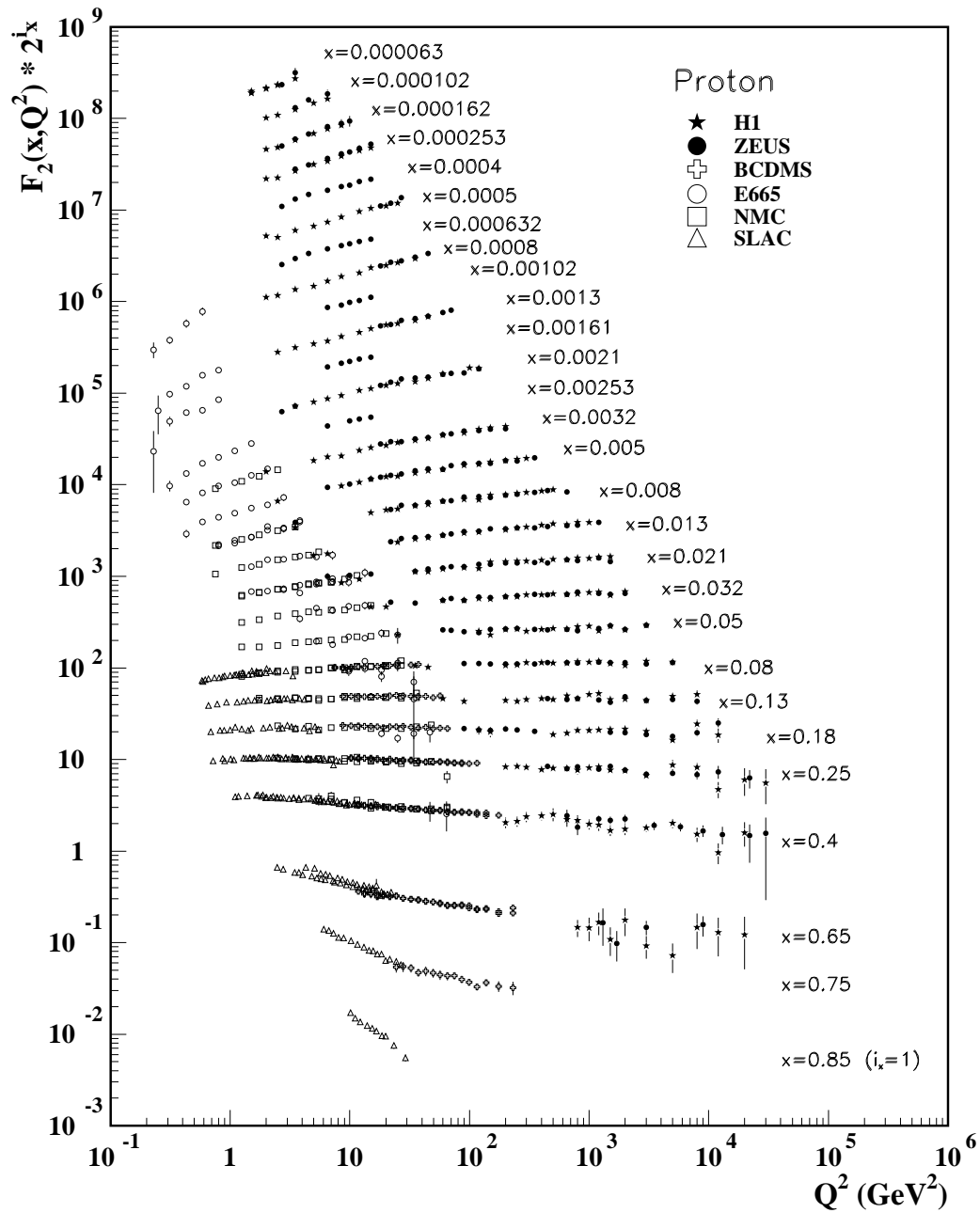
where δ , ν , κ , and μ are free parameters, and $f(x)$ is the corresponding unpolarized PDF. The input scale is $Q_0 = 1$ GeV/c. Although it is known that the unpolarized sea quark distributions are different for different flavor, there are not enough information for flavor separation in polarized PDFs. Thus flavor symmetric sea polarization is assumed. The positivity condition $|\Delta\sigma| \leq \sigma$ does not necessarily mean $|\Delta f(x)| \leq f(x)$ at NLO and higher. However, this condition is assumed since it avoids unphysical cross section $|\Delta\sigma| > \sigma$ due to the lack of experimental data.

Under the assumption of flavor SU(3) symmetry, the β decays of spin 1/2 octet baryons can be described by two parameters F , and D [47]. And certain combinations of polarized PDFs are related to these parameters as [48, 49, 3],

$$\begin{aligned} a_3 &\equiv \Delta U - \Delta D \\ &= F + D = 1.269 \pm 0.003 \end{aligned} \quad (2.35)$$

$$\begin{aligned} a_8 &\equiv \Delta U + \Delta D - 2\Delta S \\ &= 3F - D = 0.586 \pm 0.031, \end{aligned} \quad (2.36)$$

where ΔU , ΔD , and ΔS are $\Delta U \equiv \int_0^1 dx(\Delta u + \Delta \bar{u})$, $\Delta D \equiv \int_0^1 dx(\Delta d + \Delta \bar{d})$, and $\Delta S \equiv \int_0^1 dx(\Delta s + \Delta \bar{s})$. These relations are utilized to constraint the parameters of PDFs.

Figure 2.6: The structure function F_2 from DIS experiments.[42]

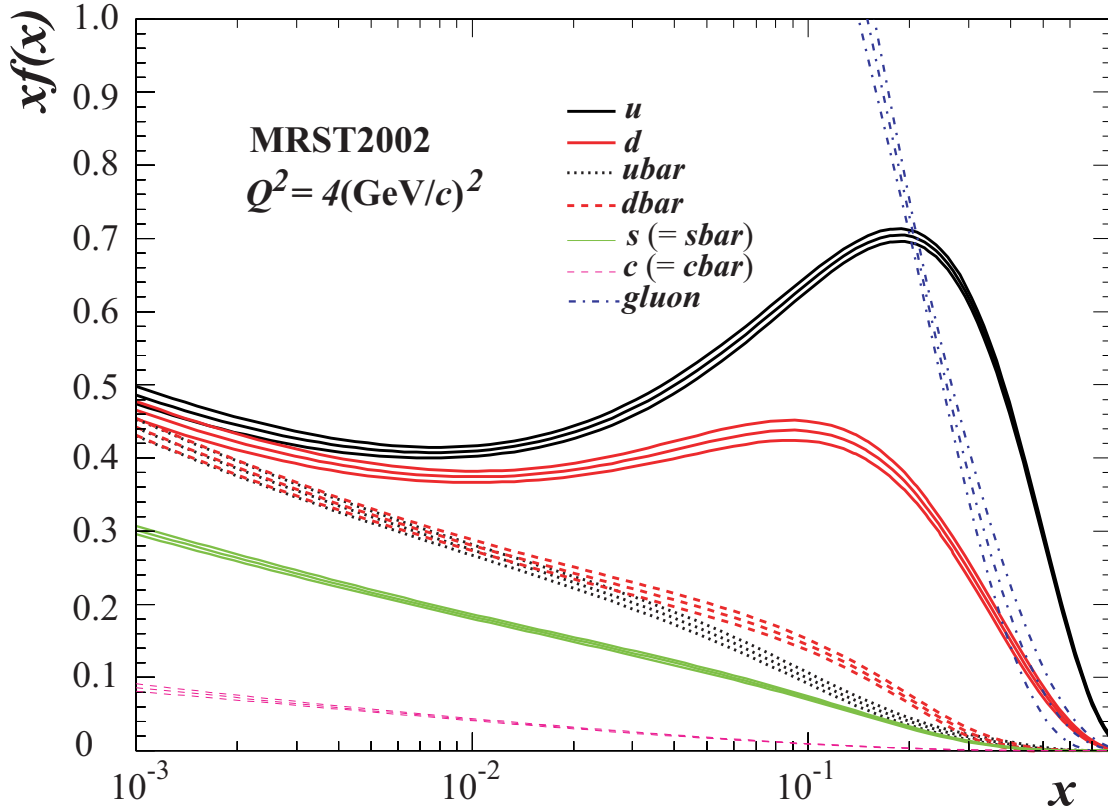


Figure 2.7: The MRST2002 PDF sets at $Q^2 = 4 \text{ (GeV/c)}^2$ [39]. The combinations of a color (blue, black, red, or green) and a line type (solid, dashed-dotted, dotted, or dashed) represent parton species. The three lines of each parton type shows the central value of the parton density and its uncertainties.

Eq. 2.35 is equivalent to the famous Bjorken sum rule [50]

$$\int_0^1 g_1^p(x) - g_1^n(x) dx = \frac{1}{6} \left| \frac{g_A}{g_V} \right| \left[1 - \frac{\alpha_s(Q^2)}{\pi} \right], \quad (2.37)$$

where $g_1^p(x)$ and $g_1^n(x)$ are the polarized structure functions for the proton and the neutron respectively. g_V and g_A are the vector and axial-vector coupling constant respectively, and they are related to F and D as $F + D = |g_A/g_V|$.

Major ingredients for polarized PDFs are the polarized structure functions $g_1(x, Q^2)$ for proton and deuteron targets. Fig. 2.8 shows the measured structure functions.

Figure 2.9 displays the AAC03 polarized PDF set. PDFs from other groups are also overlaid. Δu_v and Δd_v have relatively small uncertainty and fair agreement was reached among the PDF sets. But the gluon polarized PDF have large uncertainties, and needs

further experimental information. The 1st moment of AAC03 results are summarized in Table 2.3. The large uncertainty is also seen in the 1st moment of the gluon polarization. The quark spin contribution is $\frac{1}{2}\Delta\Sigma \sim 0.1$ and the rest of the proton spin might be carried by the gluon spin ΔG , but the uncertainty is too large to conclude it. The aim of the thesis is to provide new data towards the determination of the polarized PDF of the gluons.

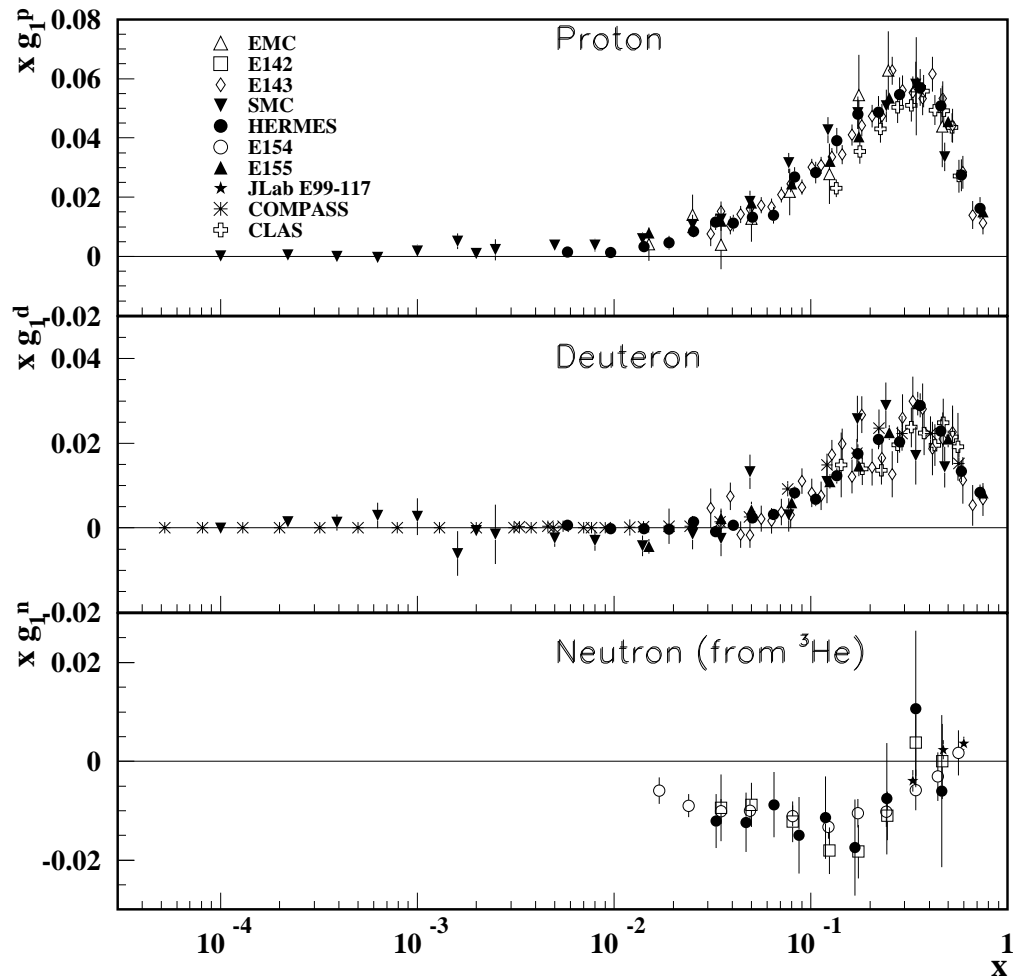


Figure 2.8: The structure function g_1 from DIS experiments.[51]

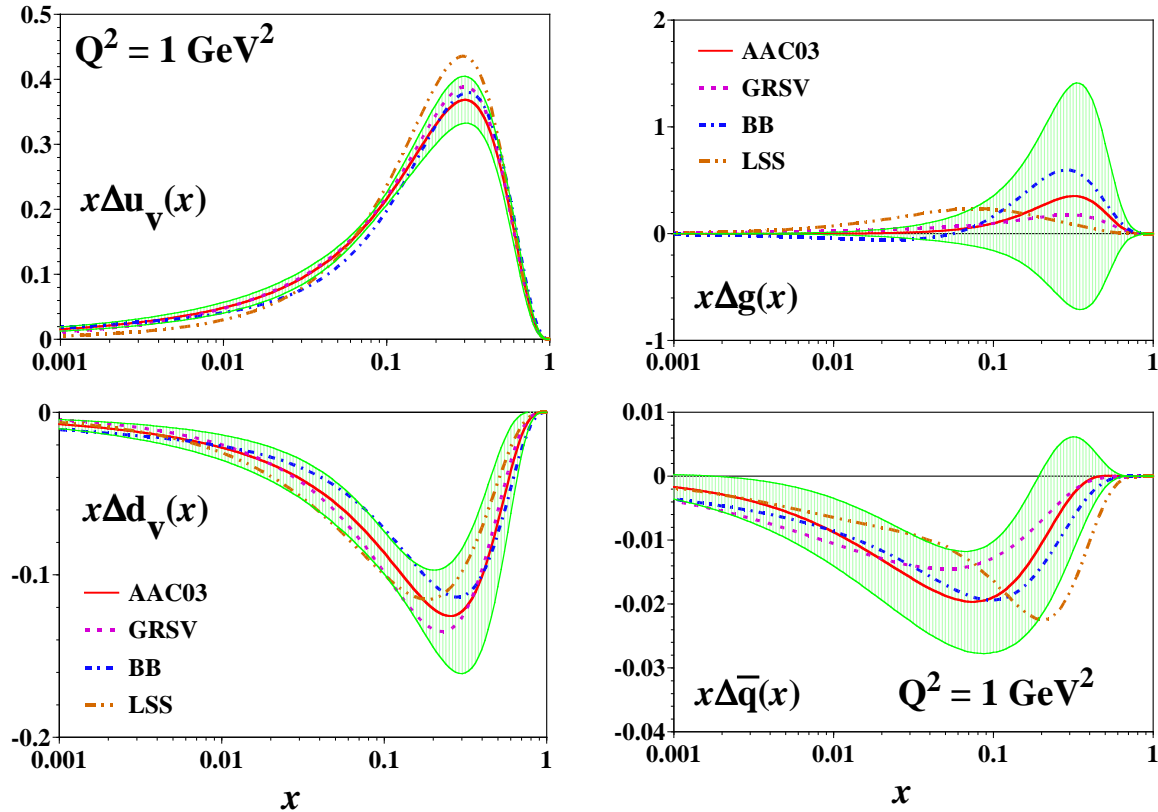


Figure 2.9: The AAC03 polarized PDF sets at $Q^2 = 1 \text{ (GeV}/c)^2$ [44]. The AAC03 results are compared with the results of other groups: GRSV [45], BB [52], LSS [46, 53, 54]. The green bands are the uncertainties for the polarized PDFs obtained by AAC03. The statistical and systematic uncertainties in the experimental results are added in quadrature and the theoretical uncertainties are not included.

2.8 Probing Δg in polarized pp collisions

Figure 2.10 displays the relative contribution of gg , qg , and qq scatterings to π^0 production at $\sqrt{s} = 62.4 \text{ GeV}$. As in the figure, the dominant subprocesses are qg and gg scatterings for the measured p_T range (1–4 GeV/c). Thus the π^0 production in pp collision is sensitive to the gluon distribution.

The polarized cross section $\Delta\sigma$ is directly connected to the polarized PDFs as defined in Eq. 2.2. Experimentally, instead of directly measured $\Delta\sigma$, the double helicity asymmetry A_{LL} is obtained which is defined as

$$A_{LL} = \frac{\Delta\sigma}{\sigma}, \quad (2.38)$$

since experimental efficiency and normalization of cross section cancels.

$\Delta\Sigma$	ΔG	$\Delta\bar{Q}$
0.213 ± 0.138	0.499 ± 1.266	-0.062 ± 0.023

Table 2.3: 1st moment of the polarized PDFs in AAC03.

The double helicity asymmetry for subprocess is defined in similar way as

$$\hat{a}_{LL} = \frac{\Delta\hat{\sigma}}{\hat{\sigma}}. \quad (2.39)$$

The \hat{a}_{LL} for various subprocesses are displayed in Fig. 2.11. Since the π^0 is detected in midrapidity in PHENIX, the measured range roughly corresponds to $\cos\theta \sim 0$. \hat{a}_{LL} for qg and gg is positive except for $gg \rightarrow q\bar{q}$. However, the contribution of $gg \rightarrow q\bar{q}$ is smaller than $gg \rightarrow gg$ by about three orders of magnitude as explained in Appendix D and overall subprocess asymmetry is positive.

2.9 x_T and probed x range

x_T is defined as $x_T = 2p_T/\sqrt{s}$, where \sqrt{s} is the center of mass energy of pp collisions, and p_T is the transverse momentum of π^0 . x_T is interpreted as the fractional momentum (x) of initial parton in the proton when the two partons with the same x collide, the scattering angle is 90 degrees, and the fragmentation is neglected. Figure 2.12 illustrates a scattering under the conditions mentioned above. The fragmentation process and precise consideration of kinematics “smear” the rough argument above. x and x_T are no longer equal, and rather broad range of x contributes for a certain p_T (or x_T) of π^0 as in Fig. 2.13 for example. However, the average x roughly scales with x_T and $x \sim 1.7x_T$.

Figure 2.14 displays the cross section for three different center of mass energy \sqrt{s} versus x_T calculated at NLO accuracy. The cross section is two orders of magnitude larger at fixed x_T at $\sqrt{s} = 62.4$ GeV compared to that at $\sqrt{s} = 200$ GeV. Thus lower center of mass energy can reach higher x_T with the same integrated luminosity. We have measured and presented the results of π^0 A_{LL} at $\sqrt{s} = 200$ GeV based on the data taken in Run 2005 [15]. The measurements at $\sqrt{s} = 62.4$ GeV, which this thesis is based on, are able to improve the accuracy at high x_T with smaller integrated luminosity compared to the measurements at $\sqrt{s} = 200$ GeV.

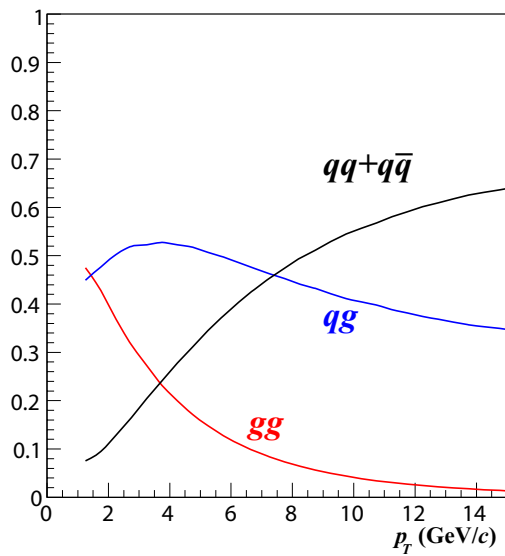


Figure 2.10: Relative contribution of processes to the production of π^0 at $\sqrt{s} = 62.4$ GeV.

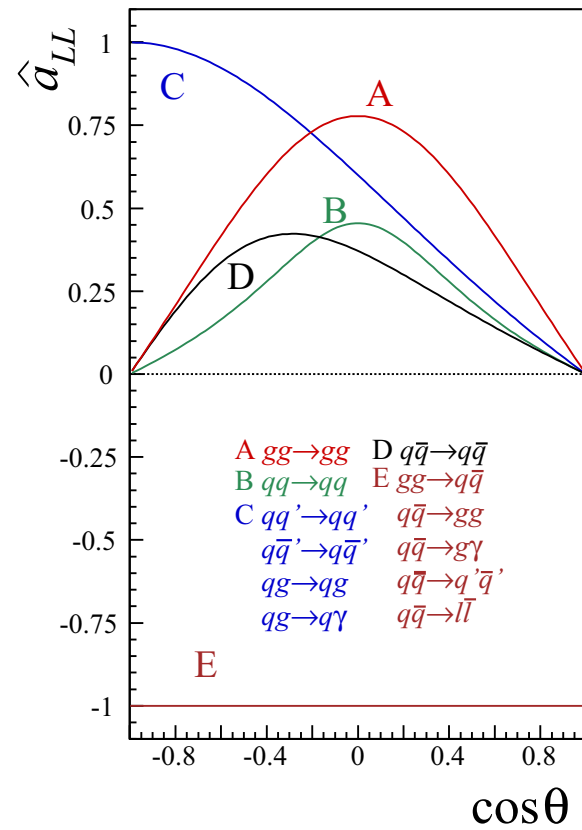


Figure 2.11: The double helicity asymmetries for subprocesses \hat{a}_{LL} . θ is the scattering angle at the center of mass system.

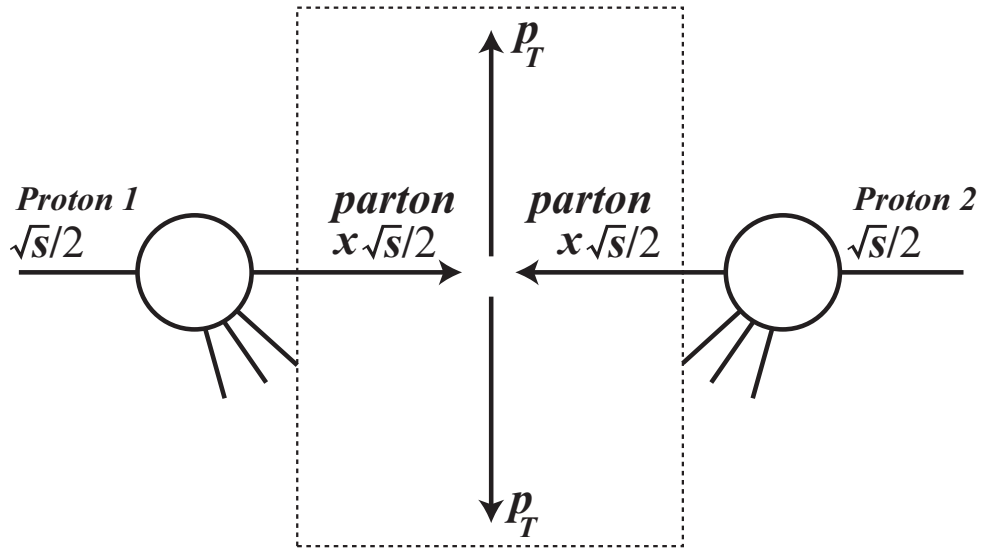


Figure 2.12: A collision with two partons have equal momentum $x\sqrt{s}/2$, when the scattering angle is 90 degrees. Fragmentation process is neglected. The p_T of scattered particle is $p_T = x\sqrt{s}/2$ and $x_T = x$ in this case.

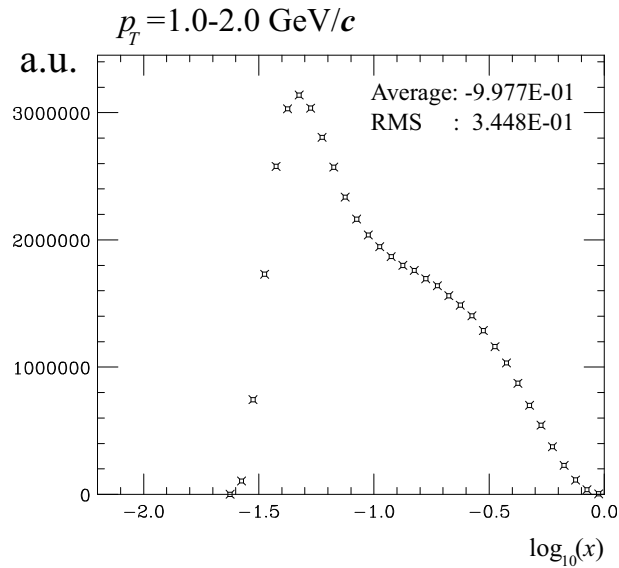


Figure 2.13: The x range contributes to π^0 production for $p_T = 1-2$ GeV/ c in pp collisions at $\sqrt{s} = 62.4$ GeV, calculated in NLO pQCD [55].

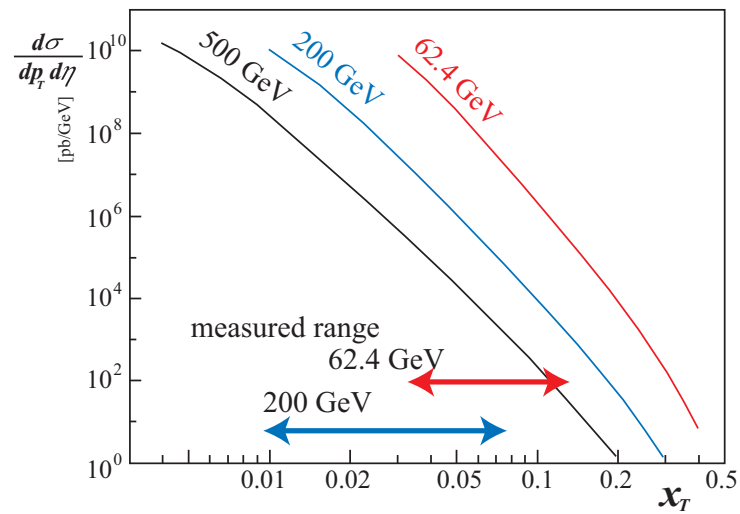


Figure 2.14: The cross section of π^0 production in pp collisions versus x_T for three different center of mass energies $\sqrt{s} = 62.4$ GeV, 200 GeV, and 500 GeV. The red arrow indicates the measured x_T range at $\sqrt{s} = 62.4$ GeV in this thesis. The blue arrow describes the measured range at $\sqrt{s} = 200$ GeV in Run 2005.

Chapter 3

Experimental Setup

3.1 Overview

This thesis is based on the data which were taken at the Relativistic Heavy Ion Collider (RHIC) with the PHENIX detector at Brookhaven National Laboratory (BNL) in the United States during the Run 2006. During Run 2006, a polarized pp experiment at $\sqrt{s} = 200$ GeV was performed for about 13 weeks (Mar.5 – Jun.5). And a polarized pp experiment at $\sqrt{s} = 62.4$ GeV followed and was for about two weeks (Jun.6 – Jun.20).

The data taken at $\sqrt{s} = 62.4$ GeV was used in this thesis. The first one third of the experiment at $\sqrt{s} = 62.4$ GeV was with transversely polarized proton beams. It was followed by the experiment with longitudinally polarized proton beams. The integrated luminosity used in this thesis is 40 pb^{-1} for longitudinal runs with average polarization of 48%.

In this chapter, RHIC is briefly introduced in Sec. 3.2. Descriptions of the experimental setup of the PHENIX detector follows in Sec. 3.3.

3.2 Relativistic Heavy Ion Collider (RHIC)

Relativistic Heavy Ion Collider (RHIC) provides high energy heavy ion collisions and polarized pp collisions. One of the major goals of the heavy ion experiment is to investigate a new state of matter which is referred to as Quark Gluon Plasma (QGP). RHIC can accelerate ions as heavy as Au up to an energy of 100 GeV per nucleon, which results in heavy ion collisions at $\sqrt{s_{NN}} = 200$ GeV. RHIC can also accelerate and collide polarized proton beams for the first time in the world, which provides us unique opportunity to study the spin property of proton through strong and weak interactions. The spin structure of proton has been studied with deep inelastic scatterings (DIS) where the interactions are mediated by virtual photons. Gluons interact at leading order in pp collisions while quarks only participate at higher order in deep inelastic scatterings (DIS). Therefore, pp collisions



Figure 3.1: RHIC accelerator complex.

are a good probe for the gluon spin contribution to the proton. The production of W in polarized pp collisions provide information on the flavor separation of the quark spin contribution. RHIC can accelerate polarized protons up to an energy of 250 GeV which results in collisions at $\sqrt{s} = 500$ GeV with design luminosity of $2 \times 10^{32} \text{ cm}^{-2}\text{s}^{-1}$.

Figure 3.1 shows an aerial view of RHIC accelerator complex and Fig. 3.2 displays its schematic. The polarized proton beam is produced at optically-pumped polarized ion source (OPPIS) [56] with the polarization of about 85%. Its intensity reaches $500 \mu\text{A}$ in a single pulse of 300–400 μs , which corresponds to $9\text{--}12 \times 10^{11}$ polarized protons. The pulse is accelerated by Linear Accelerator (LINAC) to a kinetic energy of 200 MeV. It is injected into Booster, and is accelerated up to 1.5 GeV. Then it is transferred to Alternating Gradient Synchrotron (AGS) and accelerated up to 24.3 GeV. It is injected into two independent rings at RHIC, via AGS-to-RHIC transfer line. Each beam travels in opposite direction and collides at the interaction points (IPs). Two independent beams are called the Blue (clockwise) and the Yellow (anti-clockwise) beams. RHIC has six IPs and they are referred to as IP12, IP2, IP4, IP6, IP8, and IP10 as in the case of a clock. Once RHIC was filled with beams, the beams are kept circulating in the rings to provide collisions at the IPs. When the luminosity becomes too low, beams are dumped and refilled. The sequence from injection to dump of the beam is called a fill. One fill typically lasts ~ 8 hours.

The beam in RHIC has bunch structure and each ring contains 120 bunches of polarized proton beam, with a time interval of 106 nsec. Each bunch is filled with predetermined

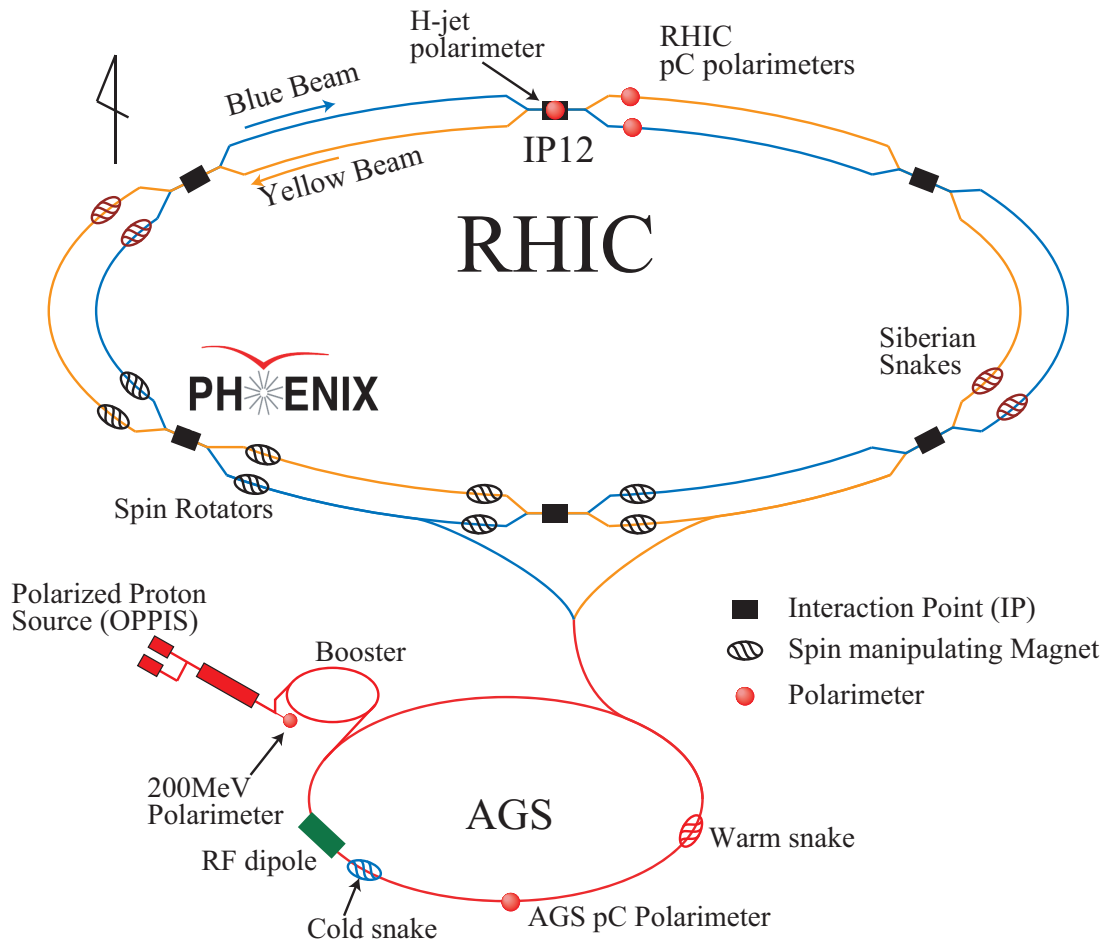


Figure 3.2: RHIC accelerator complex.

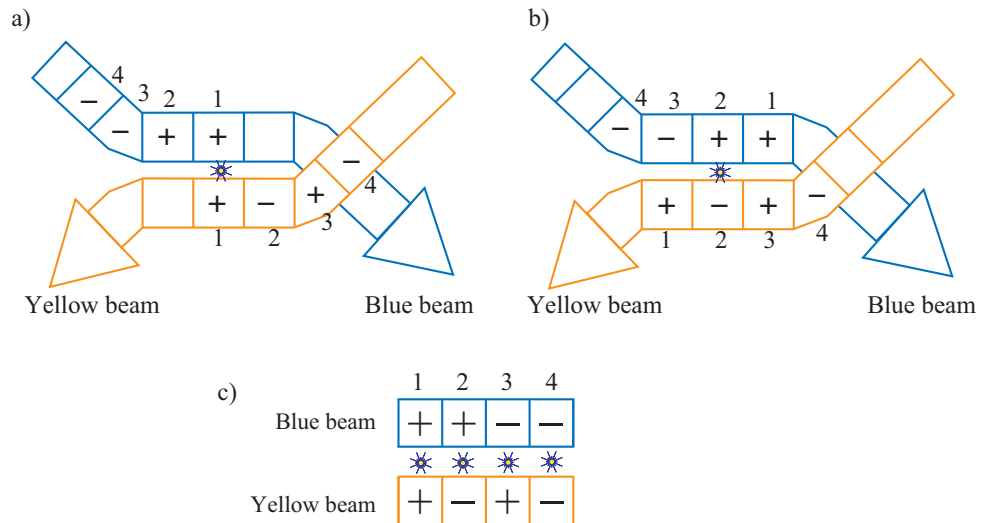


Figure 3.3: A spin pattern of RHIC polarized proton beams. An arrow represents the direction of a beam. A box corresponds to a bunch and the sign (+ and -) in the box denotes the predetermined spin state of the proton beams in the bunch. The colors of arrows and boxes represent the Blue and Yellow beams. a) Blue bunch 1 collides at Yellow bunch 1 and provide helicity same collisions. b) One beam clock after a). Blue bunch 2 and Yellow bunch 2 collide and helicity opposite collisions occur. c) The resulting spin combination of the collisions. The spin pattern provides all possible spin combination of collisions.

polarization sign. Figure 3.3 shows an example of a spin pattern assignment. The Blue beam has a spin pattern “++--” while the Yellow beam has a spin pattern “+-+-”. In Fig. 3.3a the Blue bunch 1 and the Yellow bunch 1 collide and collisions with the same helicity are obtained. One clock after Fig. 3.3a, the Blue bunch 2 and the Yellow bunch 2 collide and collisions with the opposite helicity are obtained as in Fig. 3.3b. In this way, we obtain all possible spin combinations at the same time as in Fig. 3.3c. This feature greatly reduced systematic uncertainty which comes from time dependence of the detector responses. In Run 2006, 111 bunches out of 120 bunches are filled in each ring. (A bunch out of 111 for each beam is used for tune measurements and is not used for physics measurement.) The 1st bunch of the Blue beam collides at the 81st bunch of the Yellow beam at PHENIX IP, which results in 18 non-colliding bunches. (Blue (Yellow) unfilled bunches collides Yellow (Blue) filled bunches). The non-colliding bunches can be utilized to measure single beam background. And the structure of the sequence of filled and unfilled bunches help to confirm the bunch IDs which are sent from the accelerator control system to the experiments. The exact bunch identification is crucial for precise calculation of the spin asymmetries.

3.2.1 Polarized proton source

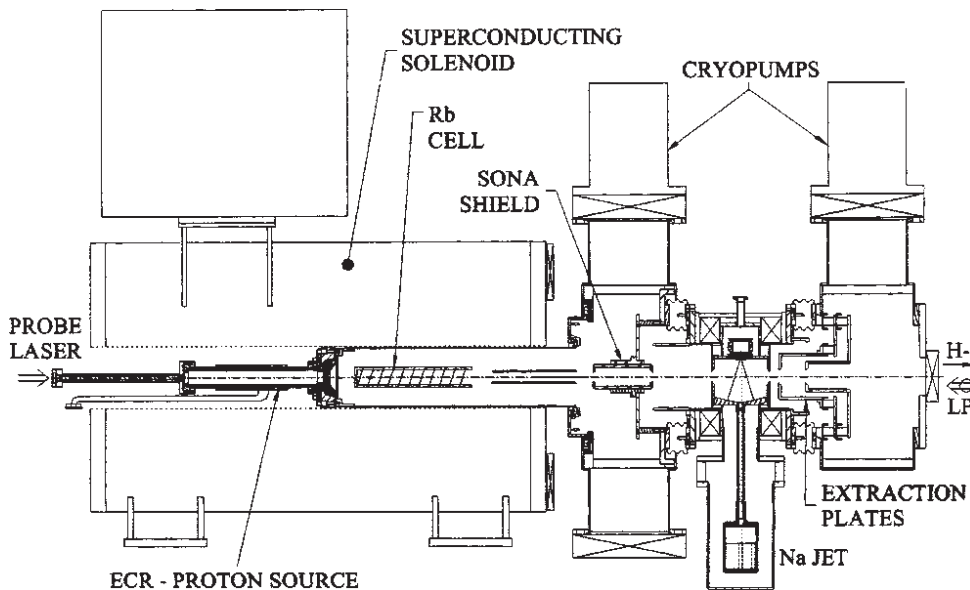


Figure 3.4: A schematic drawing of the RHIC OPPIS.

The polarized proton beam is produced at optically-pumped polarized ion source (OP-PIS) [56]. The OPPIS technique for polarized H ion beam production was developed

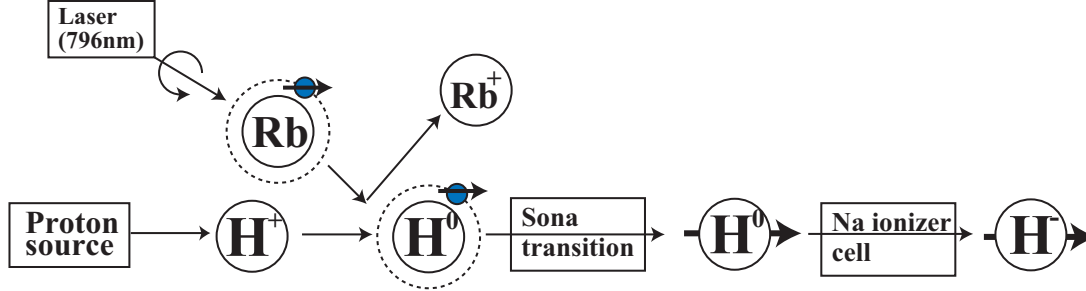


Figure 3.5: The OPPIS scheme. The labels inside circles denote the names of the atoms, which include the number of electrons, whether electrons are explicitly drawn or not. For example, the circle with the label H^0 with an electron around it does not mean H nuclei has two electrons.

in the early 80's at KEK, INR Moscow, LAMPF and TRIUMF. Figure 3.4 displays a schematic drawing of the OPPIS, and its polarizing scheme is illustrated in Fig. 3.5. The source of angular momentum is high-power lasers. Rb atoms are optically pumped by titanium-sapphire lasers and electron-spin-polarized Rb atoms are produced. H^+ atoms are created with 29 GHz Electric Cyclotron Resonance (ECR) proton source. While they pass through the Rb vapor cell, the polarized electrons are transferred from Rb to H atoms, and H^+ atoms becomes electron-polarized H^0 atoms. To prevent depolarization in the charge-exchange collisions, the optically pumped cell is situated inside the strong (2.5 Tesla) superconducting solenoid. Then the polarization is transferred from electron to the H nucleus by the Sona transition [57]. Finally, electrons are attached by the Na-jet ionizer cell and H^- ions are produced.

3.2.2 Polarization of proton beams

The proton loses its polarization during the acceleration unless special actions are taken. The proton precesses when it feels magnetic fields. The spin precession of the proton is governed by the Thomas-BMT equation[58, 59] in the laboratory frame as:

$$\frac{d\mathbf{S}}{dt} = -\frac{e}{\gamma m} [(1 + G\gamma)\mathbf{B}_\perp + (1 + G)\mathbf{B}_\parallel] \times \mathbf{S}, \quad (3.1)$$

where \mathbf{S} is the spin vector of the proton, \mathbf{B}_\perp and \mathbf{B}_\parallel are the transverse and the longitudinal components of the external magnetic fields respectively, and $G = (g - 2)/2 = 1.7928473$ is the anomalous magnetic moment of the proton, and $\gamma = E/m$ is the Lorentz factor. Since a planar circular accelerator only has the vertical guide fields ($\mathbf{B}_\perp \neq 0$, and $\mathbf{B}_\parallel = \mathbf{0}$), the proton spin vector precesses with the angular frequency of $G\gamma\omega_c$, where $\omega_c = eB_\perp/\gamma m$ is the cyclotron frequency. (A turn which corresponds to the proton's motion was subtracted

from the term $1+G\gamma$.) Thus the precession is $G\gamma$ times faster than the orbital motion, in the existence of the magnetic field. The number of spin precession per one evolution is referred to as the spin tune, ν_s . In an ideal planar circular accelerator, $\nu_s = G\gamma$.

The polarization of the proton beams are maximal at the source, and there is no repolarizing mechanism. Instead, there are many depolarizing resonances at certain beam energies. Depolarizing resonance condition is satisfied when the spin precession frequency (or the spin tune) equals the frequency of an encounter between spin-perturbing magnetic fields and the beam. Two main types of depolarizing resonances are: the imperfection resonances, and the intrinsic resonances. The imperfection resonances arise from the magnetic field error and misalignment, and occur when

$$\nu_s(= G\gamma) = n, \quad (3.2)$$

where n is an integer. Thus the imperfection resonances exist at every step of $\Delta\gamma = 1/G$, thus $\Delta E = mc^2/G = 523$ MeV in acceleration. The intrinsic resonances arise from horizontal components of the focusing fields, and occur when

$$\nu_s(= G\gamma) = kP \pm \nu_y, \quad (3.3)$$

where k is an integer, P is the super-periodicity, which is defined as the number of identical periods of the accelerator components, and ν_y is the vertical betatron tune, which is the number of the betatron oscillations per revolution. (At the AGS, $P = 12$ and $\nu_y \sim 8.8$.)

The stable spin direction is the precession axis. Thus in the absence of a spin resonance, the stable spin direction is the same as the magnetic field of the accelerator. Close to a spin resonance, the stable spin direction is perturbed away from the vertical direction by the resonance driving fields.

When a polarized beam is accelerated through an isolated resonance, the final polarization can be described by the Froissart-Stora formula[60]:

$$\frac{P_f}{P_i} = 2e^{-\frac{\pi|\varepsilon|^2}{2\alpha}} - 1, \quad (3.4)$$

where P_i and P_f are the polarizations before and after crossing the resonance respectively, and $\alpha = dG\gamma/d\theta$ is the acceleration rate per radian of the orbit angle. Thus for avoiding depolarization during a resonance crossing, $|\varepsilon|^2 \ll 2\alpha/\pi$ (results in $P_f/P_i = 1$) or $|\varepsilon|^2 \gg 2\alpha/\pi$ (results in $P_f/P_i = -1$) are required. When the beam is slowly accelerated or the resonance is strong enough (in the latter case) the spin vector adiabatically follows the stable spin direction, resulting in a complete spin flip without polarization losses. Traditionally the intrinsic resonances are overcome by using a betatron tune jump, which effectively make the resonance stronger, and the imperfection resonances are overcome with the harmonic corrections of the vertical orbit to reduce the resonance strength ε but these methods becomes difficult at high energy.

The invention of the Siberian Snake [10, 11], which generates a 180 degrees spin rotation about a horizontal axis, gave a solution to the problem. Utilizing two Siberian snakes, the stable spin direction remains unperturbed at all times as long as the spin rotation from the Siberian Snake is much larger than the spin rotation due to the resonance driving fields. The Imperfection and intrinsic resonances are both overcome by Siberian Snakes. Such a spin rotator is constructed by helical dipole magnets. The spin motion with snakes are explained in detail later in this section. At lower energy synchrotrons such as AGS with weaker depolarizing resonances, a partial snake, which rotates the spin less than 180 degrees, are sufficient to preserve the spin direction unperturbed at the imperfection resonances [61]. A 5.9 %¹ warm snake (with normal conducting magnets), together with 10% cold snake (with superconducting magnets) are utilized to overcome the depolarization resonances at AGS.

Definition of axes in the particle rest frame

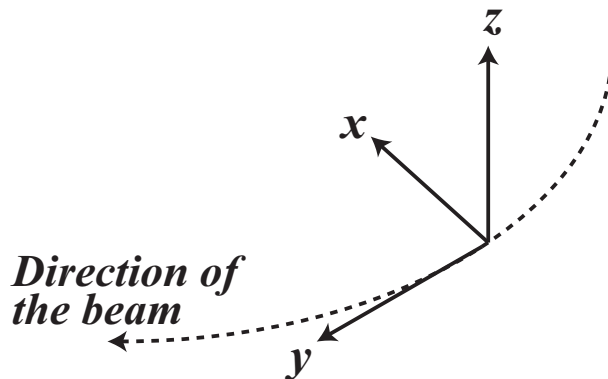


Figure 3.6: The definition of axes in the particle rest frame.

The definition of axis in the particle rest frame used in the next two subsections, is explained in Fig. 3.6. The x and y axes is in the accelerator plane. The y axis is along the direction of the beam, and the x axis is perpendicular to the y axis and faces inwards. The z axis is in the transverse direction.

Spin motion with single snake

Figure 3.7 illustrates the spin motion with a single Siberian snake configuration [62]. For simplicity, the accelerator is drawn as a combination of two bending arcs and two straight

¹The amount of the rotation induced by snakes is expressed as the fraction of 180 degrees. 5.9% snake rotates the spin by 10 degrees (180×0.059).

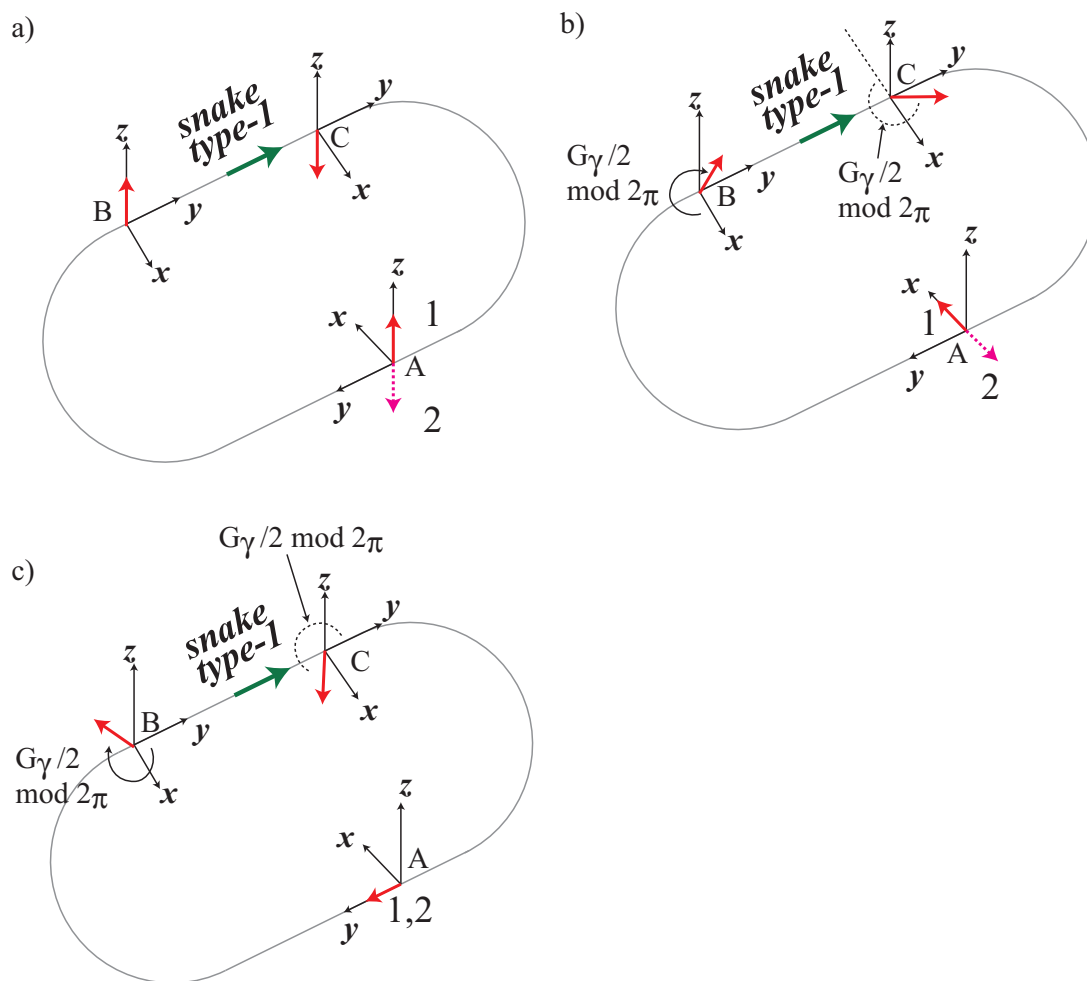


Figure 3.7: The spin motion with a single snake configuration. This is a slightly modified version of the drawing in [62]. The red arrows show the spin of the beam. The purple dotted arrows show the spin of the beam after one revolution. The green arrows represent the rotation axis of the Siberian snake.

sections. The spin precesses $G\gamma/2$ times around z axis in each bending arc ($G\gamma$ times per one turn). A Siberian snake which rotates the spin around y axis is installed in one of the straight sections. This type of snake is called ‘‘Siberian snake type-1’’. A local axis in the particle rest frame is drawn for each point (A, B, and C). The red arrows represent the spin of the beam, the purple dotted arrow represent the spin direction after one revolution. The green arrow shows the rotation axis of the Siberian snake. Figure 3.7a) shows the z component of spin motion at point A. From A to B, the spin stays in the same z direction. The spin is rotated by the snake from z to $-z$ direction between B and C. Then the spin stays the same direction $-z$ from C to A and back to the original position with the opposite spin. Therefore, the spin flips every turn. Figure 3.7b) illustrates the x component of spin motion at point A. From A to B, the spin precesses $G\gamma/2$ times around z axis. The snake rotates the spin around y axis by π and the spin precesses $G\gamma/2$ times around z axis between C and A. Therefore, the x component of spin at A flips every turn. Figure 3.7c) shows the y component of the spin at point A. In contrast to the case of z and x components, the component y remains the same direction. In total, the spin tune is $\nu = \frac{1}{2}$, which is independent of energy $G\gamma$. (The spin tune is $G\gamma$ in the absence of a snake.) Therefore, spin perturbing kick cancels every turn and does not accumulate. (For example, suppose the spin is in the y direction at point A as in Fig. 3.7c) and suffers from a spin perturbing kick around x axis at point A. The perturbing kick rotates the spin and the spin becomes $(0, \cos \chi, \sin \chi)$. Then the x and z component flips after one turn due to the snake, and the spin becomes $(0, \cos \chi, -\sin \chi) = (0, \cos(-\chi), \sin(-\chi))$. Again the perturbing kick rotates the spin in the same direction, the spin goes back to the original direction y .) This feature is very powerful in dealing with imperfection resonances. It also works for intrinsic resonances unless the betatron tune is close to a half integer. The stable spin direction is y direction at point A. At other points however, the stable spin direction depends on position and energy ($G\gamma$). For example, if we consider a point half way between A and B, the angle between the stable spin direction and the y axis is $G\gamma/4 \bmod 2\pi$. RHIC has 6 interaction points. Therefore, the dependence of stable spin direction on energy and the position cause difficulty in manipulating the spin direction at each interaction point.

Spin motion with two snakes

Figure 3.8 illustrates the spin motion with two Siberian snakes installed. As in the case of Fig. 3.7 (single snake configuration), the accelerator consists of two bending arcs and two straight sections. One of the straight sections is equipped with snake type-1. The other straight section is equipped with snake type-2 which rotates the spin by π around x axis. Figure 3.8a), b), c) show the z , x , and y components of the spin at point A. In contrast to the case of the single snake configuration, The z component stays the same and the other two components flips every turn. The spin tune is $\nu = \frac{1}{2}$ and the stable spin direction is the z direction at all times, independent of energy, and the position. (The stable direction

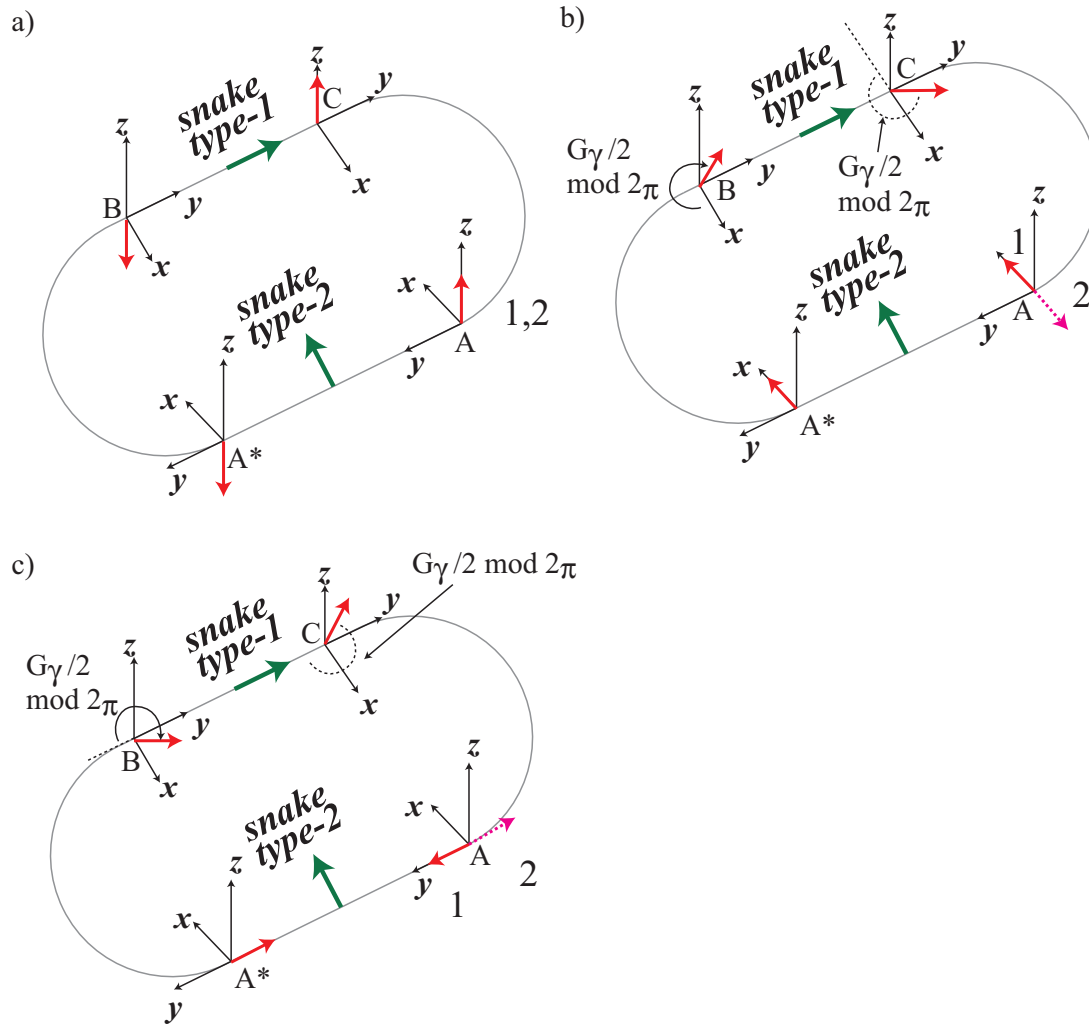


Figure 3.8: The spin motion with two snakes configuration. The red arrows show the spin of the beam. The purple dotted arrows show the spin of the beam after one revolution. The green arrows represent the rotation axis of the Siberian snake.

is opposite each other between the two arcs.) Spin perturbing kicks cancel every turn.

The snakes overcome both imperfection and intrinsic resonances unless the intrinsic resonance conditions are half integer. Such configuration with two snakes are utilized in RHIC to preserve the polarization of the proton.

Interaction points

The spin is rotated in front of the IPs by spin rotators, so that we get longitudinally polarized collisions at the IPs. The spin direction of the outgoing beams from the IPs are rotated again to the transverse direction. Fig. 3.9 shows a schematic drawing of the RHIC beams around the PHENIX interaction point.

Two large experiments, PHENIX and STAR experiments are located at IP8 and IP6 respectively. There are also smaller experiments such as PHOBOS (IP10), BRAHMS and PP2PP (share IP2). In Run 2006, PHENIX, STAR and BRAHMS were operated and the other experiments were shut down before that. In 2002, a large forward neutron asymmetry was discovered at IP12 test experiment and is utilized as PHENIX local polarimeter. Since 2004, Gas-jet absolute polarimeter experiment is being operated at IP12 which is utilized to determine the beam polarization normalization.

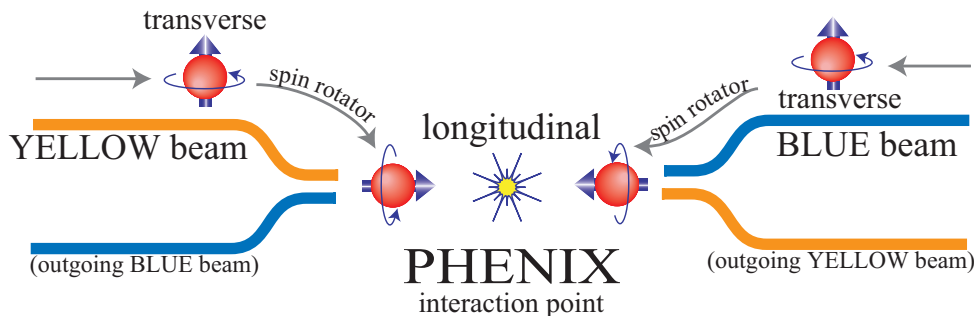


Figure 3.9: A schematic drawing of the RHIC beam near the PHENIX interaction point, when the longitudinally polarized collisions are required.

3.2.3 Polarimeters

Three polarimeters are used to measure and monitor the beam polarization. Two in RHIC and one at PHENIX experiment. Two types of polarimeters utilized in RHIC are fast carbon ribbon polarimeter (pC polarimeter) [63], and hydrogen gas jet target polarimeter (H-jet polarimeter) [64]. At PHENIX experiment, the orientation of the beam polarization is monitored by PHENIX local polarimeter [65]. These three types of polarimeters utilize a sizable single transverse spin asymmetry A_N . A_N is defined for a reaction between

transversely polarized beam and unpolarized beam (or target). It is defined as

$$A_N = \frac{\sigma_{left} - \sigma_{right}}{\sigma_{left} + \sigma_{right}} \quad (3.5)$$

where $\sigma_{left(right)}$ is the cross-section that the outgoing particle goes left(right) side when the polarization is upward in view of polarized beam. The measured raw asymmetry ε_N is $\varepsilon_N = PA_N$, where P denotes the beam polarization. Thus once the physics asymmetry A_N is known, beam polarization can be calculated as $P = \varepsilon_N/A_N$. The three types of polarimeters are introduced in this section.

Fast carbon ribbon polarimeter (pC polarimeter)

The fast carbon ribbon polarimeter (pC polarimeter) utilizes A_N in the elastic scattering between polarized proton beams and carbon target (A_N^{pC}) at very forward region, with four-momentum transfer of $-t = (0.01 - 0.02) (\text{GeV}/c)^2$. The size of A_N^{pC} in the measured kinematic region is about 1.4%. Due to the small scattering angle of protons, recoil carbons are detected instead of the scattered protons. The target should be thin for recoil carbon with small energy of 0.1 – 1 MeV to escape the target, and not to influence on the beam. However, it is required to achieve high statistics at the same time. The requirements are satisfied by using ultra-thin carbon ribbon target of 3 – 5 $\mu\text{g}/\text{cm}^2$ with a width of 10 μm is utilized.

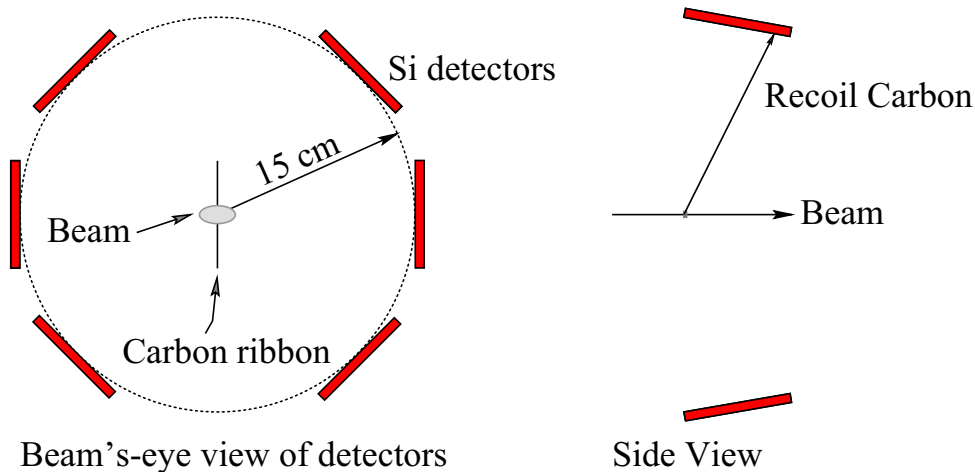


Figure 3.10: The experimental setup of the pC polarimeter. Left: beam view of the detectors. The beam runs into the paper and hit the carbon ribbon target in the center of the beam pipe. Right: side view of the detectors. The beam runs from left to right. Recoil carbon is detected with the Si detectors.

Figure 3.10 displays the experimental setup of the pC polarimeter. The target ribbon is inserted into the beam and taken out after the measurement. Slow recoil carbons are detected by the silicon detectors placed on both sides of the target. pC polarimeter collects $\sim 4 \times 10^6$ events per one measurements which is typically one minute. It corresponds to a statistical uncertainty of 4% which is smaller compared to the systematic uncertainty of 7.2% for Blue and 9.3% for Yellow beams. pC polarimeter confirms that the bunch by bunch polarization variation is within the uncertainty of the measurements. A_N^{pC} was not known in this energy and cannot be measured with the pC polarimeter system. In this respect, pC provides only relative variation of polarization for each fill. H-jet target polarimeter was utilized to obtain the absolute normalization of the polarization. The H-jet polarimeter results were used to normalize pC polarimeter results. The major source of the systematic uncertainty assigned for the beam polarizations, is the uncertainty of the absolute scale obtained with H-jet polarimeter measurement.

Polarized hydrogen gas jet polarimeter (H-jet polarimeter)

The polarized hydrogen gas jet polarimeter (H-jet polarimeter) utilizes A_N in pp elastic scattering (A_N^{pp}). Since both beam and target are polarized, A_N^{pp} can be calculated for either beam or target polarization, by averaging target or beam polarization. The relation between measured asymmetries (ε_{beam} , ε_{target}) and physics asymmetry (A_N^{pp}) is

$$A_N^{pp} = \varepsilon_{beam}/P_{beam} = \varepsilon_{target}/P_{target}, \quad (3.6)$$

where P_{beam} (P_{target}) denotes the polarization of beam (target). P_{target} is measured by Breit-Rabi polarimeter. Thus A_N^{pp} and P_{beam} can be obtained from measured asymmetries. One of the beautiful aspects in this measurement is that the physics asymmetry and the beam polarization are obtained with the same experimental setup, which reduces systematic uncertainty.

Figure 3.11 illustrates the pp elastic scattering process. The measured kinematical range is $-t = (0.001 - 0.02) (\text{GeV}/c)^2$ where the asymmetry is large. Figure 3.12 shows the experimental setup of the H-jet polarimeter. The hydrogen gas jet target crosses the RHIC beam from top to bottom at a speed of 1.6×10^3 m/sec. The density of the gas jet target is $\sim 10^2$ H atoms/sec. The target spin direction is vertical, and is reversed every 10 minutes. The recoil particle is detected with the silicon detectors which are placed on both sides of the targets. A_N^{pp} is about 4% in the measured kinematical range and the H-jet measurement provided the statistical uncertainty of 6% for a single beam for the whole run. This is not enough for measurement of polarization variation for each fill. pC polarimeter is used for this purpose instead, which provides polarization with statistical uncertainty of the same level within one minute of measurement. The absolute beam polarization obtained with H-jet target is used to calibrate the pC measurement.

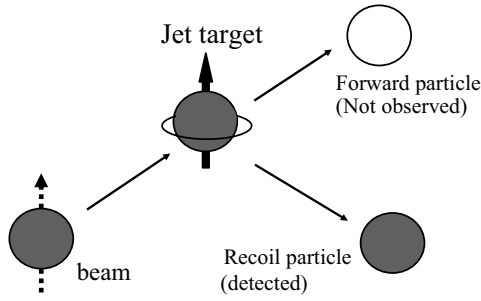


Figure 3.11: The schematics of the pp elastic scattering process. The recoil proton is observed while the forward proton is not.

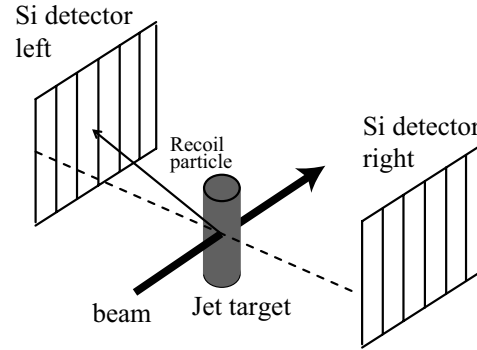


Figure 3.12: The experimental setup of the H-jet polarimeter. The beam runs through the jet target. The recoil particle is detected with the silicon detectors.

PHENIX Local Polarimeter

For the study of the gluon polarization, longitudinally polarized proton collisions are necessary while the stable polarization direction of the beam in RHIC ring is transverse as explained in Sec. 3.2.2. To obtain longitudinally polarized proton collisions, the polarization direction is rotated from transverse direction to longitudinal direction just before the interaction point. Thus the polarization orientation should be monitored at PHENIX IP. It is done by utilizing single spin asymmetry A_N of forward neutron production in polarized pp collisions. A_N vanishes when the beam polarization is in longitudinal direction. And A_N is non-zero for transversely polarized collisions. This feature is utilized to setup spin rotator magnet currents during the commissioning period. It is also used to monitor the polarization direction during the longitudinal run period.

Neutrons are detected with PHENIX Zero-Degree Calorimeters (ZDCs) and Shower Max Detectors (SMDs), which are described in detail in Sec. 3.4.2

3.3 PHENIX overview

PHENIX [66] is one of the largest experiments at RHIC, located at the 8 o'clock intersection point (IP8). PHENIX was designed to measure photons, leptons, and hadrons with excellent particle identification capability and to deal with both high-multiplicity heavy-ion collisions and high event-rate pp collisions.

Figure 3.13 is the definition of the coordinate system used in this thesis. z axis is along with the beam pipe, pointing to north, and the collision point is at the origin of the coordinate. y axis is in the vertical direction, pointing up. x axis is pointing west.

The azimuthal angle is referred to as ϕ and the zenith angle is referred to as θ . The pseudorapidity η is defined as

$$\eta = -\ln \left[\tan \left(\frac{\theta}{2} \right) \right]. \quad (3.7)$$

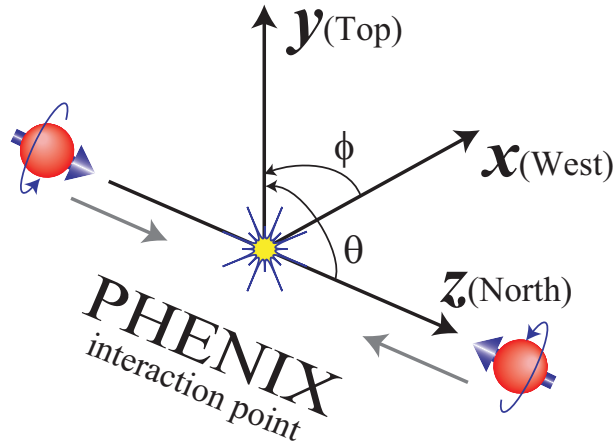


Figure 3.13: The PHENIX coordinate system.

The PHENIX experiment is composed of many sets of detectors. A collection of detectors with the same type is called a subsystem. The subsystems can be divided into three groups: two central arms, two muon arms, and global detectors. Two central arms, east and west arms, cover the pseudorapidity range of $|\eta| < 0.35$ and half in azimuthal angle. They are designed to detect photons, electrons and hadrons. Two muon arms, north and south arms, cover $1.2 < \eta < 2.4$ and $-2.2 < \eta < -1.2$ respectively with a full azimuthal coverage. They are designed to detect muons. The global detectors consist of several subsystems and measure the collision information. PHENIX has three magnets: central magnet and two muon magnets. These magnets provide magnetic fields for momentum measurement of charged particles.

Figure 3.14 displays a schematic of the PHENIX detector setup. The upper panel is a beam view of the central arm detectors. The proton beams run perpendicular to the paper, at the center of the detectors. The beam pipe is surrounded by the central arm detectors: Hadron Blind Detectors (HBD), Drift Chambers (DC), Pad Chambers (PC1, 2, and 3), Ring Imaging Čerenkov detectors (RICH), Aerogel Cherenkov detectors, Time Expansion Chamber (TEC), and Electromagnetic Calorimeters (EMCal). EMCal, which

is represented by the green boxes, are used in this thesis and is described in Sec. 3.5.1. The lower panel of Fig. 3.14 is a side view of the setup. The proton beams run as indicated by the red arrows and collide at the interaction point (IP) indicated by a star. The central arm detectors which are not drawn in the schematic, cover the IP under and over the paper. The collision vertex distributes along with the z axis approximately in a Gaussian shape, with its center at $z \sim 0$ and with a width of $\sigma \sim 60$ cm. The pole piece of the central magnet surrounds the beam pipe for $|z| > 41$ cm and it limits the acceptance of the central arms. The green boxes represent the global detectors: Beam Beam Counters (BBCs), Zero Degree Calorimeters (ZDCs). Shower Max Detector (SMDs) are placed inside ZDCs and are not displayed in the schematics. These are used in this thesis and is described in Sec. 3.4.1 and Sec. 3.4.2.

PHENIX subsystems and their acceptances and purposes are summarized in Table 3.1.

	Subsystem	η	$\Delta\phi$	Purpose
BBC	Beam-Beam Counters	$\pm(3.1 - 3.9)$	2π	Primary vertex detection. Luminosity. Time-zero. Provides level-1 trigger.
ZDC	Zero-Degree Calorimeter	± 2 mrad	2π	primary vertex detection. Luminosity. Provides level-1 trigger
DC	Drift Chambers	± 0.35	$\frac{\pi}{2} \times 2$	Charged particle detection.
PC	Pad Chambers	± 0.35	$\frac{\pi}{2} \times 2$	Pattern recognition, tracking.
TEC	Time Expansion Chamber	± 0.35	$\frac{\pi}{2}$	Pattern recognition, tracking. dE/dx .
RICH	Ring Imaging Čerenkov Counter	± 0.35	$\frac{\pi}{2} \times 2$	Electron identification. Provides level-1 trigger†
TOF	Time Of Flight	± 0.35	$\frac{\pi}{4}$	Charged hadron identification.
PbSc	Lead-Scintillator cal.	± 0.35	$\frac{\pi}{2} + \frac{\pi}{4}$	Photon and electron detection.
PbGl	Lead-Glass cal.	± 0.35	$\frac{\pi}{4}$	Provides level-1 trigger
MuTr	Muon Tracker	$\pm(1.2 - 2.4)$	2π	
MuID	Muon Identifier	$\pm(1.2 - 2.4)$	2π	Muon/hadron separation. Provides level-1 trigger†

Table 3.1: PHENIX subsystems and their acceptance and purpose. †The trigger was not used in the analysis.

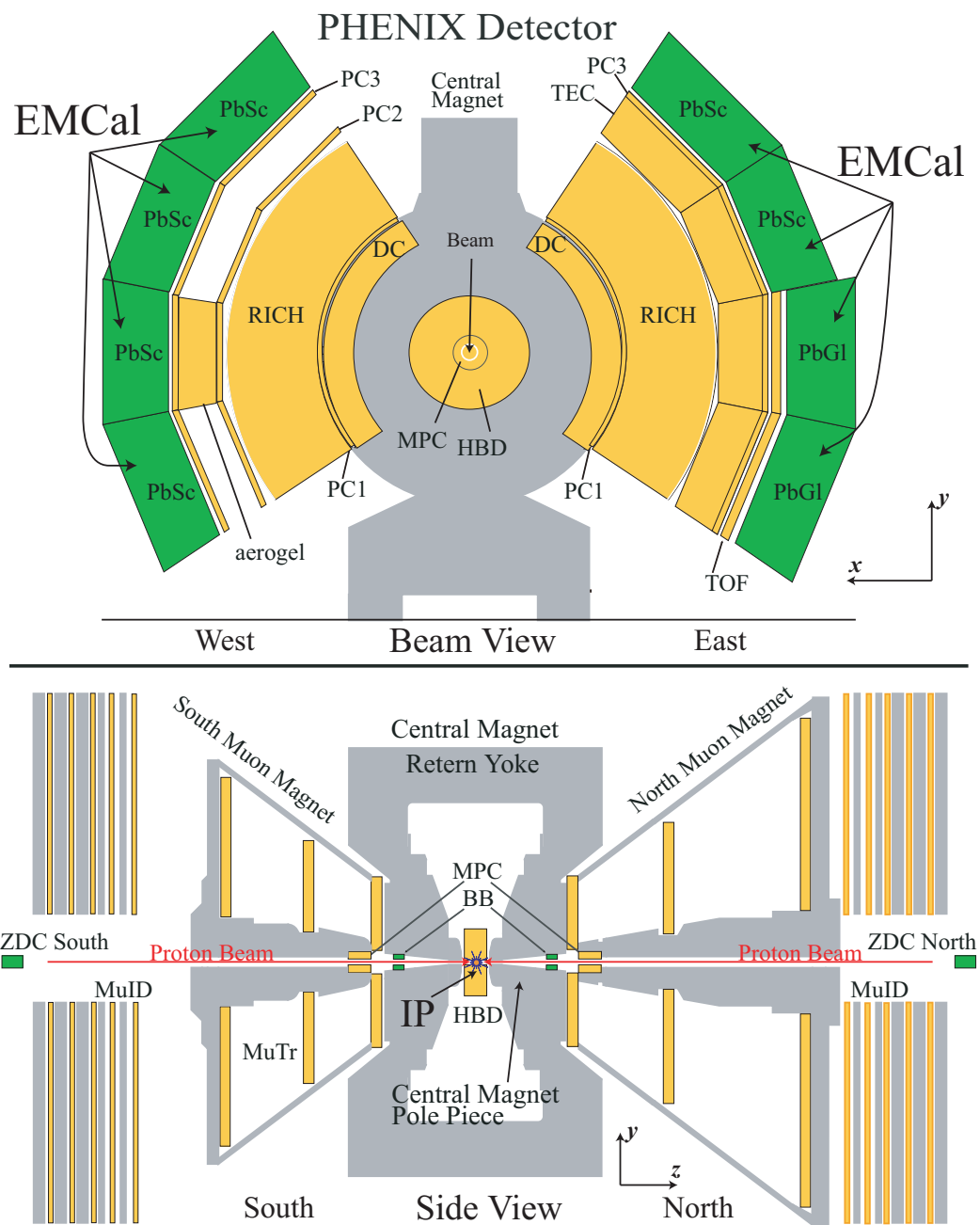


Figure 3.14: The PHENIX detector. The upper panel shows a beam view of the PHENIX central arm detectors. The eight outermost boxes represent EMCAL. The lower panel shows a side view of the PHENIX global and muon arm detectors. BBCs and ZDCs are represented by the green boxes.

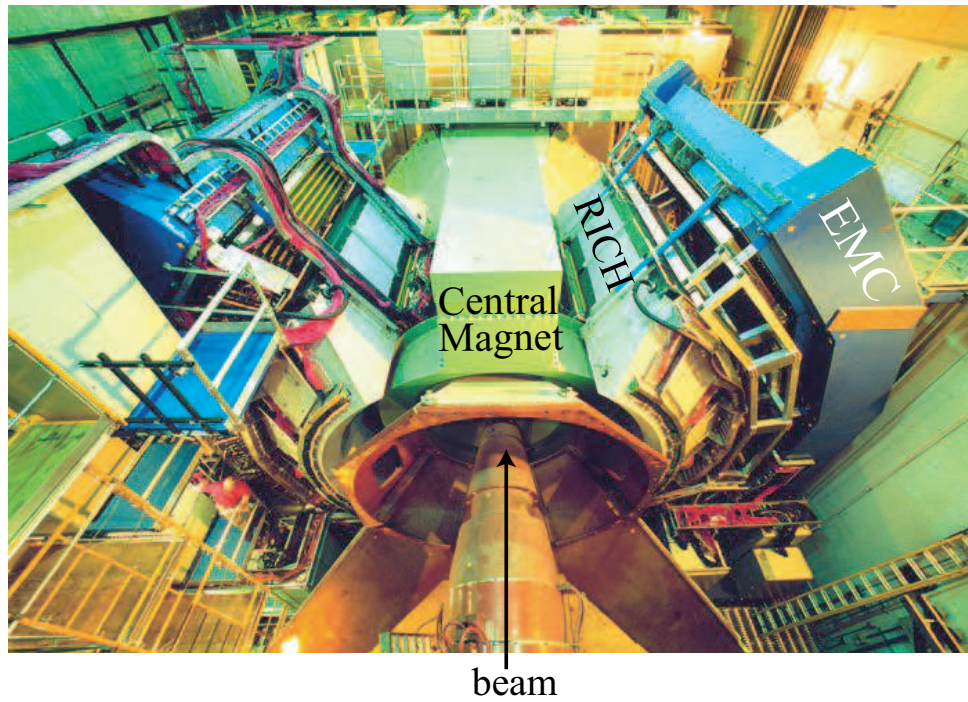


Figure 3.15: A picture of the PHENIX central arm detectors. The proton beam run as indicated by the black arrow. The IP is covered by the Central magnet and is not visible. The outer most blue structure is a support for EMCal.

3.4 PHENIX global detectors

3.4.1 Beam Beam Counter (BBC)

Beam Beam Counters (BBCs) [67] are used to determine collision time and the collision vertex position, and to provide BBC trigger. They are composed of two identical components and are placed along the beam pipe, symmetrically to the interaction point (IP). Each component is located 144 cm away from the IP. They cover forward rapidity of $3.0 < |\eta| < 3.9$. Since $+z$ direction corresponds to north and $-z$ direction to south, the different components are referred to as BBCN and BBCS. Figure 3.16 displays a picture of a BBC. The outer diameter of the BBC is 30 cm and the inner diameter is 10 cm with clearance of 1 cm between the BBC and the beam pipe. Each BBC consists of 64 hexagonal quartz Čerenkov radiators with a refractive index of ~ 1.5 , each of which is attached to a one-inch Hamamatsu R6178 photomultiplier tube. Figure 3.17 shows a picture of a pair of a 3 cm quartz radiator and a phototube. They are sensitive to charged particles with β greater than 0.7.

The BBC readout electronics chain consists of discriminators, shaping amplifiers, time-to-voltage converters (TVC) and flash ADCs (FADC). The timing and pulse height information is digitized real time and is stored in Digital Memory Units (DMUs). The BBC hit information is sent to Beam-Beam Local-Level-1 (BLL1) board to provide BBC trigger.

The collision vertex position is determined by using the time difference of the hits in two counters. Let T_N and T_S be the measured hit timing in BBCN and BBCS, respectively. The time zero (T_0) and the collision vertex position can be calculated as

$$T_0 = \frac{T_N + T_S}{2} - \frac{L}{c} \quad (3.8)$$

$$z_{\text{vertex}} = \frac{c(T_S - T_N)}{2}, \quad (3.9)$$

where L is the half of the length between the two BBCs (144 cm), and c is the speed of light. Thus when the collision vertex position is outside the BBCs ($|z| > 144$ cm), the vertex position is reconstructed as $z = \pm 144$ cm, where \pm correspond to on which side ($z > 144$ cm or $z < -144$ cm) the collision vertex is.

Vertex position cut is implemented in BBC trigger using position information obtained online. The position resolution is estimated to be ~ 5 cm online. The vertex position cut of $|z| < 30$ cm was applied and it roughly matches to the central arms' (midrapidity detector) acceptance. Two types of BBC triggers with and without vertex position cut were used during the run. In this thesis, the BBC trigger with 30 cm vertex cut is simply referred to as the ‘‘BBC trigger’’, while we explicitly write the BBC trigger without vertex cut as the ‘‘BBC no-vertex-cut trigger.’’

Offline slewing correction improves the resolution and the position resolution of ~ 2 cm was achieved offline for pp collisions.



Figure 3.16: A picture of a BBC. It consists of 64 pairs of a quartz and a phototube.



Figure 3.17: A pair of a quartz and a phototube used in the BBCs.

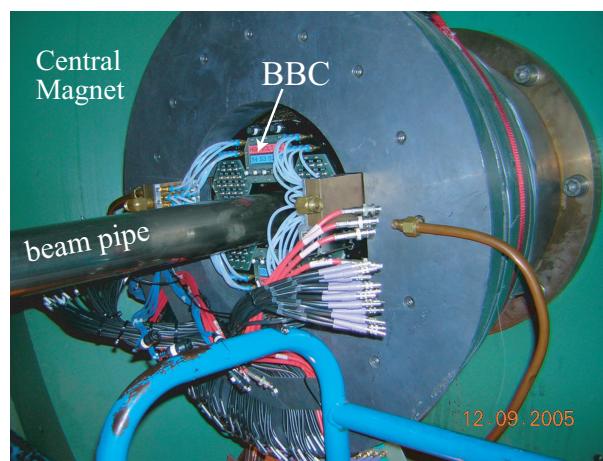


Figure 3.18: BBC installed.

3.4.2 Zero Degree Calorimeter (ZDC) and shower max detector (SMD)

Zero-Degree Calorimeters (ZDCs) [68], together with Shower Max Detectors (SMDs) were equipped to detect neutrons at very forward angle of < 2.8 mrad. They are placed at 18 m away from the IP. Figure 3.19 shows the location of the ZDCs. As in the case of BBCs, the different components are called ZDCN and ZDCS. They are placed behind the DX magnets thus most of the charged particles are swept away and neutral particles with long life, which are mainly neutrons and photons, hit the ZDCs. Neutrons can be identified as explained later. Since protons which experience elastic or diffractive scatterings at the IP may hit the beam pipes and induce showers, the resulting charged particles may hit the ZDCs. A scintillation counter are placed in front of each ZDC for charged particle veto. Figure 3.20 is a picture of a ZDC (south). It is placed between two beam pipes as explained.

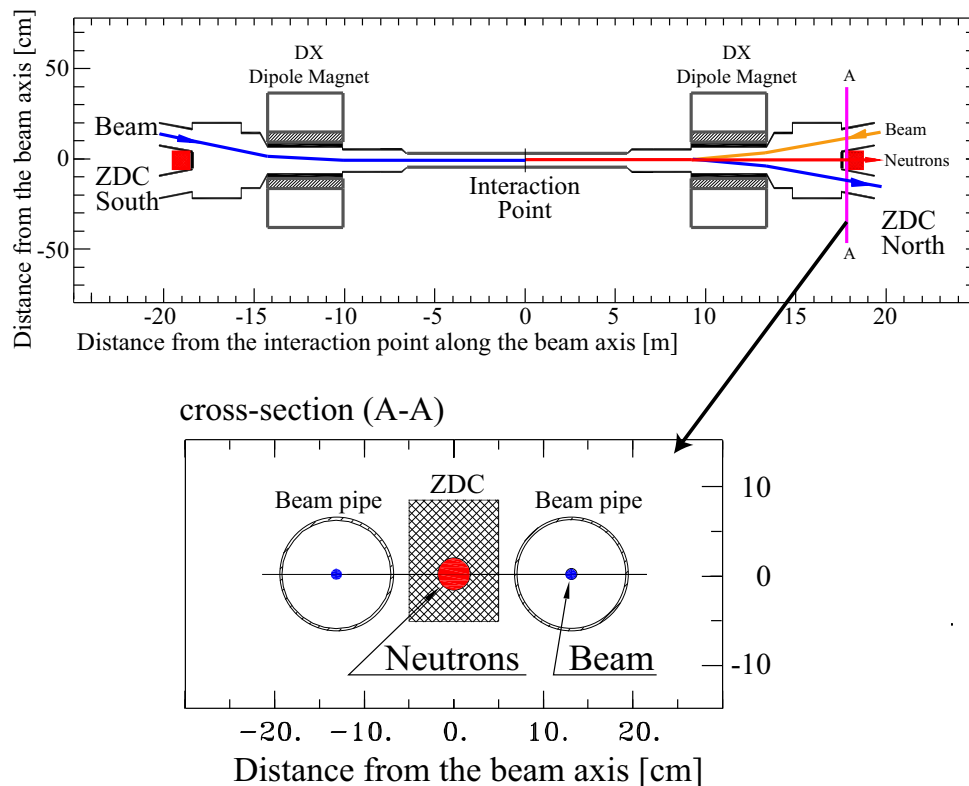


Figure 3.19: The ZDCs' location and the expected trajectories of the beams and the neutral particles such as neutrons produced in the collisions.

A ZDC consists of three ZDC modules each of which has 1.7 interaction length or

as an independent luminosity measure as well as the BBC trigger, which is explained in Sec. 3.4.1. Two types of ZDC triggers with different vertex position cuts were used during the run. One is ZDC narrow trigger which is defined with the vertex position cut of $|z| < 30$ cm, and the other is ZDC wide trigger which is defined with the vertex position cut of $|z| < 150$ cm. Since the width of the vertex position variation is ~ 60 cm, most of the collisions are covered by the ZDC wide trigger.

Comparison between BBCs and ZDCs can be used to estimate the uncertainty on luminosity measure. The method of evaluation of luminosity uncertainty is described in Sec. 4.4.

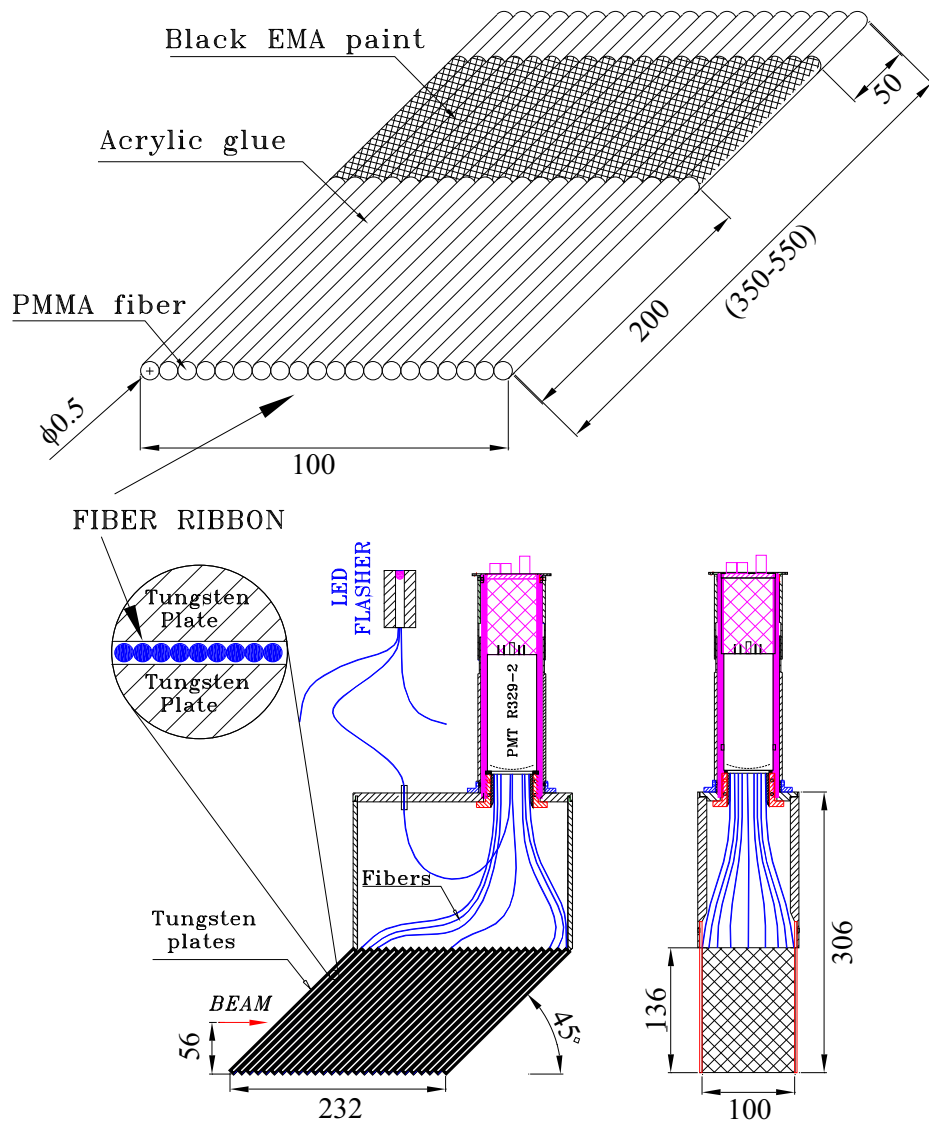


Figure 3.21: ZDC Mechanical Design.

3.5 PHENIX central arms

3.5.1 Electromagnetic calorimeter (EMCal)

The PHENIX Electro-Magnetic Calorimeter (EMCal) [69] plays an important role for the detection of photons from $\pi^0 \rightarrow \gamma\gamma$ decay. The EMCal covers central rapidity ($|\eta| < 0.35$) and half in azimuthal angle. ($\Delta\phi = \frac{\pi}{2} \times 2$). The PHENIX EMCal is composed of two types of calorimeters. Lead-Scintillator (PbSc) calorimeters, and Lead-Glass (PbGl) calorimeters. The basic parameters for EMCal are summarized in Table 3.2. A box with a label of PbSc or PbGl in Fig. 3.14 corresponds to a sector. PHENIX has 8 sectors of EMCal, 6 of them are PbSc type, and other two are PbGl type. Both type covers pseudorapidity range of $|\eta| < 0.35$. PbSc covers $\frac{\pi}{2} + \frac{\pi}{4}$ in azimuthal angle, and PbGl covers $\frac{\pi}{4}$. The minimum unit of EMCal with individual read-out is called a tower.

A PbSc sector is composed of 3×6 super-modules. A PbSc super-module consists of 6×6 modules, each of which consists of 2×2 towers. A PbGl sector is composed of 12×16 super-modules, each of which consists of 4×6 towers.

The total numbers of towers are 15552 for PbSc and 9216 for PbGl. A detailed explanation for each type follows in this section.

	PbSc	PbGl
general parameters		
radiation length (X_0)	21 mm	29 mm
Moliere radius	~ 30 mm	37 mm
channel(tower)		
cross section	52.5 mm \times 52.5 mm	40 mm \times 40 mm
depth	375 mm (18 X_0)	400 mm (14 X_0)
η coverage	0.011 [rad]	0.008 [rad]
ϕ coverage	0.011 [rad]	0.008 [rad]
super-module		
number of channels	144 (12×12)	24 (4×6)
sector		
number of super-modules	18 (3×6)	192 (12×16)
whole system		
number of sectors	6	2
number of channels	15552	9216
η coverage	0.7	0.7
ϕ coverage	90 (deg) + 45 (deg)	45 (deg)

Table 3.2: Basic parameters of two types of PHENIX EMCal.

Lead Scintillator Calorimeter (PbSc)

The PbSc is a sampling calorimeter which is composed of 65 lead tiles and 66 scintillator tiles, stacked in alternate way. The thickness of lead tile (scintillator tile) is 1.5 mm (4.0 mm). The scintillator is made of polystyrene (the bulk material) and 1.5% of p-Terphenyl (the primary fluorescent material) and 0.01% of POPOP (wavelength shifting material) are added.

A PbSc module consists of four towers, which are optically isolated and read out individually. Figure 3.22 shows the internal view of the module. A module has 64 holes for the read-out fibers to pass through, with 1.2 mm diameter and 9.27 mm spacing. The read-out fibers are made of wave length shifter (0.5% POPOP) which pass through the entire module from the back side to the front side then return to the back side after following smooth curves. The both edges of the fibers are gathered and attached to FEU115M phototubes (1 inch diameter, multi-alkali photocathode, made by MELS in Russia.) The attenuation length of the fiber is approximately 1 m, which affects the linearity of the energy measurement.

The four edges of the scintillator tiles are coated by aluminum to reflect the scintillation light except one corner at the center. For calibration, a fiber is inserted in the center of the module and provides laser light into four towers through the corners. Figure 3.23 shows a schematic of the laser calibration system [70]. The laser light is split in three steps and delivered into 3888 modules. The laser amplitude is monitored with a phototube and photo diodes in all the light splitters. The laser calibration system is to normalize the calibration change, due to the operation conditions. The gain of the amplifier for the photo diodes is monitored by test pulses.

The performance of PbSc was evaluated with the test experiments with AGS at BNL and Super Proton Synchrotron (SPS) at CERN. Figure 3.24 displays the energy resolution for electromagnetic showers as a function of incident energy, obtained by the test experiments. It is well described by

$$\frac{\Delta E}{E} = \frac{8.1\%}{\sqrt{E(\text{GeV})}} \oplus 2.1\% \quad (3.10)$$

The 8.1% in the first term of Eq. 3.10 is close to the expected resolution from sampling as predicted by GEANT. The main contributor to the constant term is intrinsic non-uniformity, in particular tower boundaries, hot spots at fiber positions and shower depth fluctuations. There will be a loss in the calorimeter response when a particle hits the corner of the towers. Shower depth fluctuations are responsible for the variations in the amount of the light seen and in the energy leakage via the front and the back surface of the calorimeter.

The position resolution depends on the incident angle of the beam due to the fluctu-

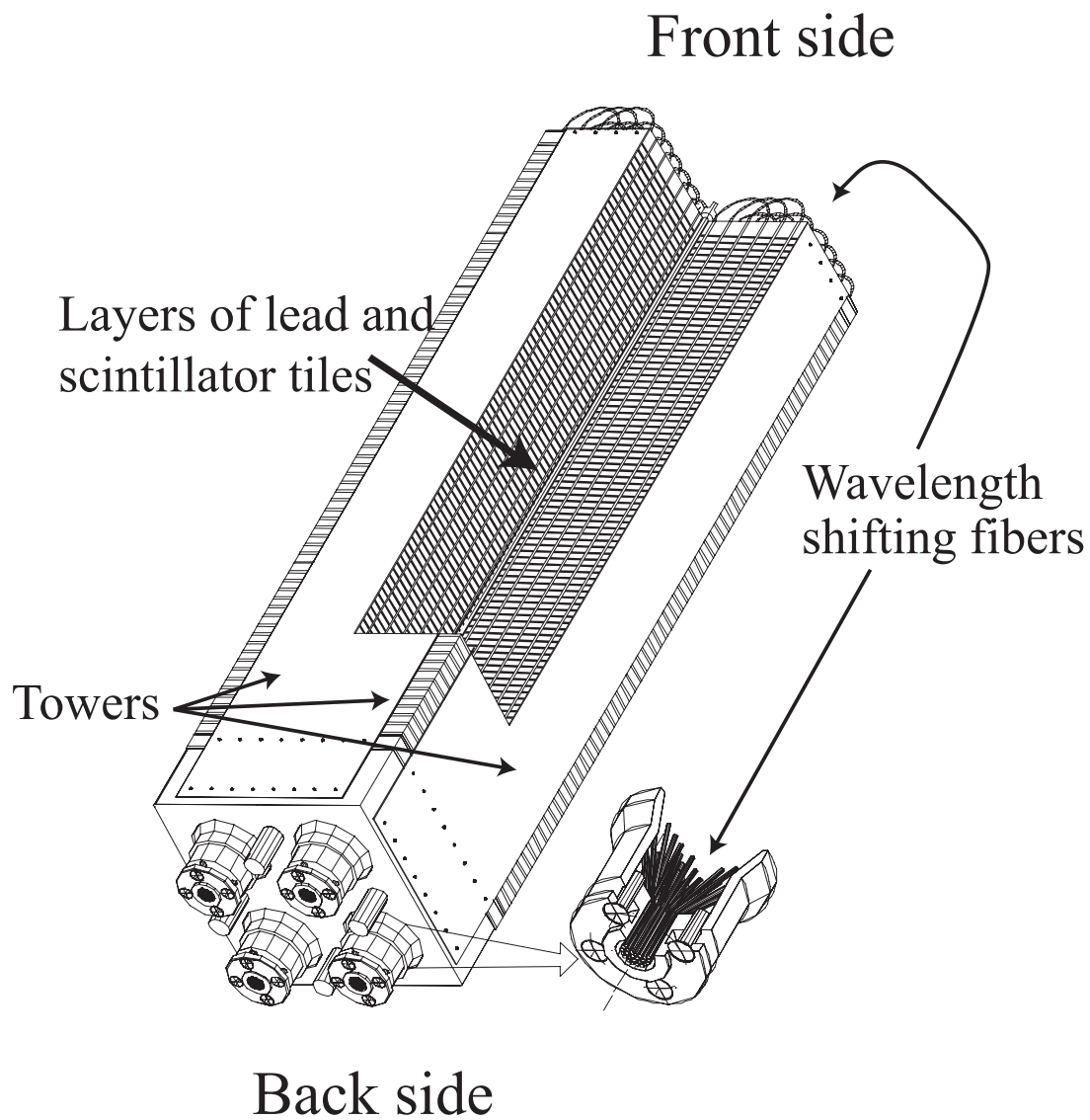


Figure 3.22: A module of PbSc. A module is composed of four towers, which are read-out individually.

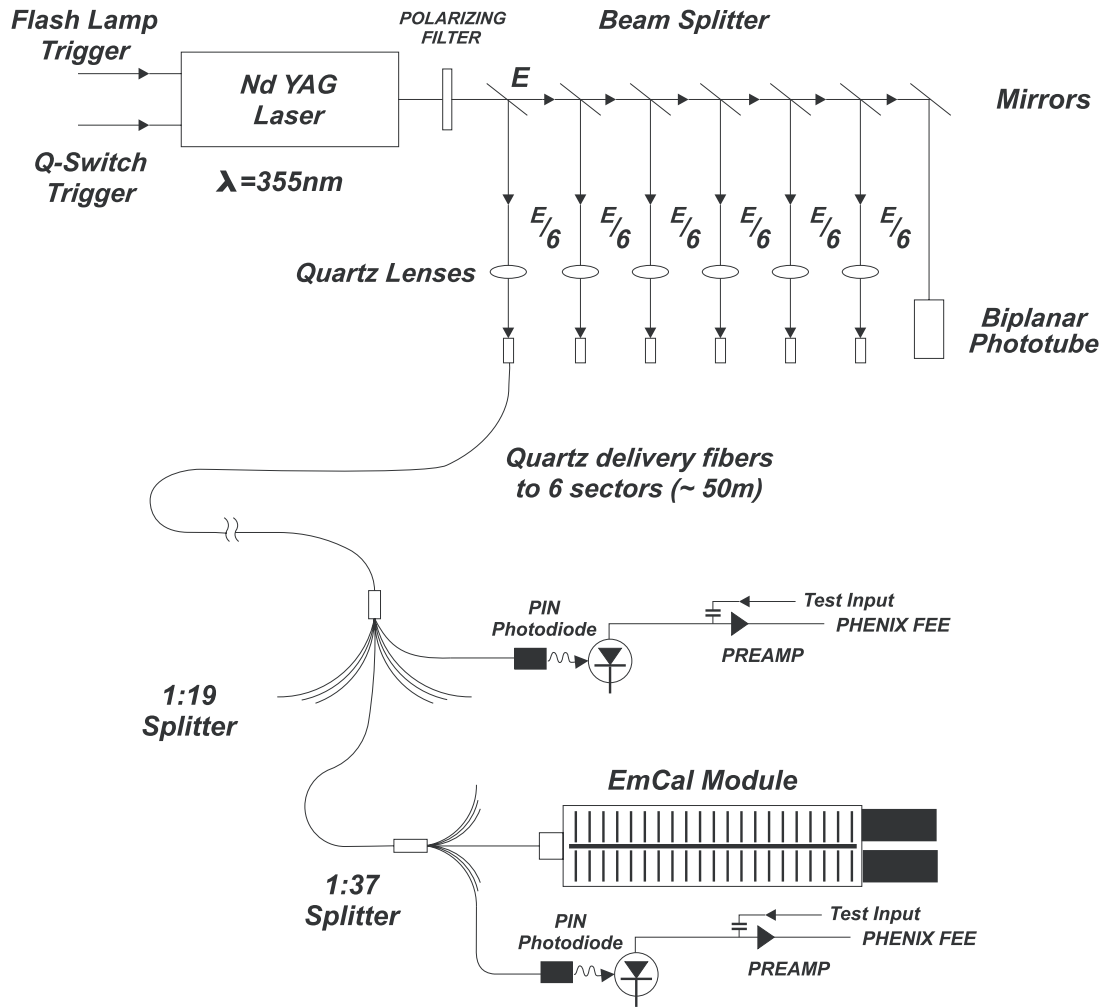


Figure 3.23: PbSc calibration

ation of the shower depth. The resolution can be expressed as

$$\Delta x = \Delta x_0 \oplus L \sin \theta, \quad \Delta x_0 = 1.55 \text{ mm} \oplus \frac{5.7 \text{ mm}}{\sqrt{E(\text{GeV})}}, \quad (3.11)$$

where L is $\sim X_0$ ($= 21 \text{ mm}$) and θ is the incident angle to the PbSc tower axis. These results are reproduced by GEANT simulation [71]. The energy deposit for a minimum ionizing particle (MIP) was measured to be 270 MeV.

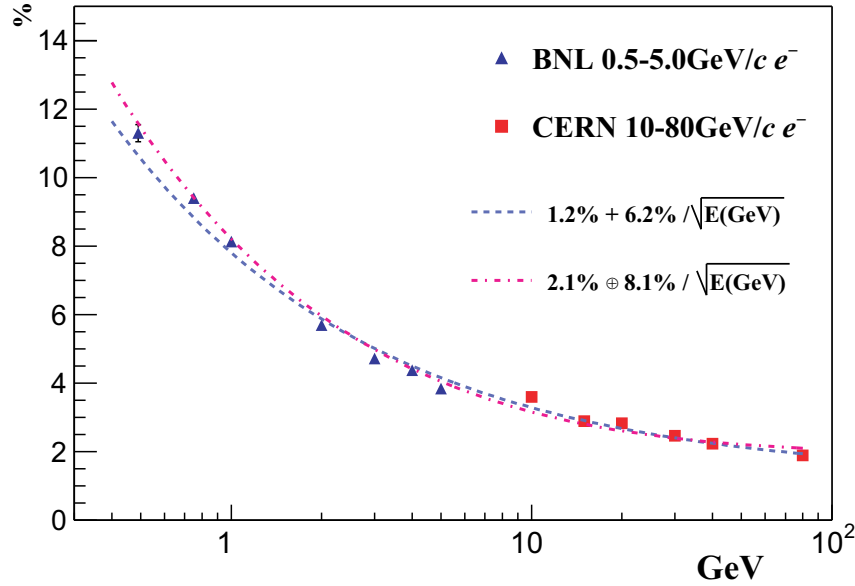


Figure 3.24: The energy resolution of PbSc for electromagnetic shower as a function of the incident energy. The vertical axis shows $\Delta E/E$.

Lead Glass Calorimeter (PbGl)

The PbGl is a Čerenkov type calorimeter. The modules are previously used in WA98[72] experiment at CERN and re-used at PHENIX. PbGl occupies two sectors out of eight.

A lead glass element has $4.0 \text{ cm} \times 4.0 \text{ cm}$ cross section and is 40 cm long. This element is the minimum unit of PbGl and is called a tower. 4×6 towers are gathered to form a super-module. A schematic of a super-module of PbGl is shown in Fig. 3.25. The towers within the super-module are optically isolated with aluminized Mylar foils and each tower is attached to an FEU-84 phototube. Steel sheets of 0.5 mm thickness are used to house the entire towers and PMTs. The PbGl LED calibration system are installed to monitor the gain drift. Three LEDs with different wave length are placed on the front of every

super-module. The mirror foil on the top surface have a hole for each PbGl tower for LED light to enter. A polystyrene reflective dome covers the LED system.

The intrinsic performance of PbGl was evaluated with the test experiments with AGS at BNL and with SPS at CERN. Figure 3.26 shows the energy resolution for electromagnetic showers obtained by the test experiments. No significant dependence on incident angle was observed. The obtained resolution is well described as

$$\frac{\Delta E}{E} = \frac{5.9 \%}{\sqrt{E \text{ (GeV)}}} \oplus 0.8 \% \quad (3.12)$$

The position resolution for electromagnetic showers are also measured and is described as

$$\Delta x = \frac{8.4 \text{ mm}}{\sqrt{E \text{ (GeV)}}} \oplus 0.2 \text{ mm} \quad (3.13)$$

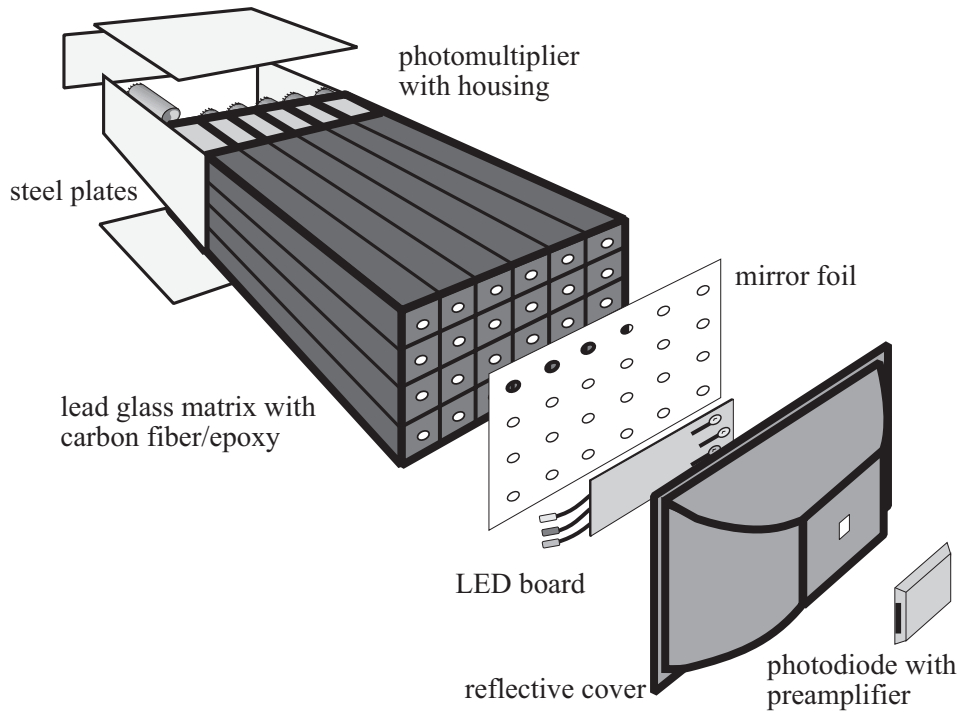


Figure 3.25: PbGl.

The response of PbGl to hadrons is different from that of PbSc since PbGl is based on Čerenkov detection. The deposit energy is suppressed for hadrons due to its Čerenkov threshold (106 MeV/c for charged pions). The energy deposit is examined at the test

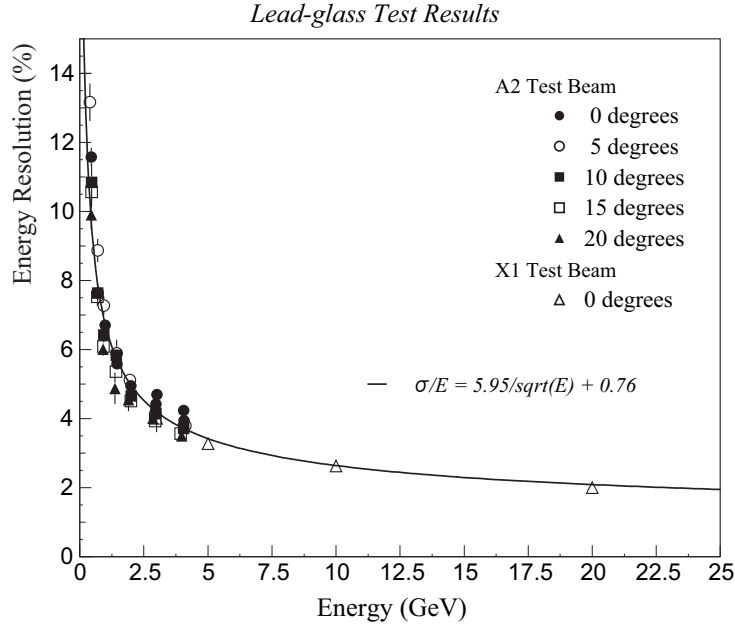


Figure 3.26: The energy resolution of PbGl for electromagnetic shower as a function of the incident energy. The vertical axis shows $\Delta E/E$.

experiments. The deposit energy of charged pions is ~ 460 MeV for 1 GeV/ c , and ~ 540 MeV for 4 GeV/ c .

3.5.2 EMCal front end electronics

Signals from PMTs are processed in the front end electronics (FEE) and the energy, time of flight, and energy sum for high-energy photon trigger are derived. The analog signals are processed by ASIC (application specific integrated circuit) chips on FEE. One ASIC chip processes four adjacent towers forming 2×2 block, which is the minimum unit for trigger decision. Figure 3.27 shows a block diagram of the analog part of FEE. There inserted a passive integrator with 93Ω resistor and 500 pF capacitor and bias voltage of +4 V is applied to allow negative pulse input from the phototube. The current profile from the phototube is converted to a voltage profile at point A, whose rise time is less than 5 nsec. It is not sensitive to the base shift and the fast voltage pulse is used for time of light measurement.

The charge is collected onto the capacitor so that the voltage at the point B in Fig. 3.27 follows the charge collected, that is the collected energy. The voltage profile has a rise time of ~ 100 nsec and long decay time of the order of $10 \mu\text{sec}$. Thus the profile is almost a step function with the amplitude proportional to the deposit energy. All of the remaining

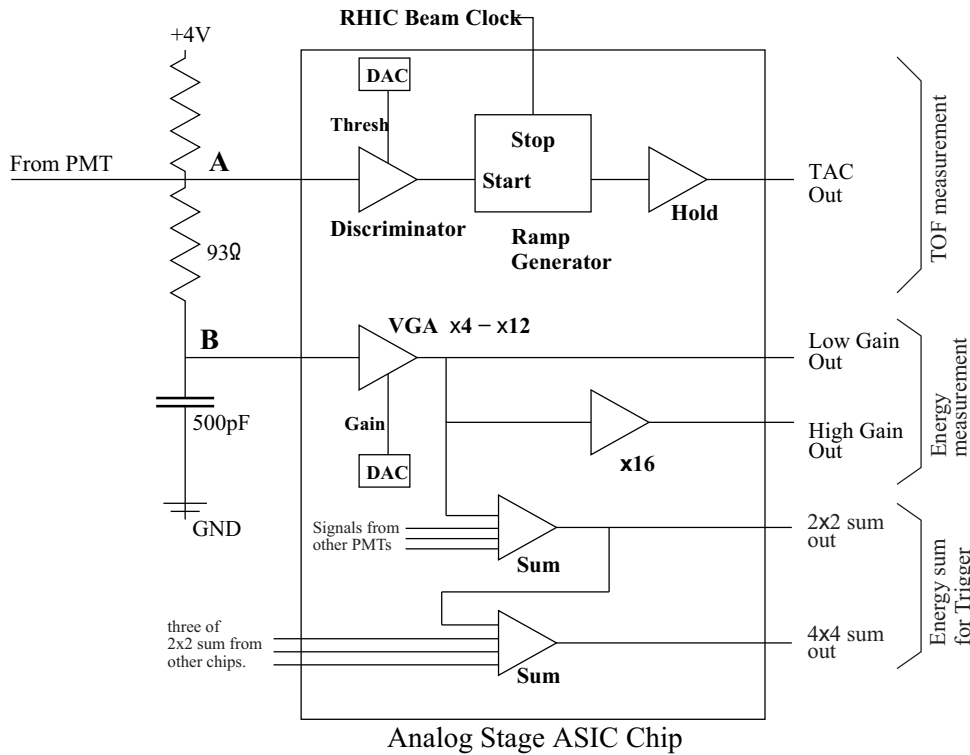


Figure 3.27: A block diagram of the analog part of EMCAL FEE. One ASIC chip handle signals from four PMTs. Only a flow for a PMT is shown.

analog processing stages up to ADC conversion are carried out within an ASIC chip[73], as shown in the Fig. 3.27. The signal is amplified by variable gain amplifier (VGA) with a gain of $\times 4 - \times 12$ with 5 bit resolution. The gain of VGAs can be remotely controlled via ARCNet [74]. ARCNet is a local area network protocol available worldwide and is utilized for the slow control of PHENIX. This allows the readout electronics to compensate, to within a few percent over its range, for gain variations among phototubes which share the same high voltage supply. This feature is useful for the trigger circuit and maximizing the ADC dynamic range for all channels. Then the signal is divided into three. One is further amplified by 16 and used for energy measurement and is called “high gain” (HG). Another signal is used for energy measurement without further amplification and is called “low gain” (LG). The other signal is used for energy sum for the trigger decision. The mechanism to have both HG and LG is to maintain good resolution for the wide energy range of 20 MeV – 30 GeV. The transition energy of the valid range between LG and HG is about 1 GeV. The signals from four PMTs in the same ASIC chip are summed and provide the energy sum of 2×2 towers for trigger decision. The analyzed data in this thesis is obtained with 2×2 energy sum trigger, which is referred to as high p_T photon

trigger. One unit of the trigger decision, a group of 2×2 towers, is called a trigger tile. When a photon hit the center of a tower, 80% of the energy is deposited at the tower. Therefore, the size of the trigger tiles is enough to trigger electromagnetic showers. Two trigger circuits were used for a single tile of 2×2 energy sum and alternated in each beam clock count. In other words, trigger circuits are different for even and odd bunches. The slight difference in trigger threshold in two circuits may lead false spin asymmetries. Thus the counts in even and odd bunches are treated separately as explained in Sec. 4.5.1.

The analog outputs of TAC, LG and HG voltages are kept in analog memory units (AMUs), which consist of an array of capacitors. When a trigger is issued, the stored analog signals are read out and digitized, then sent to the PHENIX Data Collecting Modules (DCMs), which is described in Sec. 3.7.

The analog signals can be stored for 62 beam clocks. It corresponds to $7 \mu\text{sec}$ and longer enough than $4 \mu\text{sec}$, which is needed for the trigger decision.

3.6 PHENIX trigger system

A PHENIX Level-1 trigger is to pre-select events with potential interests before high-level processing of events, based on primitive information from the PHENIX detector subsystems. The Level-1 is fully pipelined and the decision is made whenever 9.4 MHz RHIC beam clock is received. A PHENIX Level-2 trigger is based on data which are processed after accepting Level-1 trigger, thus is data-driven.

We only introduce Level-1 trigger here since the data used in this thesis are fully collected with Level-1 trigger and without Level-2 trigger.

The PHENIX Level-1 trigger consists of two types: Local Level-1 (LL1) triggers and a Global Level-1 (GL1) trigger.

A LL1 trigger communicates directly with a detector or a set of detectors for trigger decisions. Then the LL1 trigger decisions are sent to the GL1 system and it combines the trigger information to provide the final decision. In the GL1 system, prescale, and logical operations such as AND and OR of LL1 trigger decisions can be made.

Among the PHENIX LL1 triggers, the BBC, BBC no-vertex-cut, ZDCwide, high- p_T photon, and pZDC triggers are used in this analysis. The BBC, ZDC, and high- p_T photon triggers are already introduced in Sec. 3.4.1, 3.4.2, and 3.5.1 respectively. The pZDC trigger is defined as a coincidence of a hit in either BBC and a hit in either ZDC. The trigger is symbolically expressed as “(BBCN or BBCS) and (ZDCN or ZDCS)”.

3.7 PHENIX DAQ system

Figure 3.28 shows a schematic of the PHENIX Data Acquisition (DAQ) System. Since the RHIC beams have the bunch structures, the PHENIX detector has to be synchronized

with the RHIC beams. 9.4 MHz of RHIC clock is provided by the accelerator control system, and is transferred to the Master Timing Module (MTM). MTM distributes the clock into Global Level-1 (GL1) and the Granule Timing Modules which are equipped into all subsystems.

The clock and the trigger decision issued by GL1 is sent to the Front-end Electronics Modules (FEMs). FEMs manipulate FEE to process the raw signals of the PHENIX detectors. FEE has buffering scheme and store the processed signals for up to 40 bunch crossings for read-out by request from the trigger decisions.

When a trigger decision is issued by GL1, FEMs send processed signals into Data Collecting Modules (DCMs). Information is collected by Partitioner and then sent to Sub-Event Buffers (SEBs). SEBs then transfer the data on request to a set of Assembly and Trigger Processors (ATPs) under the control of the Event-Builder Controller (EBC). Here detector-by-detector information is rearranged to event-by-event information.

The rearranged data are sent to online monitoring system to online level quality control, and sent to DAQ Linux machines to record it in hard drives. Then they are recorded into tapes (HPSS). PHENIX DAQ data taking ability is about 5 kHz.

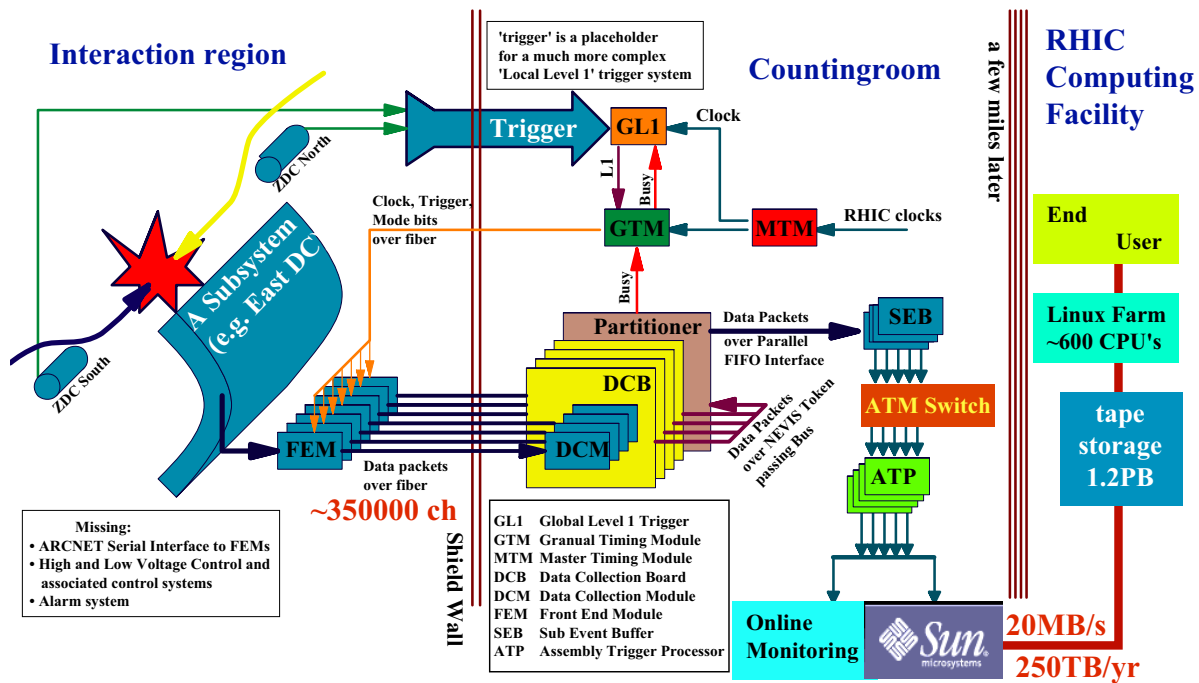


Figure 3.28: PHENIX DAQ system.

Chapter 4

Analysis

4.1 Overview

In this chapter, the analysis procedure to extract double helicity asymmetry A_{LL} of π^0 is explained. A_{LL} is defined as Eq. 2.38. It is calculated experimentally by the following formula.

$$A_{LL} = \frac{1}{|P_B||P_Y|} \frac{N_{++} - RN_{+-}}{N_{++} + RN_{+-}}, \quad R = \frac{L_{++}}{L_{+-}}, \quad (4.1)$$

where $P_{B(Y)}$ denotes the beam polarization in the Blue (Yellow) RHIC ring, N is the π^0 yield, L is the luminosity and $++$ ($+-$) represents the helicity states of the proton beams. R is the relative luminosity between bunches with the same and opposite helicities. The proton beams are transversely polarized in RHIC rings, and the spin is rotated from transverse to longitudinal direction by the spin rotators as explained in Sec. 3.2.2. Since the magnet currents of the spin rotators may not be adjusted properly, the polarizations may have residual transverse components at the IP. Therefore, in addition to (absolute) beam polarizations, beam polarization orientations are needed.

The necessary components for A_{LL} measurement are

- beam polarizations
- beam polarization orientations
- relative luminosity
- spin dependent π^0 yields.

They are explained in the following sections.

4.2 Run selection

DAQ is usually stopped after one hour of data taking and restarted even if nothing wrong is found in the detector or the accelerator. A period during which DAQ is started and stopped is called a run. It is for convenience in the analysis. For example, time dependence of the detector performance is studied run-by-run. On the other hand, the uncertainties of relative luminosity, which is discussed in Sec. 4.4, is studied fill-by-fill since it depends on the characteristics of the beams which are correlated among the runs in the same fill. Asymmetry calculations were performed run-by-run, or fill-by-fill, which is determined with the statistics and the trigger efficiency. See Sec. 4.5.1 for detail.

In Run 2006, data reconstruction was started during the data taking. For some runs PHENIX calibration database was not ready and reconstruction failed. It was not due to the detectors used in this analysis. Such runs were not available at that time and the amount was about 10%. Since recovering such small amount of data would not change the results and do not add significance of the results, such runs were not included. In total, 98 runs were available in Run 2006 at $\sqrt{s} = 62.4$ GeV. Runs without some necessary information or with wrong detector or accelerator settings, were discarded and not analyzed. A fill (fill 8035) was removed due to missing polarization information. Another fill (fill 8059) was removed since the STAR magnets frequently tripped and recovered, which was known to affect the polarization orientation at the PHENIX IP. After these selections, 86 runs (18 fills) survived and were analyzed. Out of 18 fills, 7 fills are from the transverse run period, and 11 fills are from the longitudinal run period.

Figure 4.1 displays the raw rate of BBC trigger as a function of run number. The BBC trigger serves as a luminosity measure for the PHENIX and the BBC trigger detects inelastic events with a cross section of $\sigma_{BBC} = 13.7$ mb [75]. It corresponds to 40% of inelastic scatterings in pp collisions at $\sqrt{s} = 62.4$ GeV. The inset in Fig. 4.1 is a closeup of a certain period of the raw trigger rate. A group of points corresponds to a fill and the rate, or the luminosity, decreases with increasing run number. The beams were dumped after luminosity decreased by a factor of $2 \sim 3$. The DAQ has data recording ability of about 5 kHz and are able to take data with multiple triggers. Since the BBC trigger efficiency for inelastic scatterings (which include π^0 production) is only 40%, the high- p_T photon trigger was utilized during the run to collect π^0 data used in this thesis. See Sec. 4.5.1 for the trigger performance. A typical setting of trigger mixture at the beginning of a fill is with the photon trigger (~ 500 Hz), muon trigger (~ 500 Hz), local polarimeter trigger (~ 1.5 kHz), the BBC trigger (~ 1.5 kHz) and others such as clock trigger. The photon trigger and muon trigger are without prescale, while prescale for other triggers were adjusted so that the total rate does not exceed the DAQ limit of 5 kHz. The typical live time is more than 90% as displayed in Fig. 4.2.

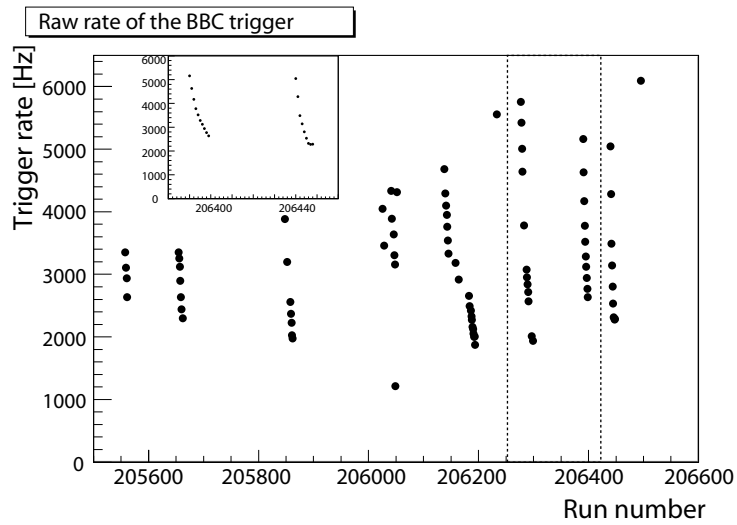


Figure 4.1: The raw rate of the BBC trigger vs run number.

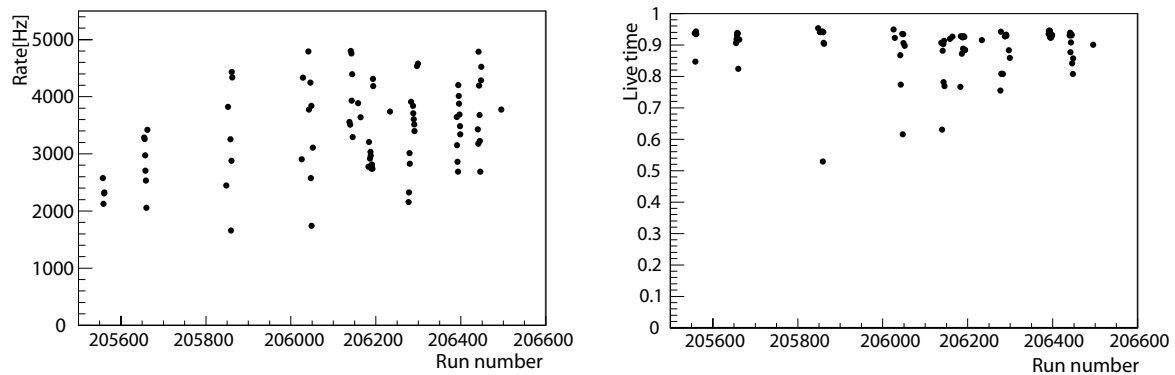


Figure 4.2: The rate of events recorded by Figure 4.3: The live time of DAQ vs run number.

4.3 Beam polarization

The beam polarization was measured with two types of polarimeters as described in Sec. 3.2.3. The pC polarimeter is utilized to measure fill by fill variations of the beam polarization, through A_N of proton-carbon elastic scatterings. Since no significant depolarization was observed during a fill, several pC polarimeter measurements in a fill are averaged and used for the asymmetry calculations. The absolute beam polarization is given by the H-jet polarimeter.

Figure 4.4 displays the beam polarizations, obtained with pC polarimeter and normalized by H-jet polarimeter results. Therefore, the vertical axis shows the absolute polarization. Statistical uncertainties and fill-to-fill uncorrelated uncertainties are shown.

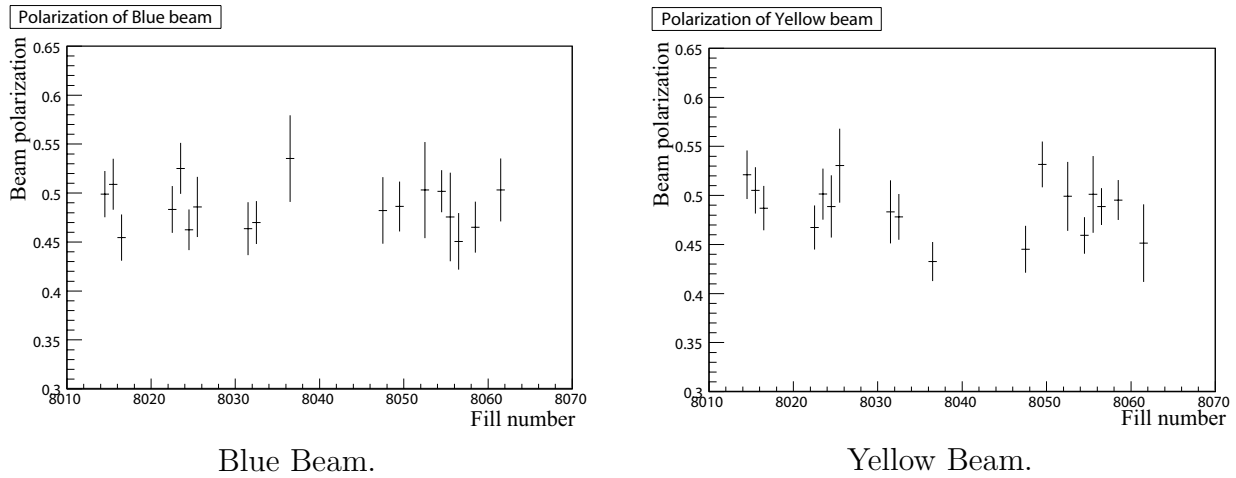


Figure 4.4: Beam Polarization.(Left: Blue Beam. Right: Yellow Beam.) The horizontal axis shows RHIC fill number, and the vertical axis shows the beam polarization. Statistical uncertainty and fill-to-fill uncorrelated systematic uncertainties are combined. Fill-to-fill correlated systematic uncertainty is not shown.

The luminosity-weighted average of beam polarization over 11 longitudinally (7 transversely) polarized fills used in this analysis, was

$$\langle P_B \rangle = 0.48 \pm 0.007[\text{stat}] \pm 0.035[\text{syst}], \quad (4.2)$$

$$\langle P_Y \rangle = 0.48 \pm 0.006[\text{stat}] \pm 0.045[\text{syst}], \quad (4.3)$$

for the longitudinal run period and

$$\langle P_B \rangle = 0.49 \pm 0.008[\text{stat}] \pm 0.035[\text{syst}], \quad (4.4)$$

$$\langle P_Y \rangle = 0.49 \pm 0.008[\text{stat}] \pm 0.045[\text{syst}], \quad (4.5)$$

for the transverse run period with a systematic uncertainty of 7.2% for the Blue beam, and 9.3% for the Yellow beam. The major systematic uncertainty is the statistical uncertainty

of H-jet polarimeter measurements which are used to normalize fill-by-fill pC polarimeter measurements. H-jet measurement for the Yellow beam at $\sqrt{s} = 62.4$ GeV was not reliable due to high background. Therefore, the calibration parameter for the yellow beam at $\sqrt{s} = 62.4$ GeV, $A_N(\text{yellow}, 62)$, was obtained as

$$A_N(\text{yellow}, 62) = A_N(\text{yellow}, 200) \times \frac{A_N(\text{blue}, 62)}{A_N(\text{blue}, 200)} \quad (4.6)$$

Additional systematic uncertainties were assigned for the Yellow beam according to the observed variations and dead layer drift at $\sqrt{s} = 200$ GeV. The average of the polarization product over the whole run was

$$\langle P_B \cdot P_Y \rangle = 0.23 \quad (0.24) \quad (4.7)$$

with a systematic uncertainty of 13.9%.

The remaining transverse-spin component (P_T/P) were measured with the PHENIX local polarimeter, by utilizing the single spin asymmetry A_N of forward neutron production. It measures the polarization in horizontal (x) and vertical direction (y) in the beam view. Then the transverse polarization component is calculated as:

$$\langle P_T/P \rangle = \sqrt{\langle P_x/P \rangle^2 + \langle P_y/P \rangle^2}, \quad (4.8)$$

and the longitudinal polarization is calculated as

$$\langle P_L/P \rangle = \sqrt{1 - \langle P_T/P \rangle^2}. \quad (4.9)$$

The results are summarized in Table 4.1. The transverse components of the beam polarizations are consistent with zero, thus the proton beams were purely longitudinally polarized within the uncertainties.

	$\langle P_x/P \rangle$	$\langle P_y/P \rangle$	$\langle P_T/P \rangle$	$\langle P_L/P \rangle$
Blue	-0.071 ± 0.135	0.080 ± 0.162	0.107 ± 0.151	$1.00 - 0.034$
Yellow	-0.039 ± 0.116	0.105 ± 0.119	0.112 ± 0.117	$1.00 - 0.025$

Table 4.1: Remaining transverse component and the longitudinal component of the beam polarizations.

4.4 Relative Luminosity

A relative luminosity R is the luminosity ratio between the same and opposite helicity collisions. It is required for the asymmetry calculations as in Eq. 4.1. In this section, relative luminosity measurement and a method to estimate its uncertainty are described.

4.4.1 Overview

The relative luminosity is defined as $R = \frac{L_{+-}}{L_{++}}$, where L_{++} and L_{+-} are the luminosity for the same and opposite helicity collisions, respectively. Although any counts which is proportional to luminosity can be used for the measurement of R , it is preferable for the counts to satisfy the following conditions: high statistics for high accuracy, no spin-dependence not to bias asymmetry measurement, small background, and linearity.

In this analysis, BBC trigger live counts were used for the relative luminosity measurement, since it satisfies all those requirements. Unfortunately BBC trigger rate (~ 10 kHz) was more than the DAQ data recording ability of 5 kHz and cannot be recorded without prescale. Thus GL1P scaler was utilized which keeps track of the number of live trigger counts for each bunch. It makes the statistical accuracy free from the DAQ data recording ability. The uncertainty on A_{LL} due to the uncertainty of R , δA_{LL}^{RL} , can be calculated as

$$\delta A_{LL}^{RL} = \frac{2N_{++}N_{+-}}{P_B P_Y (N_{++} + N_{+-} R)^2} \left(\frac{\Delta R}{R} \right) \sim \frac{1}{2P_B P_Y} \left(\frac{\Delta R}{R} \right), \quad (4.10)$$

where $N_{++(+--)}$ denotes the π^0 yields in the same (opposite) helicity collisions. P_B and P_Y are the beam polarizations.

To evaluate ΔR , BBC trigger counts (used for relative luminosity in this analysis) were compared to counts of triggers other than BBC trigger itself. The ZDCwide trigger was chosen for the transverse run period and the pZDC trigger was chosen for the longitudinal run period. The ZDCwide trigger is based on ZDCs which is another independent luminosity measure and can be used for comparison. However, the ZDCwide trigger rate was as low as the BBC trigger $\times \sim 0.008$ at $\sqrt{s} = 62.4$ GeV. Thus the accuracy was statistically limited and not satisfactory. To achieve better accuracy, the pZDC trigger was introduced and available for longitudinal run period. The pZDC is defined with BBCs and ZDCs as in Sec. 3.6 and also serves as a luminosity measure. Therefore, pZDC can be used for comparison. (Since the BBC trigger and the pZDC trigger uses BBCs in common, their dependence is considered in Sec. 4.4.6.)

The difference between the BBC trigger and the ZDCwide trigger (the pZDC trigger for longitudinal run period) is partially due to the difference of the vertex position cut as explained later in this section. Thus direct comparison of these will overestimate the relative luminosity uncertainties. Such an effect is corrected by utilizing the vertex distribution width.

At first, the quality of the bunches are investigated and only selected bunches were analyzed further. The selection criteria is described in Sec. 4.4.2.

4.4.2 Bunch selection criteria

The bunch crossing IDs are zero-based integer, 0 to 119. Although RHIC has 120 bunches in each RHIC beam, the last nine bunches in each beam were not filled as explained in

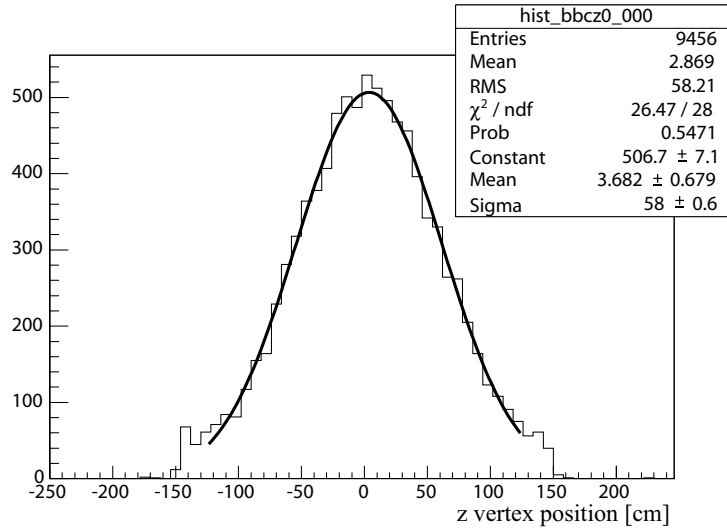


Figure 4.5: BBC z distribution. (Fill 8031, crossing number 0) It was fitted with Gaussian to obtain the vertex width. The BBCs are located at $|z| \sim 144$ cm and any collisions outside the range are reconstructed as $|z| \sim 144$ cm.

Sec. 3.2. The first bunch in the Blue beam collides on the 81st bunch in the Yellow beam at the PHENIX IR, which results in 18 (9×2) non-colliding bunch crossings. Two sets of non-colliding bunch crossings are called the “abort gaps”. The crossing ID = 1 was discarded due to the specification of DAQ. A bunch in each ring (ID = 20, 60) is reserved for accelerator control, and removed from the analysis. Consequently ninety nine bunch crossings survive the criteria. In addition, bunches with the BBC trigger counts 3 RMS less than the average were also removed since bunch crossings with small populations imply that they have different vertex distributions from others.

4.4.3 Vertex width

It was obtained by fitting the BBC z -vertex distributions to Gaussian in BBCLL1-(noVertexCut) triggered events fill by fill. Figure 4.5 shows an example of the fit in a fill. The bunch-by-bunch vertex distributions are well reproduced by Gaussians. The distributions have peaks at $|z| \sim 144$ cm since they are the places where BBCs are located and any collisions outside two BBCs are reconstructed at $|z| \sim 144$ cm. See Sec. 3.4.1 for detail.

4.4.4 A method to estimate the uncertainty on the relative luminosity

Here we introduce a ratio r_i defined as:

$$r_i = \frac{A_i}{B_i}, \quad (4.11)$$

where i is the crossing ID, and $A_i(B_i)$ is the number of counts of trigger A(B) in the crossing ID i ($i = 0 - 119$). If the triggers A and B are perfect luminosity measures, then r_i should be constant. The ratio r_i is calculated for each fill, and is fitted to

$$r_i = C[1 + A_{LL}P_BP_Y] \quad (4.12)$$

$$= C[1 + \varepsilon_{LL} \cdot \text{sgn}(P_BP_Y)] \quad (4.13)$$

where C and ε_{LL} are the fitting parameters. (when it is done for transverse runs, LL is replaced by TT .) A possible dependence of the triggers on spin is taken into account by introducing the parameter ε_{LL} in the fit. ε_{LL} is interpreted as the (raw) double helicity asymmetry of A compared to B . It is difference of the double spin asymmetries of A and B ,

$$\varepsilon_{LL} \sim \varepsilon_{LL}^A - \varepsilon_{LL}^B \quad (4.14)$$

when $\varepsilon_{LL}^A, \varepsilon_{LL}^B \ll 1$. And the raw asymmetries are related to the double helicity asymmetries as $A_{LL} = \varepsilon_{LL}/(P_BP_Y)$. This method provides the difference of the asymmetries for two processes. The BBC trigger, which is used for relative luminosity calculations, and the ZDCwide and pZDC are expected to be spin independent. It is confirmed by the comparison between BBC and ZDCwide (or pZDC).

The uncertainty propagates to A_{LL} of π^0 as $\frac{1}{P_Y P_B} \delta \varepsilon_{LL}$, where $\delta \varepsilon_{LL}$ denotes the uncertainty on the fit parameter ε_{LL} . The spin dependence ε_{LL} is expected to be zero and was confirmed in the analysis. The BBC trigger was chosen as trigger B throughout the analysis since it is the trigger used for relative luminosity calculations. Its spin dependence was evaluated by comparing it to ZDCwide or pZDC. ZDCwide was used as the trigger A for the transverse run period, and the pZDC trigger was used as the trigger A for the longitudinal run period as explained in Sec. 4.4.1. Figure 4.7 shows the results of the ratio r for a fill. (It is a fill from longitudinal run period. Thus pZDC trigger was used as the trigger A.) The solid line describes the fit function (Eq. 4.13). It was bent at removed bunches for a guide. It has a huge reduced χ^2 of 4248/95. r_i are different for different bunches but it cannot be explained by the spin dependence ε_{LL} . It is considered to be due to vertex width variations.

The BBC trigger has a vertex position cut of $z = \pm 35$ cm, while pZDC does not. Thus even if both work as perfect luminosity measures, wider vertex distribution makes the ratio r_i larger. Figure 4.6 illustrates the effect of the vertex cut on luminosity ratio. A Gaussian represents z vertex distribution in a bunch crossing. Two Gaussians in the

figure are with the same mean value of 0 but have different widths of $\sigma = 60$ cm and $\sigma = 40$ cm, and normalized so that to have the integrals over the whole z are the same. $\sigma = 60$ cm is reasonable for vertex distribution in real experiment but $\sigma = 40$ cm is extremely narrower than the real distributions but it was chosen so that to illustrate the effect clearly. The resolution of vertex cut is neglected in this discussion for simplicity. The dashed line represents the vertex cut implemented in the BBC trigger. Thus the BBC trigger counts collisions inside the vertex cut, while the pZDC trigger counts the whole z area. Let $N_{i,\text{BBC}}$ and $N_{i,\text{pZDC}}$ be the trigger counts of BBC and pZDC for the crossing i respectively, and $N_{i,\text{inside}}$, $N_{i,\text{whole}}$ be the counts for crossing i inside the vertex cut and the counts for the whole distributions respectively. Then the ratio $r_i = N_{i,\text{pZDC}}/N_{i,\text{BBC}}$ is proportional to $N_{i,\text{whole}}/N_{i,\text{inside}}$.

$$r_i = \frac{N_{i,\text{pZDC}}}{N_{i,\text{BBC}}} \propto \frac{N_{i,\text{whole}}}{N_{i,\text{inside}}}. \quad (4.15)$$

Thus the ratio between the two luminosity measures $N_{\text{pZDC}}/N_{\text{BBC}}$ is different due to the difference in width of the z vertex distributions. However, the difference due to the width has nothing to do with the accuracy of the relative luminosity. Let c be the vertex cut, and w be the vertex width. The fraction of events inside the vertex cut is calculated as

$$f_r(z') = \frac{2}{\sqrt{\pi}} \int_0^{z'} \exp(-t^2/2) dt. \quad (4.16)$$

where $z' = c/w$. Taylor expansion of $f_r(z')$ at $z'=0$ is

$$f_r(z') = z' + \frac{z'^3}{3} + \dots. \quad (4.17)$$

$f_r(z')$ can be approximated as $f_r(z') \sim z'$ when z' is smaller than one. Since $N_{i,\text{whole}}/N_{i,\text{inside}} \propto 1/f_r(z')$ and $z' \propto 1/w$, $N_{i,\text{whole}}/N_{i,\text{inside}}$ is linearly dependent on the vertex width w .

Figure 4.8 shows an example of the correlation between the ratio r_i and the vertex width. They have clear correlation as expected. The plots were fitted to a linear function:

$$f(w) = p_0 + p_1 w, \quad (4.18)$$

where w denotes vertex width, and p_0 and p_1 denote fit parameters. Figure 4.9 shows the deviation of r_i from the fit divided by its statistical error δr_i . The reduced χ^2 of the fit is greater than unity which indicates the existence of effects other than the vertex width dependence. Such unknown uncertainties are accounted by enlarging the uncertainty by $\sqrt{\chi^2/\text{NDF}}$. If the deviation from the fit is greater than $2.5 \times \sqrt{\chi^2/\text{NDF}}$, the bunch crossing was removed from the asymmetry calculations since it implies that it has different vertex distributions from other crossings. In Fig. 4.9, a bunch with a deviation of ~ 11 was removed (crossing ID = 75.) Figure 4.11 displays corrected ratio $r' = r/f(w)$ and the fit results. Please note that the reduced χ^2 of the fit was greatly reduced from 4248/95 (~ 45) to 802.2/94 (~ 8.5), but there still remain systematic uncertainty. It was accounted by enlarging the fit error with $\sqrt{\chi^2/\text{NDF}}$.

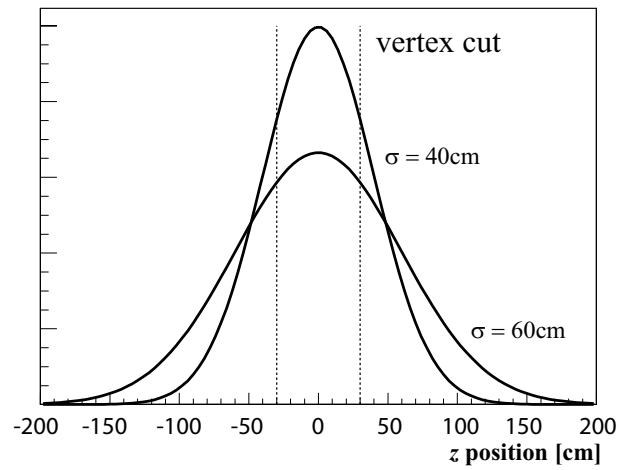
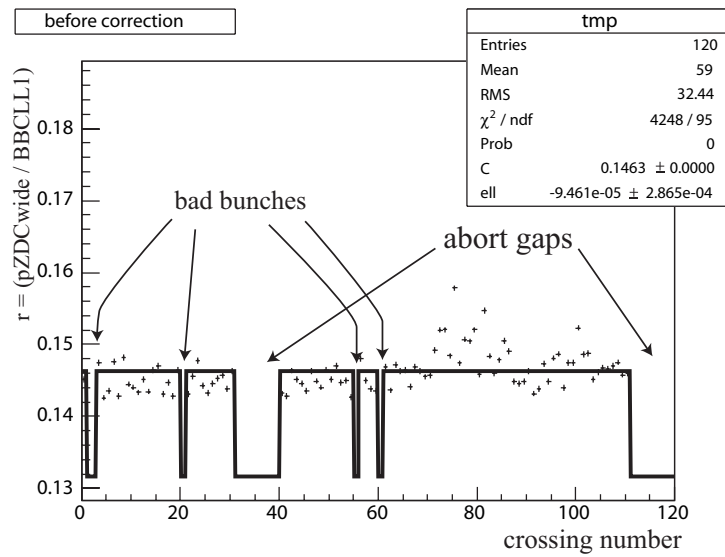


Figure 4.6: The effect of vertex cut on luminosity ratio.

Figure 4.7: ratio $r = \text{pZDC} / \text{BBCLL1}$ and the fit result.

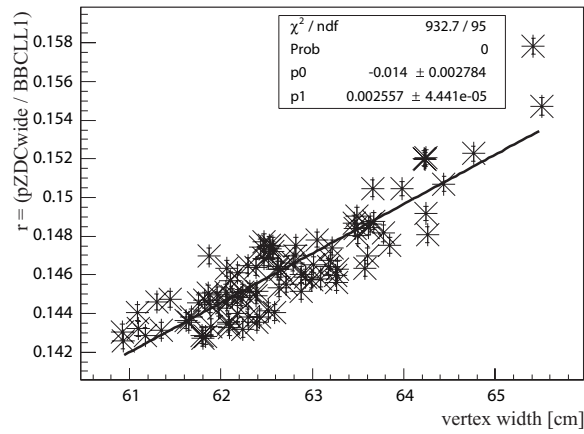
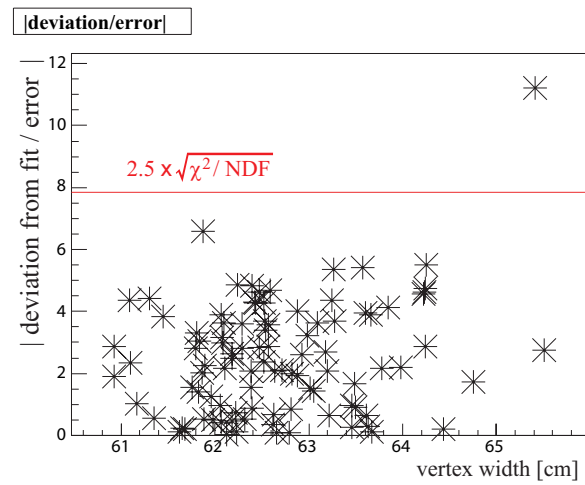
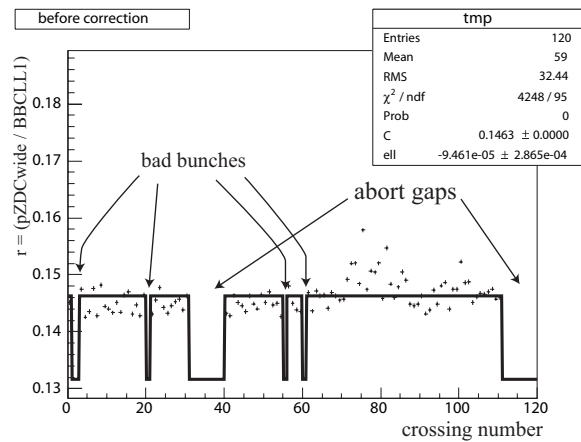
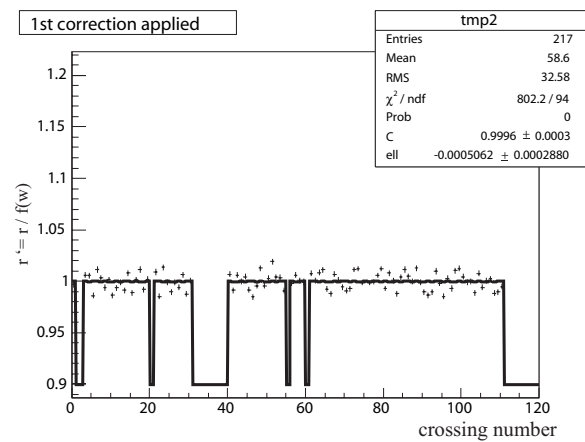
Figure 4.8: ratio r vs vertex width.

Figure 4.9: Deviations from the fit divided by statistical uncertainties.

Figure 4.10: r_i (before vertex width correction)Figure 4.11: r'_i (after vertex width correction)

4.4.5 Results of relative luminosity analysis

Figure 4.12 shows the reduced χ^2 vs $\delta\varepsilon_{TT}$ for the transverse run period, and Fig. 4.13 displays the reduced χ^2 vs $\delta\varepsilon_{LL}$ for the longitudinal run period. They look reasonable and no fills were removed. Figure 4.14 (4.15) displays $\varepsilon_{TT(LL)}$ vs fill number and was fitted to constant. For conservative estimation of uncertainty, the fill-by-fill statistical uncertainty for $\varepsilon_{\text{fill}}$, $\delta\varepsilon_{\text{fill}}$, is enlarged by $\sqrt{\chi^2/\text{NDF}}$ when $\chi^2/\text{NDF} > 1$ as mentioned in the previous subsection, to account possible systematic uncertainty as mentioned in the previous subsection. The enlarged error is indicated by red error bar in Fig. 4.14 and Fig. 4.15. The uncertainty $\delta\varepsilon_{TT}$ (transverse) was found to be 7.5×10^{-4} , and $\delta\varepsilon_{LL}$ (longitudinal) was found to be 3.3×10^{-4} . Since the average polarization is $\langle P_B \cdot P_Y \rangle = 0.24$ (2.3) for transverse (longitudinal), the effect on double spin asymmetries will be $\delta A_{TT} = 3.1 \times 10^{-3}$ for transverse run period, and $\delta A_{LL} = 1.4 \times 10^{-3}$ for longitudinal run period. The statistical accuracy of $A_{TT}^{\pi^0}$ and $A_{LL}^{\pi^0}$ for π^0 are $\delta A_{TT}^{\pi^0} \sim 7 \times 10^{-3}$ and $\delta A_{LL}^{\pi^0} \sim 5 \times 10^{-3}$ respectively. Therefore, the systematic uncertainties from relative luminosity are small compared to the statistical uncertainties of π^0 asymmetries.

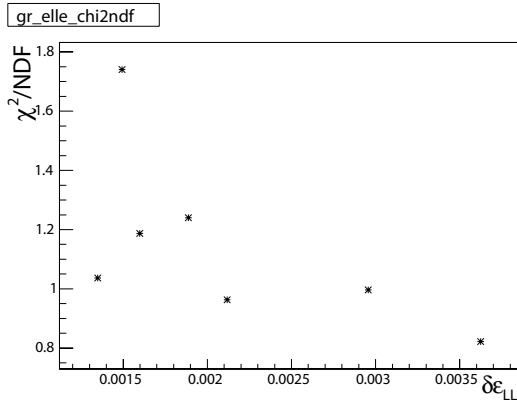


Figure 4.12: χ^2/NDF VS ε_{TT} (Transverse run period. ZDCwide)

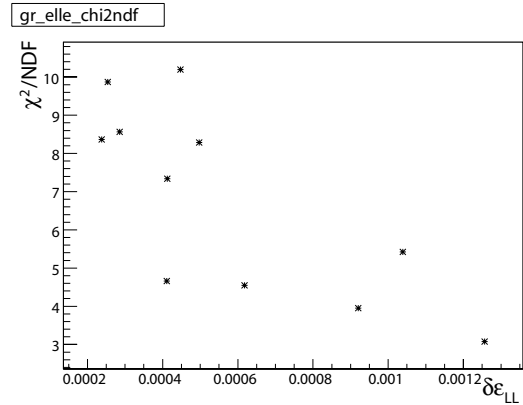
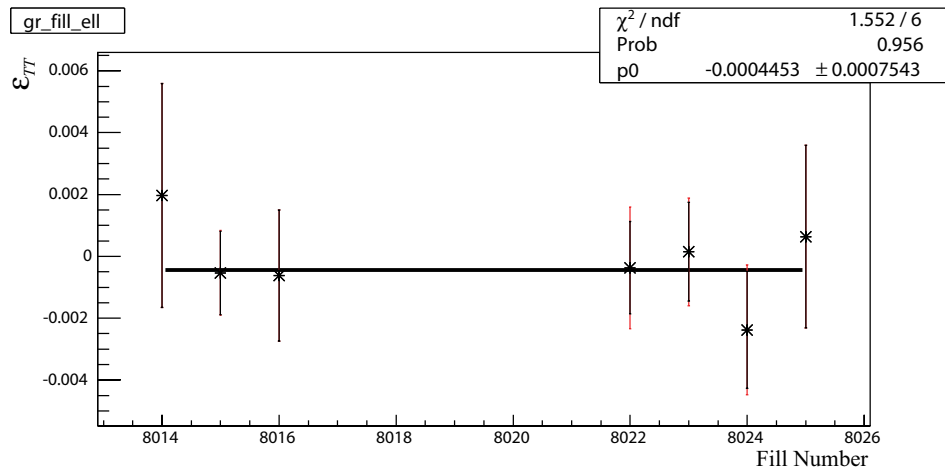
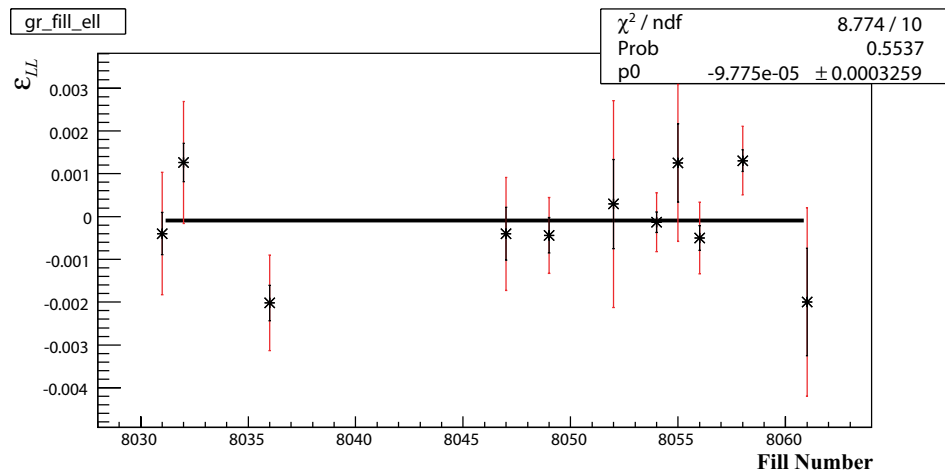


Figure 4.13: χ^2/NDF VS ε_{LL} (Longitudinal run period. pZDC)

4.4.6 Event overlap

The BBC and pZDC triggers use the BBCs in common. To evaluate how much the pZDC trigger is dependent on the BBC trigger in statistical point of view, event overlap was investigated using real data. We define a notation “A in B” which describes the number of live counts of trigger-A in trigger-B triggered events. For example, “ZDCwide in BBC no-vertex-cut” means ZDCwide live counts in the BBC no-vertex-cut triggered events. The results are shown in Table 4.2. For comparison, event overlap at $\sqrt{s} = 200$ GeV was also investigated. (We used to use ZDCwide in the analysis at $\sqrt{s} = 200$ GeV.) ZDCwide in

Figure 4.14: ϵ_{TT} vs fill.Figure 4.15: ϵ_{LL} vs fill.

BBC no-vertex-cut at $\sqrt{s} = 200$ GeV and pZDC in BBC-no-vertex-cut at $\sqrt{s} = 62.4$ GeV are 0.7%, 1.2% respectively. BBCno-vertex-cut in ZDCwide at $\sqrt{s} = 200$ GeV and BBC-no-vertex-cut in pZDC at $\sqrt{s} = 62.4$ GeV is 21% and 19%, respectively. The event overlap is in similar level at both energies. The BBC trigger and the pZDC (and ZDC) trigger are almost independent in statistical point of view and can be used to obtain the accuracy of relative luminosity.

Trigger		62.4GeV	200GeV
BBC no-vertex-cut	in ZDCwide	1.3×10^{-2}	2.1×10^{-1}
ZDCwide	in BBC no-vertex-cut	3.8×10^{-5}	6.7×10^{-3}
BBC no-vertex-cut	in pZDC	1.9×10^{-1}	N/A
pZDC	in BBC no-vertex-cut	1.2×10^{-2}	N/A

Table 4.2: Event Overlap. The results from $\sqrt{s} = 62.4$ GeV in Run 2006 and $\sqrt{s} = 200$ GeV in Run 2005 are shown.

4.4.7 Single beam background

Single beam background is estimated by comparing the BBC trigger counts in colliding and non-colliding bunch crossings. There are two types of non-colliding bunch crossings: Blue beam only bunch crossings (31 – 39), and Yellow beam only bunch crossings (111 – 119). Among the Yellow beam only crossings, crossing ID = 115 was removed since it is reserved for GL1P scaler reset and the trigger counts in the bunch crossing is not correct. Figure 4.16 shows the ratio between the average counts in colliding and non-colliding bunch crossings versus run sequence number. Open (closed) circle is from Blue (Yellow) beam only bunch crossings. Single beam background is $< 0.35\%$ and it has negligible effect on δA_{LL} .

4.5 π^0 reconstruction

Spin dependent (bunch crossing dependent) π^0 yields are necessary for asymmetry calculations. π^0 is detected via two photon decay, $\pi^0 \rightarrow \gamma\gamma$. The decay photons are detected with PHENIX EMCAL, which is explained in Sec. 3.5.1. The high p_T photon trigger was utilized to collect data. The trigger performance including its rejection power and efficiency for π^0 , is discussed in Sec. 4.5.1.

Deposited energy of photon-induced electromagnetic showers in EMCAL spreads among several towers, which is the minimum unit of individual read-out in EMCAL. These towers with deposited energy are gathered to form a cluster to measure the photon energy. The clustering algorithm used in the analysis is explained in Sec.4.5.2.

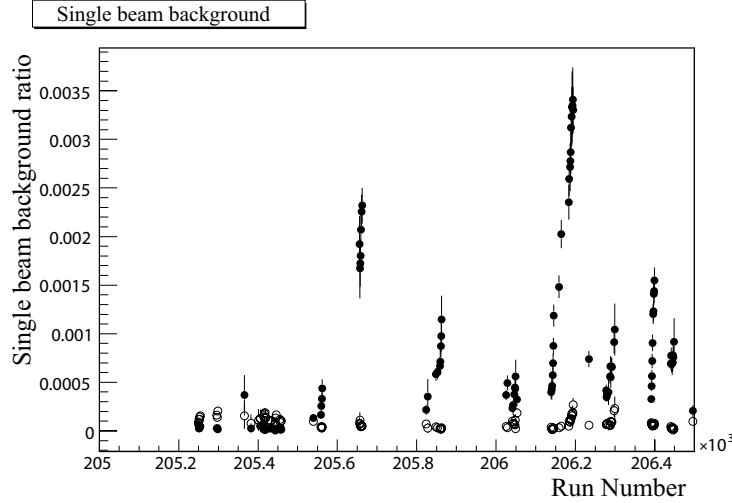


Figure 4.16: The ratio between the average BBC trigger counts in colliding and non-colliding bunch crossings. Open circle: Blue beam only bunch crossings. Closed circle: Yellow beam only bunch crossings.

EMCal is composed of many towers and some towers may not work properly. The quality assurance of the EMCal towers is explained in Sec. 4.5.3. tower-by-tower relative gain variations were corrected online as explained in Sec. 3.5.1. In addition, offline energy calibration was performed with the measured π^0 peak position as described in Sec. 4.5.4. The applied cuts to identify π^0 are explained, and obtained two-photon invariant mass spectra are shown in Sec. 4.5.6. The EMCal stability for the whole run is evaluated in Sec. 4.5.7. The background in the obtained two-photon invariant mass spectra are discussed in Sec. 4.5.8 and Sec. 4.5.9.

4.5.1 High- p_T photon trigger performance

The analysis is based on data collected with the high p_T -photon trigger. We review the trigger performance in this section. The trigger decision is based on the energy sum of 2×2 towers. A collection of 2×2 towers are referred to as a trigger tile. See Sec. 3.5.2 about the trigger.

Rejection power

The performance of the trigger is monitored by the rejection power which is defined as $N_{\text{BBC}}/N_{\text{photontrig}}$ where N_{BBC} is the number of the BBC triggered events, and $N_{\text{photontrig}}$ is the number of the high- p_T photon triggered events respectively. The rejection factor is defined using the BBC trigger since the BBC trigger is the best luminosity measure

in PHENIX as described in Sec. 4.4. The BBC trigger detects 40% of the inelastic pp scatterings at $\sqrt{s} = 62.4$ GeV. Figure 4.17 shows the obtained rejection power of the high- p_T photon trigger. The rejection power was about ~ 10 during the run. A cluster of runs corresponds to a fill. (Between fills, about ~ 100 of run numbers were consumed for detector calibrations and diagnostics of DAQ.) The time dependence of rejection power is mainly caused by electronics noise. Sometime we have very hot towers which fire the trigger at every crossing. Such towers are masked for trigger decision and such runs with hot trigger tiles were discarded.

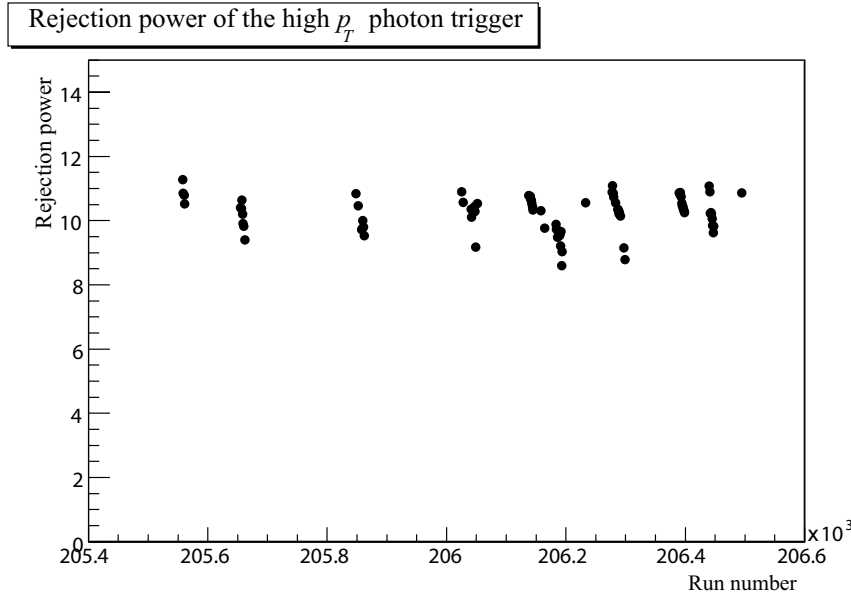


Figure 4.17: Rejection power of the high- p_T photon trigger

Circuit swap of the high- p_T photon trigger

As described in Sec. 3.5.2, the high- p_T photon trigger utilizes two different circuits for a trigger tile and alternated in each beam clock count. Therefore, signals from even and odd bunch crossings are treated with two different circuits. Different circuits lead to different thresholds, and false asymmetries. It is avoided by calculating asymmetries separately for even and odd bunch crossings.

The synchronization of the circuit usage for even and odd bunch crossings is done at the beginning of a run. Therefore, a swap of the circuits between even and odd bunch crossing may take place between two consecutive runs in a fill. Figure 4.18 shows an example of such swap. The ratio $N_{\text{photontrig}}/N_{\text{BBC}}$, which is the inverse of the rejection power, is plotted for each bunch crossings for a sector. The inverse of the rejection power

is different from that in Fig. 4.17 by a factor of 8 which is the number of sectors. The ratio is different for even and odd bunch crossings due to the slightly different threshold of the circuits. It swaps between even and odd bunch crossings between consecutive runs within the same fill. The probability to have such swap was small, about once in five runs. Please note that the synchronization of trigger circuits are done at the beginning of data taking thus trigger circuit swap never occur during a run.

Therefore, asymmetry calculations were performed run-by-run basis. Unfortunately there is not enough statistics to calculate background asymmetry for the highest p_T bin ($3 - 4 \text{ GeV}/c$) in run-by-run basis. Thus fill-by-fill calculations were performed for the highest p_T only. As explained later in this section, the trigger efficiency reaches plateau at $p_T > 3 \text{ GeV}/c$. Therefore, it is safe to calculate fill-by-fill at the highest p_T bin.

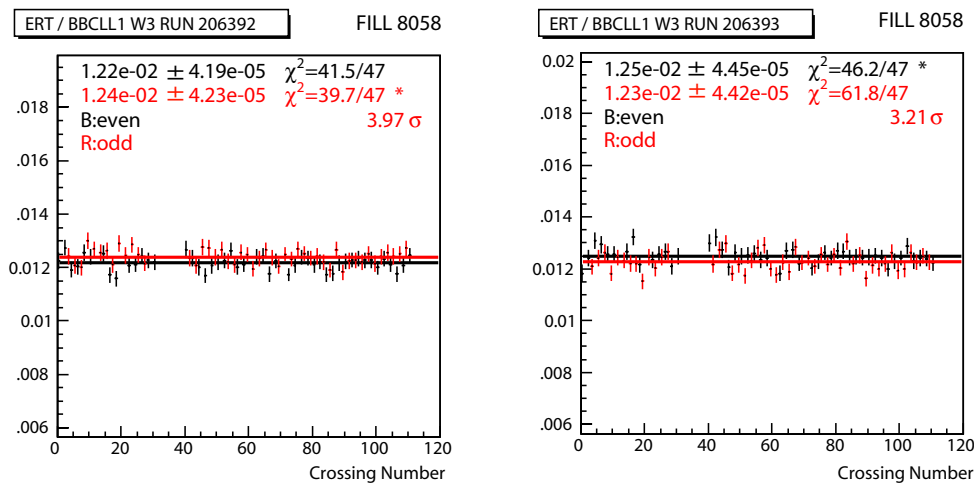


Figure 4.18: An evidence of trigger circuit swap between even and odd bunch crossings between runs in a same fill. The ratio between the high- p_T photon triggered events and the BBC triggered events versus crossing number for a sector. Black histograms are for the even crossings and red histograms are for the odd crossings. They are fitted to constants for even and odd bunches separately and the fit results with reduced χ^2 are shown in the histograms. The larger fit results are indicated with * and are swapped between Run 206392 (Left) and Run 206393 (Right). These two runs are in the same fill.

The high- p_T photon trigger efficiency for π^0

The high- p_T trigger efficiency is defined as the fraction of clusters which fire the high- p_T photon trigger in BBC triggered events. Figure 4.19 displays the high- p_T photon trigger efficiency for π^0 's vs p_T . They are $\sim 55\%$ ($\sim 25\%$) at $p_T=1 \text{ GeV}/c$, increase towards higher p_T , and reach plateau of $\sim 98\%$ ($\sim 88\%$) for PbSc (PbGl). Noisy towers in EMCAL,

mainly due to electronics noise, are removed from trigger decision. The plateau can be explained by the fraction of the removed towers in the trigger decision.

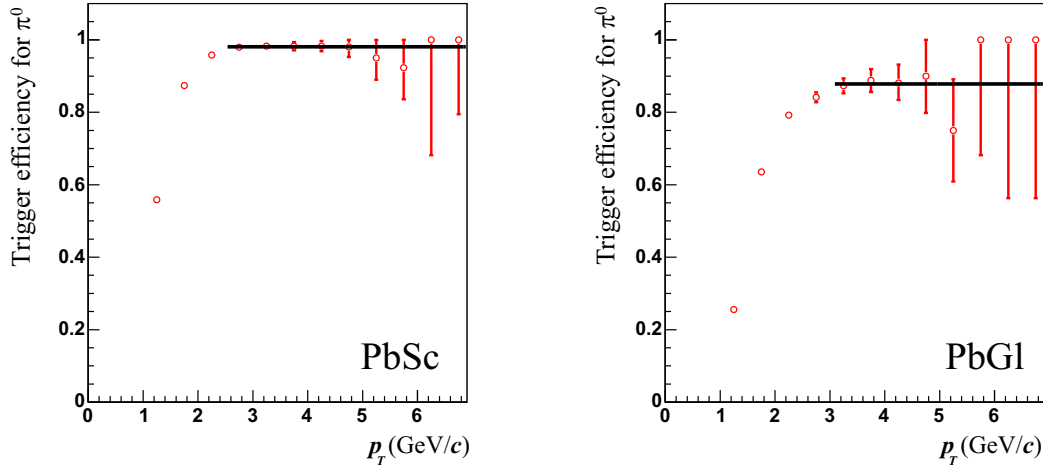


Figure 4.19: The high- p_T photon trigger efficiency for π^0 versus p_T . Left: PbSc. Right: PbGl. Both PbSc and PbGl reach plateau at high p_T and it is explained by the fraction of masked trigger tile.

4.5.2 Clustering algorithm

From EMCal, the following information about an incident particle is extracted for the analysis.

- Total energy
- Hit position
- Photon probability

The energy deposit of a particle hit at EMCal spreads among several towers. To extract information of the incident particle, it is necessary to find a group of towers which have energy deposit of the particle.

At first, a certain threshold is applied to select towers. The threshold is 10 MeV for PbSc and 14 MeV for PbGl. The higher threshold for PbGl is due to the larger noise in PbGl. The neighboring towers among the selected towers are grouped into clusters. If there are more than two maxima of energy deposit in a cluster, they are splitted into clusters so that a cluster has only one maximum.

In PbGl, all energies in the cluster towers are summed and total energy is corrected for the incident angle dependence. In PbSc, “core” tower technique is utilized to extract energy deposit of clusters. The sum is performed only for core towers, instead of summing all tower energy in a cluster. Core towers are defined as those in which the incident particle is estimated to deposit the energy more than 2% of the total energy. The estimation is based on the electromagnetic shower profile which was parametrized in the test beam experiments. The energy sum of core tower is about 90% of the total. Then the total energy is extracted with the impact angle dependence correction. The impact angle dependence is less than 4%. The energy losses caused by the attenuation in the fibers and shower leakage, are corrected. The “core” tower technique was introduced to cope with the high occupancy environment in heavy ion collision experiment. Although it is not necessary in pp collisions, it is favorable to use the same algorithm in both pp and heavy ion experiment to reduce unnecessary systematic uncertainty due to the difference of clustering algorithms. This degrades the energy resolution slightly (the constant term of the energy resolution is increased from 2% to 3%) but the achieved resolution is good enough for the analysis.

The hit position of the incident particle is obtained by the center of gravity method. The positions of towers in a cluster are weight-averaged by tower energy. Then the dependence of the impact angle of the particle is corrected.

Photon probability is calculated based on χ^2 test of the observed energy distribution in a cluster with an ideal electromagnetic shower profile which is parametrized by the test experiment.

4.5.3 Quality assurance of the EMCal towers

EMCal consists of ~ 25000 towers and some of the towers may not work as expected. Towers which do not work as expected, are masked and not used for the analysis. Such towers can be categorized into three types: dead, noisy and not-calibrated towers. A dead tower is defined as the number of hits in the tower is zero or considerably smaller than other towers. A noisy tower is defined as a tower sending signals greatly higher frequency than other towers, which is due to electronics noise. Distributions of the number of hits for each tower, is created for each sector and towers which have multiplicity greater by 15σ from the average are labeled as noisy and removed. Since energy leakage may affect the energy measurement, in addition to those towers described above, towers next to those bad towers, and the edge towers are also removed. Table 4.5.3 summarizes the fraction of the masked towers.

4.5.4 Energy calibration of EMCal

The time dependence of the gain in EMCal is corrected tower-by-tower basis with the laser calibration system in EMCal. The calibration data are analyzed automatically after

	PbSc		PbGl	
Edge towers	1272	(8.2%)	568	(6.2%)
Bad towers	288	(1.9%)	420	(4.6%)
Neighbor towers	2060	(13.2%)	2110	(22.9%)
Total towers	15552		9216	

Table 4.3: The fraction of the masked towers.

calibration data taking, and stored into the PHENIX calibration database. In addition to the online calibration, offline energy calibration was performed by utilizing the measured π^0 peak position. The offline energy calibration utilizes physics signal and provide most reliable energy scale. The energy scale is corrected for π^0 peak to have the world average of π^0 mass obtained by Particle Data Group (PDG) [76] at first. After the calibration, the scale is further corrected for energy smearing effect as explained in Sec. 4.5.5.

The amount of the collected data at $\sqrt{s} = 62.4$ GeV was not enough for the offline tower-by-tower energy calibration. However, before short low energy pp experiment at $\sqrt{s} = 62.4$ GeV (~ 2 weeks), longer high energy pp experiment at $\sqrt{s} = 200$ GeV (~ 10 weeks) was performed. Thus the calibrations were performed with the data at $\sqrt{s} = 200$ GeV instead.

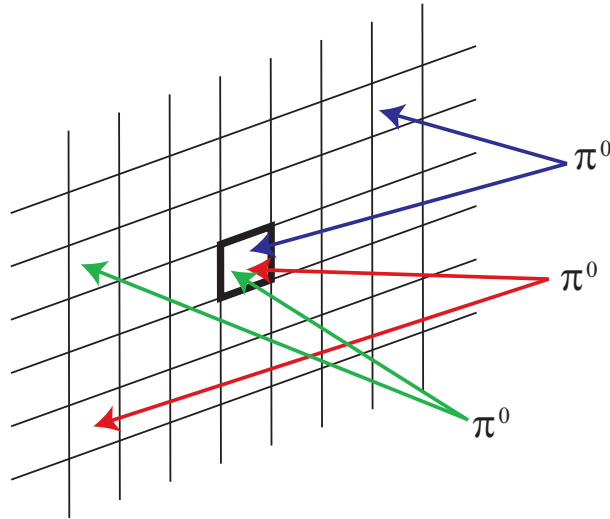


Figure 4.20: A method of tower-by-tower energy calibrations. The boxes represent EMCal towers. The box surrounded by thick lines is the target tower of the calibration. One of the decay photon of each π^0 in the figure hits the target tower. These π^0 's are used for the calibration of the target tower.

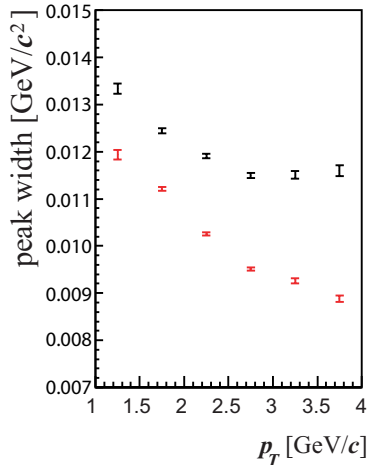


Figure 4.21: π^0 width vs p_T before (Black) and after (Red) energy calibration.

The offline calibration procedure is as follows. At first, run-by-run variations are corrected using π^0 mass peak position. Then tower-by-tower gain correction follows. Figure 4.20 illustrates the method of the tower-by-tower calibration. The energy scale of a target tower is corrected with the measured π^0 -mass peak for photon pairs, one of each pair hits the target tower. Although the mass shift due to the other tower is averaged and have smaller effect than the target tower, it is still not negligible. It is overcome by iterating the process several times. Figure 4.21 displays the width of π^0 before and after the calibration.

At the time of clustering, non-linearity due to energy leakage and light attenuation in the fibers were corrected as in Sec. 4.5.2. However, there are residual non-linearity mainly due to a finite energy threshold for individual towers to cut electronic noise. Residual non-linearity was corrected by utilizing p_T -dependent π^0 -mass peak-position and was obtained to be

$$E_{\text{corrected}} = \frac{E_{\text{org}}}{0.003 + (1 - 0.01/E_{\text{org}})} \quad \text{for PbSc} \quad (4.19)$$

$$E_{\text{corrected}} = \frac{E_{\text{org}}}{0.021 + (1 - 0.02/E_{\text{org}})} \quad \text{for PbGl.} \quad (4.20)$$

The above corrections were obtained with the data at $\sqrt{s} = 200$ GeV, and applied for data at $\sqrt{s} = 62.4$ GeV.

4.5.5 Absolute energy scale

The absolute energy scale is calibrated by comparing the observed and the simulated π^0 mass. For the purpose, Fast Monte Carlo (FastMC) simulation was used. FastMC is a

simple Monte Carlo simulation unlike GEANT. It produces π^0 according to the measured cross section, makes it decay into two photons, and smears the energies and the positions of the photons according to the detector resolutions. Electro-magnetic shower profiles are simulated with the parameters obtained with the test experiments. The same tower masks as in the analysis was used and the trigger efficiency was applied.

Finite energy resolution cause π^0 mass peak shift from the PDG (world average) value due to the steep p_T dependence of π^0 cross section. A π^0 with a certain measured p_T may have lower or higher p_T in reality due to finite energy resolution. The invariant mass of two photon pair, $M_{\gamma\gamma}$ and transverse momentum, p_T are calculated as

$$\begin{aligned} M_{\gamma\gamma}^2 &= 2E_1E_2(1 - \cos(\theta)) \\ &= 4E_1E_2 \sin^2\left(\frac{\theta}{2}\right), \end{aligned} \quad (4.21)$$

and

$$p_T = \sqrt{|\mathbf{E}_{T,1} + \mathbf{E}_{T,2}|^2} \quad (4.22)$$

$$= \sqrt{|\mathbf{E}_{T,1}|^2 + |\mathbf{E}_{T,2}|^2 + 2|\mathbf{E}_{T,1}||\mathbf{E}_{T,2}|\cos\phi} \quad (4.23)$$

where E_1 and E_2 ($\mathbf{E}_{T,1}$ and $\mathbf{E}_{T,2}$) represent energy (transverse energy) of two photon clusters, θ is the opening angle between the clusters, ϕ is the angle between $\mathbf{E}_{T,1}$ and $\mathbf{E}_{T,2}$. When reconstructed p_T is higher than the real p_T , reconstructed mass is likely to be larger than the real π^0 mass at the same time and vice versa. Due to the steep p_T dependence, effect from lower p_T is more than higher p_T which results in π^0 mass shift to higher side. In addition, π^0 mass peak position becomes lower due to the following effects. One of the sources of the unusual π^0 is so called ‘‘albedo’’. One of decay photons may convert into electron-positron pair, but still be reconstructed as a single cluster when the pair is close enough. Therefore, the reconstructed mass is close to that of π^0 . Another source is π^0 from decay of other hadrons such as K_s^0 and η . The effects were evaluated with GEANT and obtained to be -1 ± 1 MeV/ c^2 . The uncertainty is translated into 0.7% in energy scale and is accounted as systematic uncertainty. In the FastMC, the π^0 mass was lowered by 1 MeV/ c^2 to take into account the effect. Finally, the mass was evaluated by the FastMC and found to be about 137 MeV and the energy scale at $\sqrt{s} = 62.4$ GeV was corrected accordingly.

To reproduce the measured π^0 peak width vs p_T , the constant term of EMCAL energy resolution was increased to 4% (6%) in PbSc and PbGl. It is mainly due to the imperfection of the calibration.

Figure 4.22 displays the positions and widths of the observed and simulated π^0 mass peak. Energy asymmetry, α , is defined as

$$\alpha = \frac{|E_1 - E_2|}{E_1 + E_2}, \quad (4.24)$$

where E_1 and E_2 are the photon energies of a pair. Figure 4.23 shows the energy asymmetry, α , distributions for $p_T = 1.0 - 1.5$ GeV/ c and $p_T = 2.5 - 3.0$ GeV/ c . The non-linearity corrections as described in Sec. 4.5.4 were already applied for the plots. A cut was applied for Energy asymmetry $\alpha < 0.8$ as described in the next subsection. The energy asymmetry, α , is not flat for low p_T due to the energy unbalance between two photons caused by the high- p_T photon trigger. FastMC simulation and data agree well.

Slight difference of the π^0 peak position between sectors of EMCAL is observed and is expected from misalignment of EMCAL. The uncertainty was evaluated to be 1%. For the final systematic uncertainty of the energy scale, 1% (misalignment) and 0.7% (mass shift) was added in quadrature and 1.2% was assigned. This has negligible effect on A_{LL} since observed A_{LL} is flat.

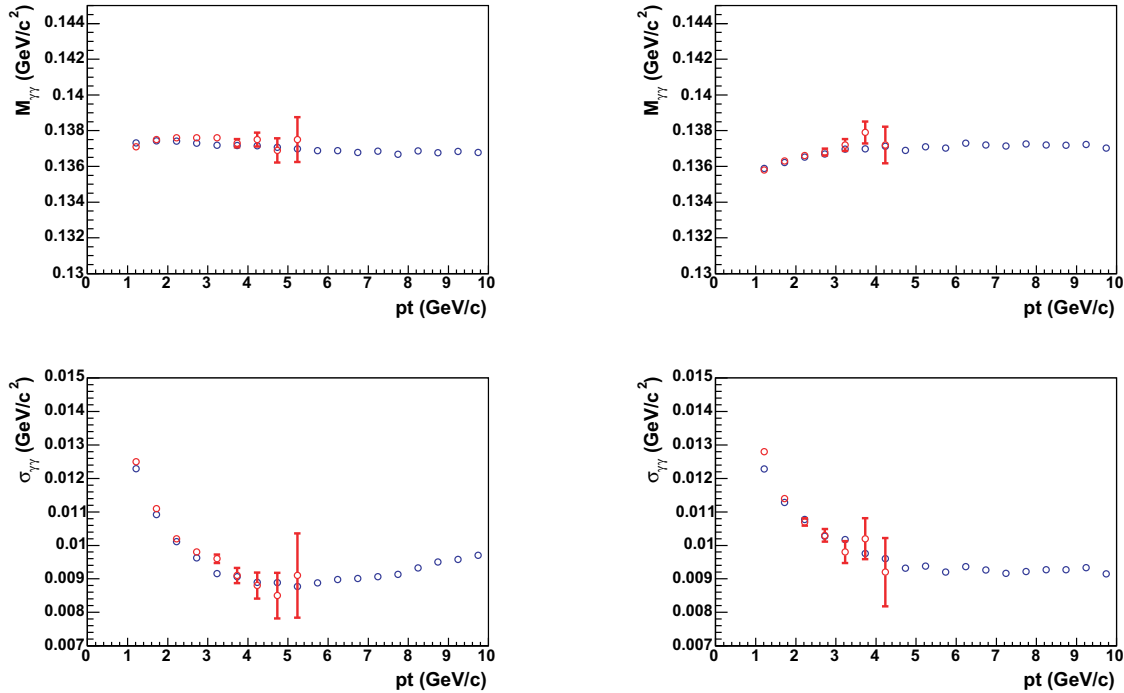


Figure 4.22: π^0 peak position vs p_T (Top) and π^0 peak width (Bottom) for PbSc (left) and PbGl (right). Blue points are obtained with simulations, Red points are from real data.

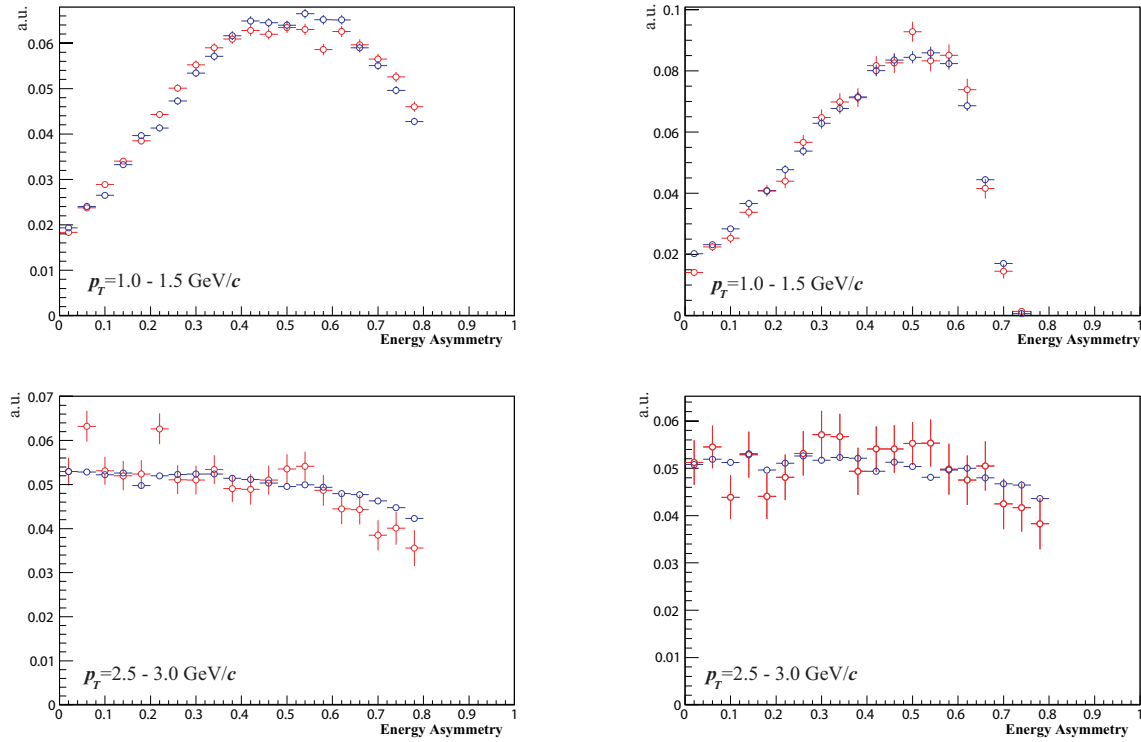


Figure 4.23: Energy asymmetry α for $p_T = 1.0 - 1.5$ GeV/c (Top) and $p_T = 2.5 - 3.0$ GeV/c. Left plots are for PbSc and right plots are for PbGl. Blue points are obtained with simulations, and red points are from real data. The decrease in high α for $p_T = 1.0 - 1.5$ GeV/c is due to the minimal energy cut for single photons.

4.5.6 Reconstruction of π^0

As explained in the beginning of this section, π^0 yields are required for the asymmetry calculations. The π^0 mesons are detected via two photon decay and the photons were detected with PHENIX EMCAL.

In this analysis, invariant mass spectrum was obtained for any pairs of clusters in EMCAL in an event. A peak at π^0 mass in the invariant mass spectrum was identified as π^0 . The following criteria were applied for clusters or cluster pairs to reduce the background.

- Minimal photon energy cut,
- Shower profile cut,
- Energy asymmetry cut (α),

- Trigger tile matching for the higher energy cluster.

Minimal photon energy cuts were applied to reduce combinatorial background from very low energy clusters. The threshold was 0.1 GeV (0.2 GeV) for PbSc (PbGl). Higher threshold for PbGl is due to the larger noise in PbGl. Energy distribution in a cluster is compared with shower profile which is parametrized in the test experiment. Based on the χ^2 test, clusters which has probability of less than 0.02 are discarded. Energy asymmetry is expected to be flat where trigger bias is small, while combinatorial background tends to have large energy asymmetry due to large number of low energy clusters. Energy asymmetry cut $|\alpha| < 0.8$ was applied to further reduce the background. The background ratios for various cut conditions are summarized in Table 4.4. The background ratios for the cuts applied for the analysis is in column (a).

Two-photon invariant mass spectrum for each p_T bins are shown in Fig.4.24. In addition to a peak corresponds to π^0 , there exists another peak near ~ 0 GeV/ c^2 . The peak originates from cosmic ray and hadrons and is discussed in detail in Sec. 4.5.8.

p_T (GeV/ c)	Background ratio		
	(a)	(b)	(c)
1.0 – 1.5	35%	37%	46%
1.5 – 2.0	17%	20%	31%
2.0 – 2.5	10%	13%	27%
2.5 – 3.0	5.5%	8.8%	36%
3.0 – 4.0	3.9%	8.7%	57%

Table 4.4: The background ratio for different cuts. (c) with minimal photon energy cut, and trigger tile matching. (b) with shower profile cut in addition to the cuts imposed on (c). (a) with energy asymmetry cut in addition to the cuts imposed on (b). (cuts used for the final results.)

4.5.7 EMCAL stability

EMCAL stability was investigated with run-by-run variation of π^0 identification. Figure 4.25a) displays run-by-run variations of π^0 peak position. A gain drift can be seen and the π^0 mass increased by ~ 2 MeV towards the end of the run. However, the peaks are within $\pm \sim 2$ MeV and we use ± 25 MeV mass window. Therefore no further run-by-run correction was applied. Figure 4.25b) and c) show the run-by run variations of the width and the background ratio of π^0 peak. They are stable for the runs and no runs were excluded by the EMCAL stability check.

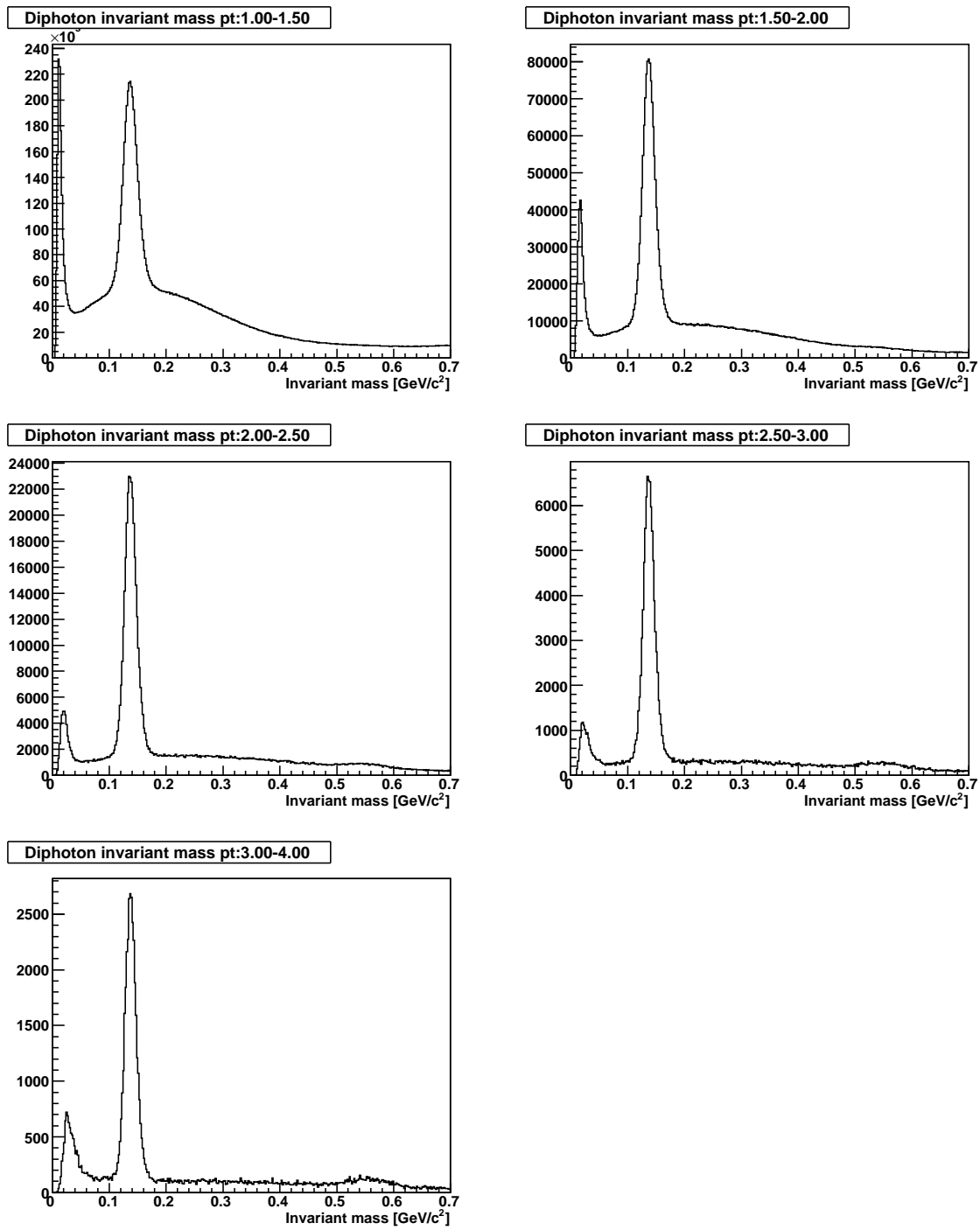


Figure 4.24: Two-photon invariant mass spectra. Both PbSc and PbGl types were used to obtain the distributions.

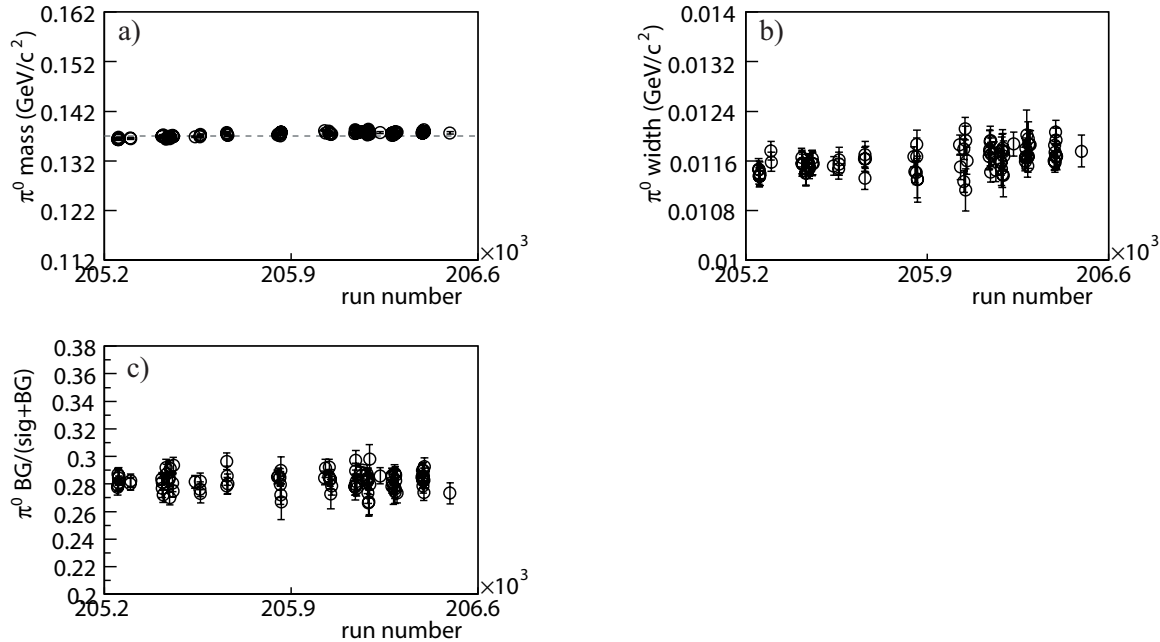
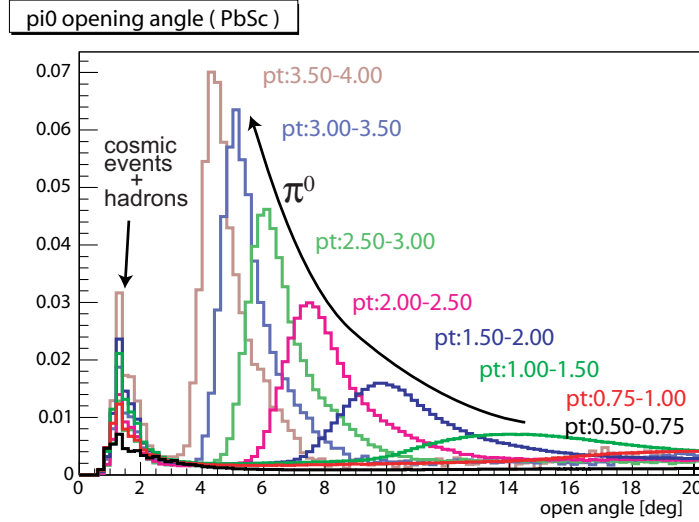


Figure 4.25: Run-by-run variation of π^0 identification. The horizontal axis is the run sequence number for the three plots. a) mass of π^0 . The range of the vertical axis corresponds to the mass window used to identify π^0 . b) width of π^0 . c) background ratio. They are stable for the whole run.

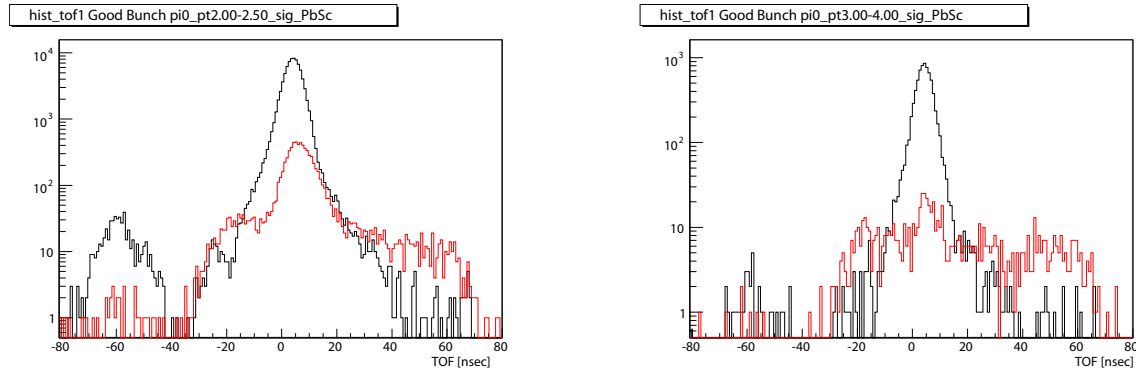
4.5.8 Discussion on the background peak

As shown in Fig. 4.24 there exists a peak below π^0 mass and they move towards π^0 peaks with increasing p_T . The peak comes from hadrons and cosmic rays. Hadrons and cosmic rays make wider shower than photons and sometimes make two maxima in a cluster. Such clusters are divided into two by the clustering algorithm, which makes a pair of clusters with the same distance (thus opening angle). Since the width of a tower corresponds to an angle of 0.011[rad], the angle between the splitted towers is expected to be $0.011[\text{rad}] \times 2 \sim 1.3$ degrees. Figure 4.26 shows the two-photon opening angle distribution. The opening angle of π^0 decreases with increasing p_T while the opening angle of cosmic or hadron events stay at the same expected angle.

To support the statement above, Time of Flight (TOF) distributions are shown for two selected p_T bins in Fig. 4.27. The black line shows the TOF distribution inside the π^0 mass window, and the red line shows TOF under the cosmic ray and hadron background peak around $\sim 0 \text{ GeV}/c^2$. There are two components. Please note that the resolution of TOF is limited to $\sim 3 \text{ nsec}$ since BBC time zero subtraction was not done. In addition, time of flight quality assurance is not complete. The plot is to show for a rough qualitative statement only. As in the Fig. 4.27, one is collision related and the other is collision

Figure 4.26: Opening angle distribution for each p_T bin. (PbSc)

unrelated. The one with collision is from hadrons and it has longer TOF than photons. The other component which is independent of collisions comes from cosmic rays. (The peak at -60 nsec corresponds to the events with TOF measurement failure or out of the range.)

Figure 4.27: TOF distributions for photon pairs within the π^0 mass window (black), and for cosmic and hadron peak. Left: $p_T = 2.0 - 2.5$ GeV/ c . Right: $p_T = 3.0 - 4.0$ GeV/ c .

4.5.9 Cosmic ray event under π^0 signal window

As discussed in Sec. 4.5.8, the peak near ~ 0 GeV/ c^2 in a two-photon invariant mass spectrum comes from cosmic ray and hadron events. The hadron events are collision related

while the cosmic ray events are collision un-related. To estimate the amount of cosmic ray background under the π^0 peak, two-photon invariant mass spectra were obtained from the non-colliding bunches and is displayed in Fig. 4.28. The black histograms show invariant mass spectra from the colliding bunches, the red histograms are from non-colliding bunch crossings, scaled by the number of bunches. (The number of colliding bunches / the number of non-colliding bunches) Background in the lowest $p_T(1.0 - 1.5\text{GeV}/c)$ is $\sim 0.1\%$ Background in the highest $p_T(3.0 - 4.0\text{GeV}/c)$ is $\sim 1\%$ or less. Cosmic ray events are thought to have zero asymmetries thus the effect on the measured asymmetry is negligible. At the highest p_T , the peaks near $0\text{ GeV}/c$ in black and red histograms match well. Thus in the highest p_T , cosmic ray events dominate in the peak. For $p_T = 1.0 - 1.5\text{ GeV}/c$, the peak near $\sim 0\text{ GeV}/c^2$ is larger in PbSc than that in PbGl, and hadron events dominate since PbGl detects Čerenkov radiation and is less sensitive to hadron events than PbSc.

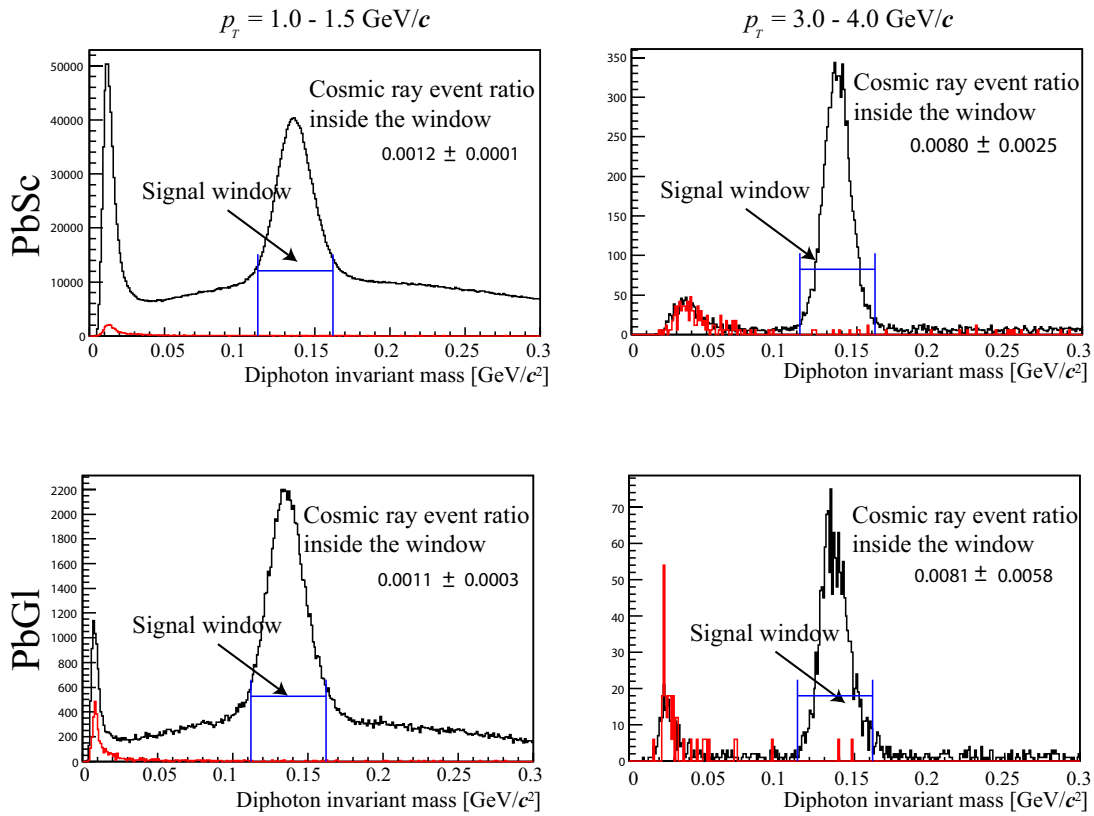


Figure 4.28: Two-photon invariant mass spectrum for $p_T = 1.0 - 1.5\text{ GeV}/c$ and $p_T = 3.0 - 4.0\text{ GeV}/c$, in PbSc and PbGl. The black histograms are for the events in the colliding bunch crossings, and the red ones are for that in the non-colliding bunch crossings, scaled by the number of bunch crossings.

4.5.10 Vertex cut difference in π^0 and BBC trigger

The high- p_T photon trigger was used to collect π^0 sample, while relative luminosity is calculated with the BBC trigger counts. The vertex position cuts are slightly different between them. Therefore, the effect of the cut difference on the measured A_{LL} is estimated in this subsection.

The vertex cut in the BBC trigger is implemented by utilizing the time difference between the hits in BBCN and BBCS as explained in Sec. 3.4.1. The high- p_T photon trigger does not have explicit vertex cut. Instead, the z axis is surrounded by the central magnet for $|z| > 41$ cm, thus the measured π^0 has a vertex cut-off but slightly different from the vertex cut in the BBC trigger.

We define a ratio $r = N_{\pi^0+BG}/N_{\text{BBC}}$, where N_{π^0+BG} is the counts for the signal window in two-photon invariant mass spectrum for $p_T > 1$ GeV/ c which is defined in Sec. 4.6.1, and N_{BBC} is the BBC trigger counts. The ratio r can be written (in case there is no vertex width variations) as $r = C(1 + \varepsilon_{LL}\text{sgn}(P_BP_Y))$ where ε_{LL} is the raw asymmetry of $\pi^0 + BG$ and it relates to the double helicity asymmetry as $A_{LL} = \varepsilon_{LL}/(P_BP_Y)$. r depends not only on spin, but also the vertex width as discussed in Sec. 4.4. The purpose of the thesis is to measure A_{LL} that is the dependence of r on spin. In this subsection, the dependence of r on the vertex width is estimated with a simple Monte Carlo (MC). The obtained dependence is utilized to estimate the overall effect on A_{LL} . Necessary ingredients for the MC are the z (vertex position) dependence of π^0 detection efficiency and the BBC trigger efficiency.

The z dependence of the BBC trigger efficiency is expressed as

$$f_{\text{BBC}}(z) = \varepsilon_{\text{BBCno-vcut}}(z) \cdot \varepsilon_{\text{BBCvcut}}(z). \quad (4.25)$$

where $\varepsilon_{\text{BBCno-vcut}}(z)$ is the z dependent BBC detection efficiency without vertex cut and $\varepsilon_{\text{BBCvcut}}(z)$ is the z dependent BBC vertex cut efficiency. $\varepsilon_{\text{BBCno-vcut}}(z)$ is measured and well reproduced by a Gaussian with sigma of 95 ± 10 cm as described in Appendix A. $\varepsilon_{\text{BBCvcut}}(z)$ is measured by comparing the counts in BBC no vertex cut trigger with and without the BBC trigger fired. The results are displayed in Fig. 4.29 with a fit function. It can be well approximated by a combination of two error functions

$$\text{Erf}(x) = \frac{2}{\sqrt{\pi}} \int_0^x \exp(-t^2) dt \quad (4.26)$$

$$\varepsilon_{\text{BBCvcut}}(z) = p_0 \text{Erf}\left(\frac{z-p_1}{\sqrt{2}p_2}\right) / 2 \cdot \left(1 - \text{Erf}\left(\frac{z-p_3}{\sqrt{2}p_2}\right)\right) / 2. \quad (4.27)$$

where p_0 , p_1 , p_2 , and p_3 are the fit parameters. p_0 is the normalization, p_1 and p_3 are the vertex cut edge on negative and positive z sides respectively. p_2 is the resolution of the vertex cut. For the MC, the obtained histogram is utilized instead of the fit function since the χ^2 is not good. But the results did not change anyway.

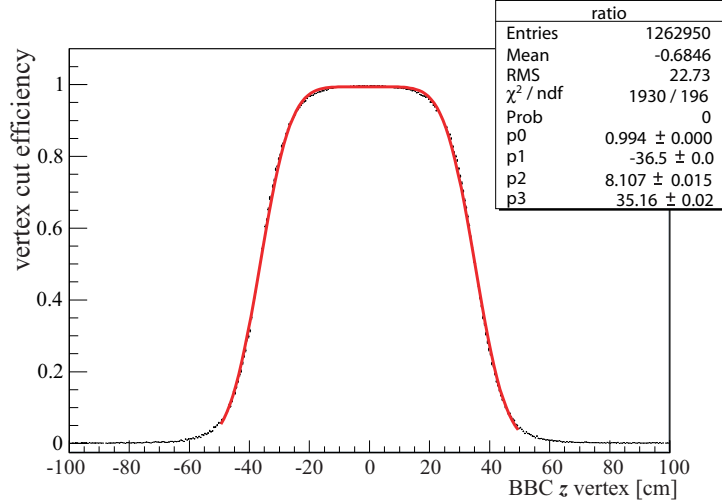


Figure 4.29: BBC trigger vertex cut efficiency.

The z dependence of π^0 detection efficiency with BBC z vertex reconstructed, is expressed as

$$f_{\pi^0, BBC}(z) = \varepsilon_{\pi^0}(z) \cdot \varepsilon_{BBC\text{no-vcut}}(z). \quad (4.28)$$

where $\varepsilon_{\pi^0}(z)$ is the z dependent π^0 efficiency which includes the acceptance of the EMCAL. Figure 4.30 displays the obtained $\varepsilon_{\pi^0}(z)$.

The π^0 counts for $|z| > 50$ cm is only $(7.17 \pm 0.095) \times 10^{-3}$ for the same helicity combinations and $(7.23 \pm 0.095) \times 10^{-3}$ for the opposite helicity combinations. They are consistent within the statistical uncertainty. The statistical uncertainty propagates to A_{LL} as $9.5 \times 10^{-5} / \langle P_B P_Y \rangle \sim 4.1 \times 10^{-4}$ thus it is negligible compared to the assigned systematic uncertainty from the relative luminosity. Therefore, the following discussion only consider $|z| < 50$ cm. Correcting BBC efficiency mentioned above only increase the amount of π^0 counts for $|z| > 50$ cm about 20% in counts thus does not change the results.

The dependence of r on vertex width is estimated by utilizing a simple MC with the information obtained above. Input is a Gaussian distribution which simulates the observed vertex distribution in BBC no vertex triggered events. As shown in Fig. 4.5, the observed vertex distribution is well reproduced by a Gaussian for $|z| < 100$ cm. The probability of π^0 to be observed for a randomly obtained z position is calculated by $\varepsilon_{\pi^0}(z) / \varepsilon_{BBC\text{no-vcut}}(z)$. And the probability of BBC counts to be observed is calculated by $\varepsilon_{BBC}(z)$. The absolute efficiency is not the source of systematic uncertainty. Therefore, the probability is made to be 100% for $\varepsilon_{BBC\text{no-vcut}}$ where the probability is the highest and 80% for ε_{π^0} not to exceed 100% by $\varepsilon_{BBC\text{no-vcut}}$ correction. Figure 4.31 shows the vertex width dependence of the ratio between π^0 counts and the BBC trigger counts (with vertex cut) obtained by the simple MC. The measured vertex width is within the

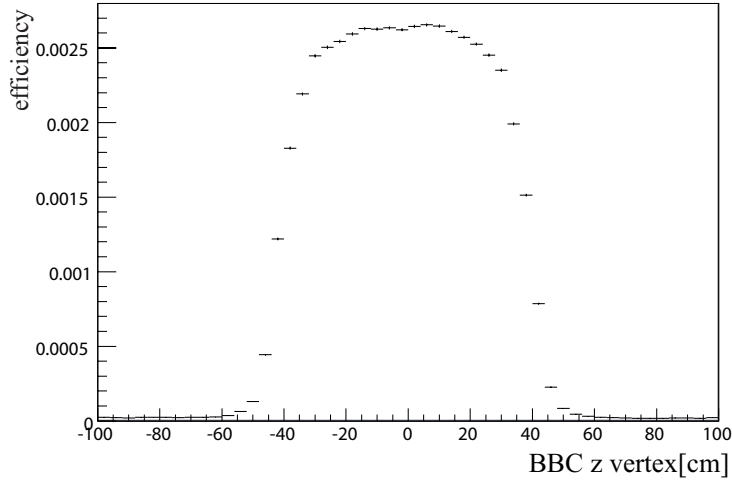


Figure 4.30: z vertex dependence of π^0 relative efficiency.

range ($55 < \sigma < 65$ cm) and the ratio is linearly dependent on the width. The dependence is obtained to be $\sim 3.6 \times 10^{-4}/\text{cm}$. ($3.2 \times 10^{-4}/0.88$).

The bunch by bunch width for each fill were weight-averaged to obtain the widths for helicity same and opposite combination separately to estimate the overall effect on A_{LL} . Figure 4.32 displays the difference of width in the different helicity combinations. The difference is consistent with zero and obtained to be 0.053 ± 0.049 for the longitudinal run period. Taking one σ , the uncertainty propagates to A_{LL} as $\sim 0.36/\langle P_B P_Y \rangle \sim 1.6 \times 10^{-4}$. Similar results were obtained for the background window. The uncertainty is one order smaller than the uncertainty from the relative luminosity. Therefore, the vertex cut difference have negligible effect on the measured A_{LL} .

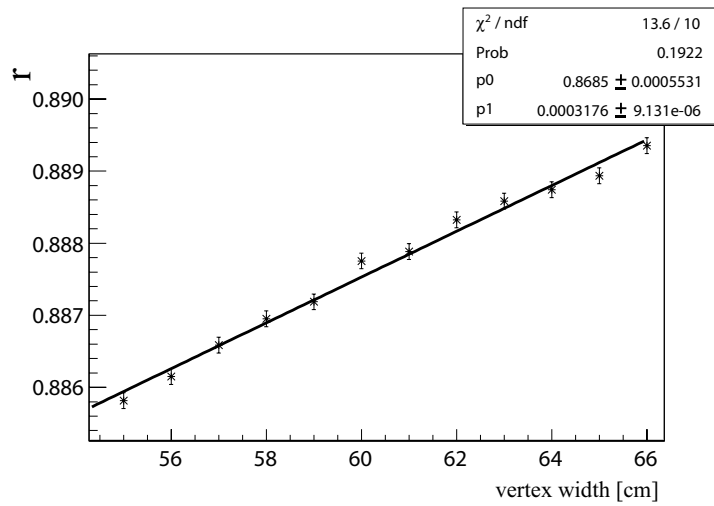


Figure 4.31: a MC results of width dependence.

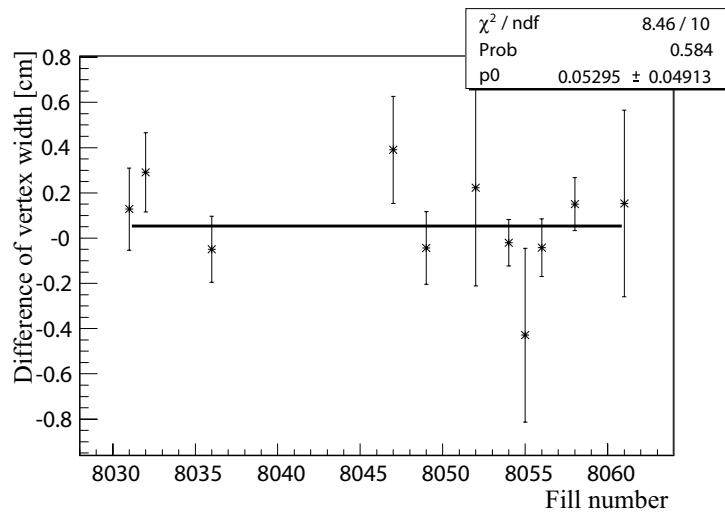


Figure 4.32: difference in vertex width.

4.6 Spin asymmetries

4.6.1 Calculation of the asymmetries

The goal of the thesis is to extract double helicity asymmetry A_{LL} of π^0 . In addition to A_{LL} , double transverse spin asymmetries A_{TT} , and single longitudinal spin asymmetries A_L were also obtained for a study on systematic uncertainties. A_L is defined in Sec. 4.6.4.

We take A_{LL} as an example to explain the procedure to extract asymmetries since the procedures are the same for A_{TT} and A_L .

The double helicity asymmetry A_{LL} is calculated as

$$A_{LL} = \frac{1}{P_B P_Y} \frac{N_{++}/L_{++} - N_{+-}/L_{+-}}{N_{++}/L_{++} + N_{+-}/L_{+-}} \quad (4.29)$$

$$= \frac{1}{P_B P_Y} \frac{N_{++} - RN_{+-}}{N_{++} + RN_{+-}} \quad \text{where} \quad R = \frac{L_{++}}{L_{+-}} \quad (4.30)$$

P_B (P_Y) is the polarization of the Blue (Yellow) beam and N_{++} (N_{+-}) is the particle yield in the same (opposite) helicity bunch crossings, and R is the relative luminosity between bunches with the same and opposite helicities. π^0 is identified by constructing invariant mass of two decay photons and the background under π^0 peak is indistinguishable from the signals. The amount of π^0 signals could be obtained in principle by a fit for different polarization sign separately and A_{LL} can be directly calculated for π^0 signals. However, A_{LL} must be calculated run-by-run or fill-by-fill as explained in Sec. 4.5.1. Therefore, the method suffers from π^0 yield-extraction uncertainty. Instead, the asymmetry for π^0 and background, $A_{LL}^{\pi^0+BG}$, was calculated and the contribution on the asymmetry from the background, A_{LL}^{BG} , was subtracted to obtain the physics asymmetries of π^0 , $A_{LL}^{\pi^0}$.

$A_{LL}^{\pi^0+BG}$ were calculated using the yields in signal window, which is defined as the mass range 137 ± 25 MeV/ c^2 .¹ The width corresponds to $\sim 2\sigma$ of the π^0 peak. The background asymmetry A_{LL}^{BG} under π^0 peak cannot be directly measured. It is replaced by the background asymmetry of the side band $177 - 217$ MeV/ c^2 , assuming that the background asymmetry under the π^0 peak is the same as that in the side band. Figure 4.33 illustrates the signal window and the background window used for asymmetry calculations. The lower side band was not used in this analysis to avoid possible effect from the cosmic ray and hadron background peak. See Sec. 4.5.8 for the cosmic ray and hadron background peak. It was confirmed that the asymmetries for the lower and higher side band are consistent with zero.

The subtraction is performed by the following formula:

$$A_{LL}^{\pi^0} = \frac{A_{LL}^{\pi^0+BG} - r A_{LL}^{BG}}{1 - r} \quad \text{where} \quad r = \frac{N_{BG}}{N_{\pi^0+BG}}, \quad (4.31)$$

¹The peak position of π^0 mass is ~ 137 MeV/ c^2 (which is slightly higher than the world-average of π^0 mass) due to the energy smearing effect as explained in Sec. 4.5.5

$$\delta A_{LL}^{\pi^0} = \frac{\sqrt{(\delta A_{LL}^{\pi^0+BG})^2 + r^2 (\delta A_{LL}^{BG})^2}}{1 - r}. \quad (4.32)$$

The procedure to extract the background ratio r is explained later.

For a calculation of A_{LL} , the data are required to have more than 10 counts for same and opposite helicity bunch crossings for the statistical uncertainty of Poisson distribution to be approximated by that of Gaussian distribution. This is just rejecting low statistics runs and does not bias the measurement.

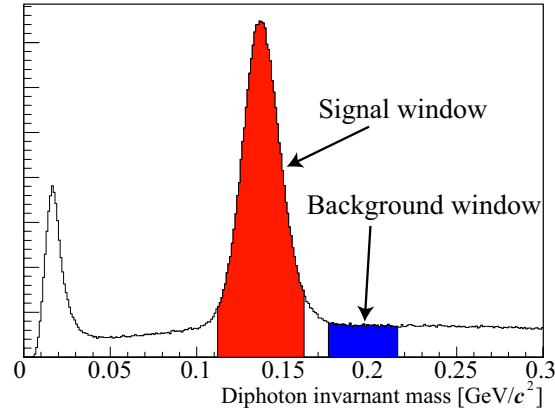


Figure 4.33: The ranges used for asymmetry calculations. The red area corresponds to the signal window (signal + background), and the blue area describes the background window.

The statistical uncertainties of A_{LL} is calculated as:

$$\delta A_{LL} = \frac{1}{P_B P_Y} \frac{2RN_{++}N_{+-}}{(N_{++} + RN_{+-})^2} \sqrt{\left(\frac{\delta N_{++}}{N_{++}}\right)^2 + \left(\frac{\delta N_{+-}}{N_{+-}}\right)^2 + \left(\frac{\delta R}{R}\right)^2}. \quad (4.33)$$

The calculation of statistical uncertainty needs careful consideration since the number of signals no longer obey the Poisson distribution. Let N^{sig} be the number of signals, N^{trig} be the number of triggered events, and $\langle k \rangle$ ($\langle k^2 \rangle$) be the average number (squared) of signals in one event. N^{trig} obeys the Poisson distribution and its statistical uncertainty is approximated by that of Gaussian distribution as $\delta N^{trig} = \sqrt{N^{trig}}$. The statistical uncertainty of N^{sig} is calculated as

$$\delta N^{sig} = \sqrt{\frac{\langle k^2 \rangle}{\langle k \rangle}} \times \sqrt{N^{sig}}. \quad (4.34)$$

$\sqrt{\frac{\langle k^2 \rangle}{\langle k \rangle}}$ is referred to as the enhancement factor since the statistical uncertainty is that of a Poisson distribution times the enhancement factor. They were obtained for each p_T bins and were summarized in Table 4.5.

p_T [GeV/c]	$\sqrt{\langle k^2 \rangle / \langle k \rangle}$	
	Signal window	Background window
1.0 – 1.5	1.09	1.06
1.5 – 2.0	1.04	1.03
2.0 – 2.5	1.02	1.03
2.5 – 3.0	1.02	1.02
3.0 – 4.0	1.02	1.02

Table 4.5: The enhancement factor for the statistical uncertainties for each p_T bins.

4.6.2 Background ratio in signal window

Background ratio in signal window, which is defined in Sec. 4.6.1, is necessary to subtract the background asymmetry under π^0 mass peak. The background ratio is defined as $r = \frac{N_{BG}}{N_{\pi^0} + N_{BG}}$, where N_{BG} and N_{π^0} are the number of background and π^0 counts in the signal window. (It was introduced in Eq. 4.31.) To evaluate the background ratio, the invariant mass spectra were fitted with a combination of three functions: $f_{\cos}(x)$, $f_{\text{comb}}(x)$, and $f_{\text{sig}}(x)$. $f_{\cos}(x)$ represents the tail of the cosmic ray and hadron events near ~ 0 GeV/ c^2 and exponential was assumed. $f_{\text{comb}}(x)$ describes combinatorial background and a quadratic function or a linear function was assumed. Quadratic functions were assumed for $p_T < 2.5$ GeV/ c since low p_T spectra were not well reproduced by linear functions. $f_{\text{sig}}(x)$ represents π^0 mass peak and Gaussian was assumed. Figure 4.34 displays an example of the fit. The black curve shows the sum of the functions while red, purple and blue curves describe the contribution from the functions separately. The curves were drawn for the range used for the fit. The π^0 mass peak was not well reproduced by a Gaussian shape which results in large reduced χ^2 , ~ 19 for the lowest p_T and ~ 3 for the highest p_T bin. Thus the amount of signal and background in the signal window is simply obtained by counting the measured yields, while the amount of the background is estimated by the fit function. The statistical uncertainties assigned from the fit were enlarged by square root of the reduced χ^2 of the fit and assigned as systematic uncertainties. The difference between the counts and integral of the fit function in the signal window is within the assigned systematic uncertainties. The fit range was also varied and the results were compared but the difference was within the assigned systematic uncertainties.

The obtained background ratio and the systematic uncertainties for each p_T bin are summarized in Table. 4.6.

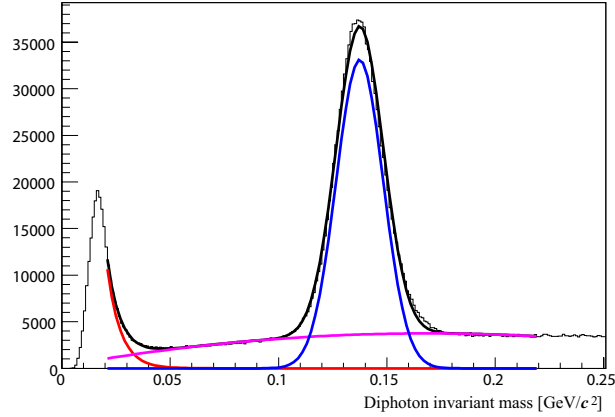


Figure 4.34: Background ratio estimate by a fit. The functions $f_{\cos}(x)$, $f_{\text{comb}}(x)$, and $f_{\text{sig}}(x)$ were used. See text for the definitions. The black curve shows the sum of the functions while red, purple and blue curves describe the contribution from the functions separately. The curves were drawn for the range used for the fit.

p_T [GeV/c]	BG ratio in signal window
1.0 – 1.5	0.350 ± 0.008
1.5 – 2.0	0.170 ± 0.010
2.0 – 2.5	0.100 ± 0.015
2.5 – 3.0	0.055 ± 0.002
3.0 – 4.0	0.039 ± 0.004

Table 4.6: Background (BG) ratios and their systematic uncertainties in signal window for each p_T bins.

4.6.3 Average p_T

The calculated asymmetries are plotted at the average p_T , $\langle p_T \rangle$, for each p_T bin. As in the case of the asymmetries, it requires background correction to obtain the average p_T of π^0 . It is obtained with the following formula:

$$\langle p_T^{\pi^0} \rangle = \frac{\langle p_T^{\pi^0+\text{BG}} \rangle - r \langle p_T^{\text{BG}} \rangle}{1 - r} \quad \text{where} \quad r = \frac{N_{\text{BG}}}{N_{\pi^0+\text{BG}}} \quad (4.35)$$

The obtained average p_T for each p_T bin is listed in Table.4.7. The statistical uncertainties and the effect from the systematic uncertainty of background ratio obtained in Sec. 4.6.2 are negligible compared to the absolute energy scale uncertainty of 1.2%.

p_T [GeV/c]	$\langle p_T^{\pi^0} \rangle$ [GeV/c]
1.0-1.5	1.21
1.5-2.0	1.70
2.0-2.5	2.20
2.5-3.0	2.70
3.0-4.0	3.32

Table 4.7: The average p_T for each p_T bin.

4.6.4 Asymmetries

Double helicity asymmetries A_{LL}

The double helicity asymmetry A_{LL} of π^0 were obtained as explained in Sec. 4.6.1. The asymmetries were calculated run by run for $p_T < 3$ GeV/c and fill by fill for $p_T > 3$ GeV/c as explained in Sec. 4.5.1. Figure 4.35 ² shows run-by-run A_{LL} results for even bunch crossings, signal window, and $p_T = 1.5 - 2.0$ GeV/c as an example. It was fitted to a constant and $A_{LL}^{\pi^0+BG}$ was obtained. A_{LL}^{BG} was also obtained in the same way and subtracted using π^0 purity measured as in Sec. 4.6.2. The results of A_{LL} were calculated separately for even and odd bunch crossings, and they are averaged to obtain the final results. The final results of A_{LL} for even and odd bunch crossings separately and the combined results are displayed in Fig. 4.36.

Double transverse spin asymmetries A_{TT}

Our purpose is to measure A_{LL} but the measured A_{LL} is affected by the double transverse spin asymmetry A_{TT} through the remaining transverse components of the beam polarizations as discussed in Sec. 4.7.2. Thus A_{TT} was also obtained in this analysis. A_{TT} should have azimuthal angle dependence and is proportional to $\cos(2\phi)$. Therefore, measured asymmetry A_{TT}^{meas} should be corrected for angle dependence to obtain the physics asymmetry A_{TT} . But as explained in Sec. 4.7.2, the correction is not necessary for this analysis and the correction was not performed. The measured A_{TT}^{meas} without angle-dependence correction was displayed in Fig. 4.37 and listed in Table. 4.8. The gray band indicate the systematic uncertainty from the relative luminosity as discussed in Sec. 4.4.

²Between fills, ~ 100 run numbers are consumed for detector calibrations and diagnostics of DAQ. Therefore, gaps of ~ 100 runs appear in the figure.

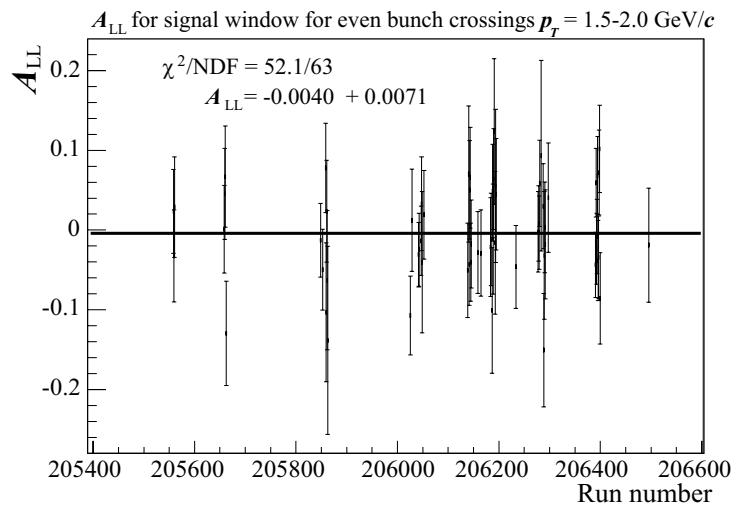


Figure 4.35: Run-by-run results of $A_{LL}^{\pi^0+BG}$ for even bunch crossings at $p_T = 1.5 - 2.0$ GeV/c.

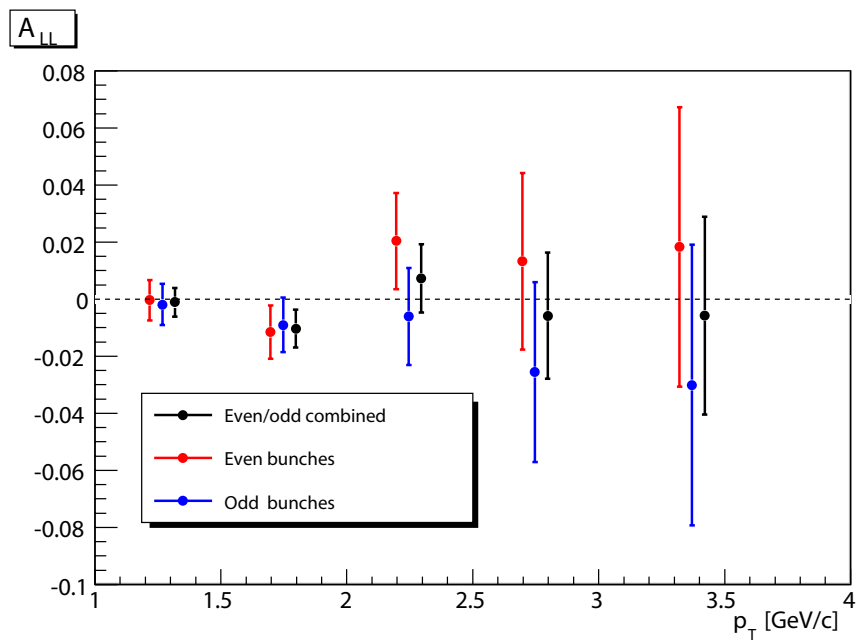


Figure 4.36: The results of $A_{LL}^{\pi^0}$ for even (red) and odd (blue) bunch crossings and the combined results (black).

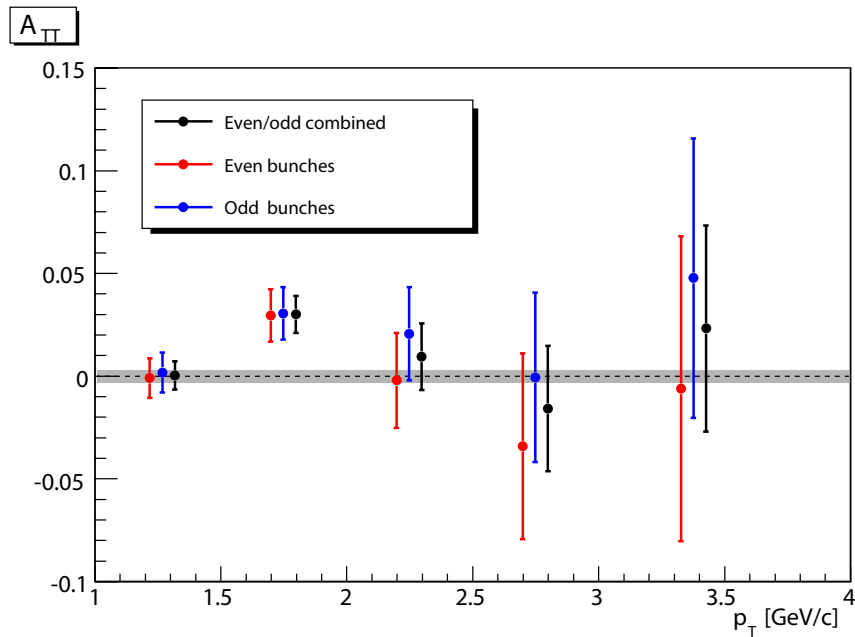


Figure 4.37: Results of $A_{TT}^{\pi^0}$ for even (red) and odd (blue) and the combined results (black). The gray band shows the systematic uncertainty from the relative luminosity.

p_T bin	$\langle p_T \rangle$	$A_{TT}^{\pi^0}$
1.0 – 1.5	1.22	$4.0 \times 10^{-4} \pm 6.8 \times 10^{-3}$
1.5 – 2.0	1.70	$3.0 \times 10^{-2} \pm 9.1 \times 10^{-3}$
2.0 – 2.5	2.20	$9.4 \times 10^{-3} \pm 1.6 \times 10^{-2}$
2.5 – 3.0	2.70	$-1.6 \times 10^{-2} \pm 3.0 \times 10^{-2}$
3.0 – 4.0	3.33	$2.3 \times 10^{-2} \pm 5.0 \times 10^{-2}$

Table 4.8: Results of $A_{TT}^{\pi^0}$.

Single spin asymmetries A_L

Single spin asymmetry A_L is defined as

$$A_L \equiv -\frac{1}{P} \frac{\sigma_+ - \sigma_-}{\sigma_+ + \sigma_-}, \quad (4.36)$$

where P is the polarization of the polarized beam, and σ_+ and σ_- are the cross sections for the helicity $+$ and $-$ collisions respectively. Non-zero single spin asymmetry requires parity violation in physics process, that is the weak interactions. It is expected to be very small ($A_L < 10^{-5}$) at $\sqrt{s} = 200$ GeV [77] and be smaller than that at $\sqrt{s} = 62.4$ GeV.

It is experimentally calculated as

$$A_L = -\frac{1}{P} \frac{N_+ - RN_-}{N_+ + RN_-}, \quad \text{where.} \quad R_{\text{single}} = \frac{L_+}{L_-} \quad (4.37)$$

N_+ (N_-) is the particle yields in the collisions with helicity $+$ ($-$) state in one beam and either helicity state in the other beam. R_{single} is the relative luminosity for helicity $+$ and $-$ beam collisions. It was measured in a similar way as described in Sec. 4.6.1. Since both Blue and Yellow beams are polarized, A_L can be measured for each beam separately.

Figure 4.38 displays the results of A_L for Blue and Yellow beams separately and they are consistent with zero as expected.

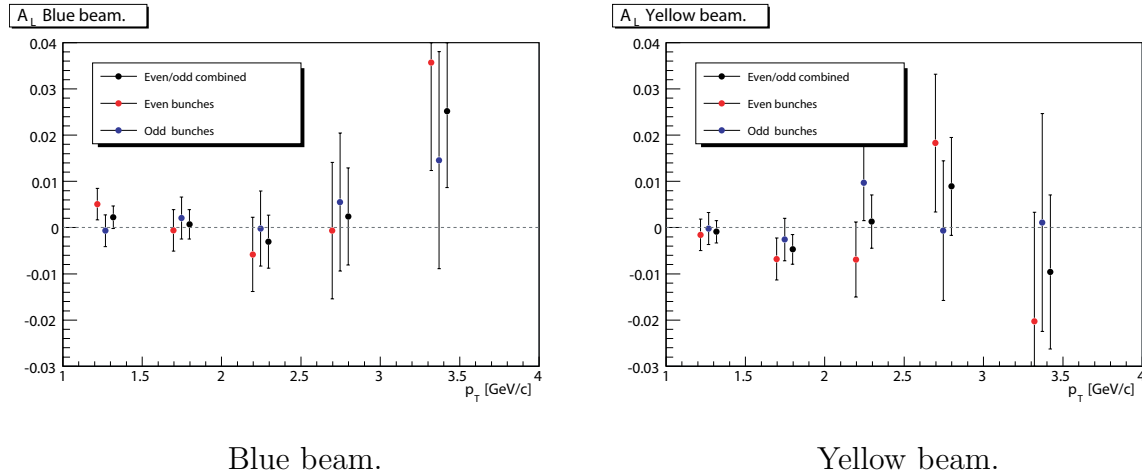


Figure 4.38: The results of $A_L^{\pi^0}$ for the Blue (left) and Yellow (right) beams. Red points are for even, blue for odd, and black for the combined results.

4.7 Systematic uncertainties

Sources of systematic uncertainties on the analysis are discussed in this section. Bunch shuffling technique was utilized to confirm the validity of the assigned uncertainties and

is described in Sec. 4.7.4. The assigned systematic uncertainties are summarized in Sec. 4.7.6.

4.7.1 Beam polarizations

The uncertainty of A_{LL} due to the beam polarizations propagates as,

$$\delta A_{LL}^{\text{pol}} = \frac{\delta(P_B P_Y)}{P_B P_Y} A_{LL}. \quad (4.38)$$

The uncertainty correlates over all p_T , thus behave as a scale uncertainty, where the central values and the uncertainties are changed by the same factor. The systematic uncertainty of 13.9% was assigned for the beam polarizations. The major contributor to the systematic uncertainty is the statistical uncertainty in the H-jet polarimeter measurement.

4.7.2 Beam polarization orientations

The beam polarization orientations were measured with the PHENIX local polarimeter as described in Sec. 3.2.3. The fraction of the transverse components are $\langle P_T/P \rangle^B = 0.11 \pm 0.15$ for the Blue beam, $\langle P_T/P \rangle^Y = 0.11 \pm 0.12$ for the Yellow beam. Thus the beams are fully longitudinally polarized within the uncertainties and the longitudinal components are $\langle P_L/P \rangle^B = 1.000 - 0.023$ for the Blue beam, $\langle P_L/P \rangle^Y = 1.000 - 0.022$ for the Yellow beam.

The beam polarization orientations affect in two ways: The effect from the uncertainty of the longitudinal components of the beams, and the effect from A_{TT} through transverse components of the beams.

The effect from the uncertainty of the longitudinal components of the beams

The A_{LL} was calculated as the polarization is fully longitudinally polarized. The uncertainty of A_{LL} from the uncertainty of longitudinal components of the beam polarizations, $\delta A_{LL}^{\text{uncert.long.}}$, is calculated as

$$\delta A_{LL}^{\text{uncert.long.}} = \delta \left(\frac{1}{P'_{B,L}} \frac{1}{P'_{Y,L}} \right) A_{LL}^{\text{meas}} \quad (4.39)$$

$$= \frac{A_{LL}}{P'_{B,L} P'_{Y,L}} \sqrt{\left(\frac{\delta P'_{B,L}}{P'_{B,L}} \right)^2 + \left(\frac{\delta P'_{Y,L}}{P'_{Y,L}} \right)^2}, \quad (4.40)$$

where $P'_{B,L} = \frac{P_{B,L}}{P}$ and $P'_{Y,L} = \frac{P_{Y,L}}{P}$. Thus a systematic uncertainty of 3.2% (2.3% \oplus 2.4%) was assigned for the effect. The uncertainty is p_T -correlated and behaves as a scale uncertainty.

The effect from the A_{TT} through the transverse components of the beams

In addition, the measured A_{LL} is affected by A_{TT} through the transverse components of the beams. The effect on A_{LL} is:

$$\delta A_{LL} = \frac{P_{B,T}P_{Y,T}}{P_B P_Y} A_{TT}^{\text{meas}}. \quad (4.41)$$

The effect was calculated with the measured A_{TT} and the polarizations. The central values plus one σ were assigned as the systematic uncertainties and is summarized in Table 4.9. The assigned uncertainties are smaller compared to the major systematic uncertainty from relative luminosity (besides the scale uncertainty from the beam polarization).

4.7.3 Relative luminosity

The uncertainty of relative luminosity is assigned as $\delta A_{LL} = 1.4 \times 10^{-3}$ as described in Sec. 4.4.

4.7.4 Bunch shuffling

Bunch shuffling is a technique to evaluate the validity of the uncertainty of the asymmetry calculations. The asymmetry calculations were performed in the same way as the true asymmetry calculations but with the polarization signs randomly assigned to the bunch crossings. Such calculations were repeated and accumulated. Figure 4.39 displays an example of the shuffled A_{LL} variations. They are fitted to Gaussian to obtain σ for the shuffled variations. They are compared with the uncertainty for the true asymmetries.

Figure 4.40 display the ratio between the σ of the shuffled A_{LL} variations and the statistical uncertainty of true A_{LL} versus p_T . The statistical uncertainties were well reproduced by the shuffled results and no further systematic uncertainties were found in this analysis.

4.7.5 Double collision effect

The BBC trigger cannot distinguish two collisions if they occur at exactly the same bunch crossing. Double collision would make measured luminosity lower than the the actual luminosity. Thus it is important to estimate the double collision rate.

The total cross section (σ_{tot}) and the elastic scattering cross section (σ_{el}) of pp collisions at $\sqrt{s} = 62.4$ GeV are $\sigma_{tot} \sim 43$ mb, and $\sigma_{el} \sim 7.5$ mb, respectively [78]. Thus the inelastic scattering cross section becomes $\sigma_{inel} \sim 35.5$ mb. The cross section of events which the BBCs detect is $\sigma_{BBC} = 13.7$ mb, which is about 40% of the inelastic scattering cross sections. The rate of the BBC trigger without vertex cut was at most 15 kHz

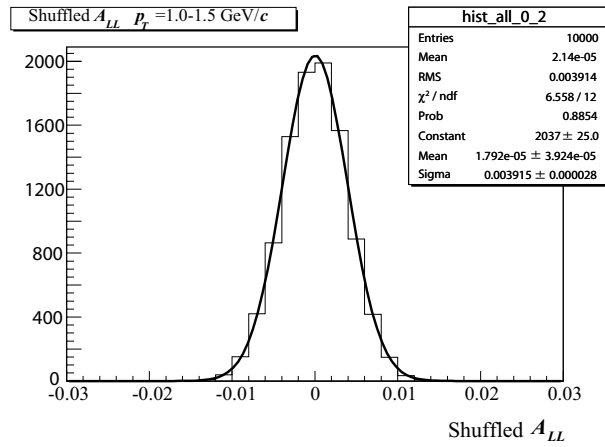


Figure 4.39: The shuffled A_{LL} variations for the signal window and $p_T = 1.0 - 1.5$ GeV/ c in even bunch crossings.

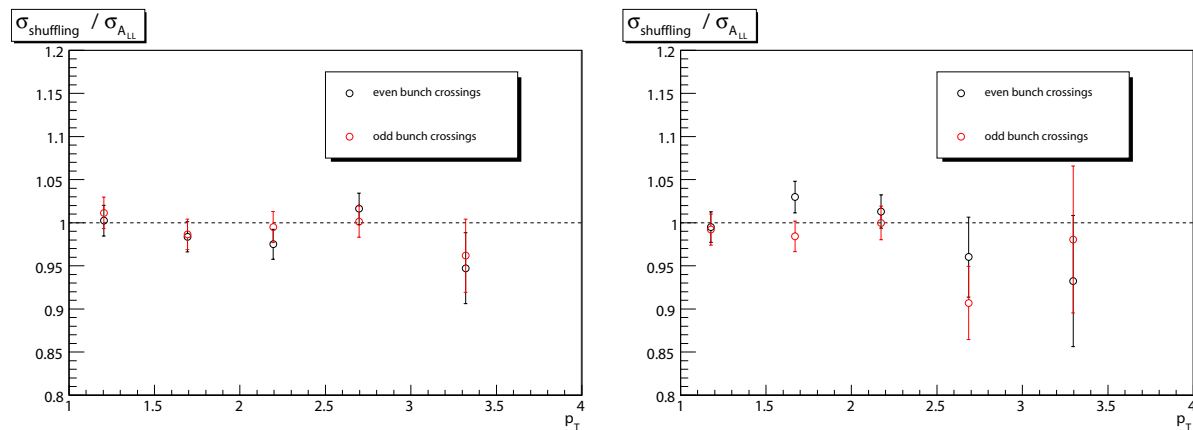


Figure 4.40: The ratio of the σ of the shuffled A_{LL} variations and the statistical uncertainty of true A_{LL} for π^0 +background (left), and background (right) windows. Black circles are for the even bunch crossings, and Red ones are for the odd bunch crossings.

at $\sqrt{s} = 62.4$ GeV in Run 2006. Thus the real collision rate (inelastic scattering rate) is at most $15/0.4 \sim 38$ kHz. Since RHIC has 9.4MHz (1/106 nsec) basket of beam with ~ 100 out of 120 bunches filled, the single collision probability is $\sim 0.49\%$. The collision probability obeys the Poisson distribution with parameter $\lambda = 0.0049$. Thus the probability to have k collisions in a bunch crossing, p_k , is calculated to be

$$p_k = \frac{e^{-\lambda} \lambda^k}{k!}. \quad (4.42)$$

Therefore, probability to have more than one collision per bunch is $\sim 0.0012\%$ and is negligible.

4.7.6 Summary of the systematic uncertainties

The sources of systematic uncertainties are;

- Relative luminosity.
- A_{TT} contamination through transverse component of the beam polarizations.
- Background ratio in the signal window.
- (Scale uncertainty) Polarizations of the beams
- (Scale uncertainty) Longitudinal components of the polarizations.

The last two items were treated separately since they are scale uncertainties. The uncertainty of 14% ($13.9\% \oplus 3.2\%$) was assigned. The systematic uncertainties are summarized in Table. 4.9. The systematic uncertainty is about 28% of the statistical uncertainty for the lowest p_T where the statistics are the largest. The dominant systematic uncertainty originates from the relative luminosity.

p_T (GeV/c)	A_{TT} effect	Rel. lumi. ($\times 10^{-4}$)	BG ratio	total ($\times 10^{-4}$)
1.0 – 1.5	0.87	14	1.8	14
1.5 – 2.0	10	14	3.6	18
2.0 – 2.5	3.9	14	3.9	15
2.5 – 3.0	6.9	14	0.3	16
3.0 – 4.0	11	14	13	22

Table 4.9: Systematic uncertainties for A_{LL} . The scale uncertainty of 14% which comes from the beam polarizations was not listed in the table.

Chapter 5

Results and discussions

In this chapter, we present and discuss the results of π^0 A_{LL} in polarized pp collisions at $\sqrt{s} = 62.4$ GeV.

Although lower \sqrt{s} has advantage in probing high x range, it should not be too low. In fact, NLO pQCD calculation fail to describe low-energy fixed-target experiments. Therefore, it is important to confirm pQCD applicability since the polarized gluon distributions are extracted based on pQCD. Before presenting and discussing the results of A_{LL} , which is the main subject of the thesis, the results of the cross sections are shown and the applicability of pQCD is discussed in Sec. 5.1. Then the results of A_{LL} are presented and discussed in Sec. 5.2. Two global analyses on polarized PDFs which included our A_{LL} results are discussed in Sec. 5.3.

5.1 The cross section results

Figure 5.1 presents the inclusive mid-rapidity π^0 invariant production cross sections at $\sqrt{s} = 62.4$ GeV versus p_T , from $p_T = 0.5$ GeV/ c to $p_T = 7$ GeV/ c [75]. They were measured with the same data set as the asymmetries. An overall normalization uncertainty of 11% due to the uncertainty in absolute normalization of the luminosity is not shown. The analyzed data sample with 0.76×10^9 BBC triggers corresponded to 55 nb^{-1} integrated luminosity. The measurements fall within the large spread of ISR data [79, 80, 81, 82, 83, 84, 85, 86, 87, 88, 89, 90]. A summary of the situation can be found in [17].

The data are compared to NLO and NLL pQCD calculations at a theory scale $\mu = p_T$, where μ represents equally-chosen factorization, renormalization, and fragmentation scales [36]. See Sec. 2.3 about the scale. The NLL corrections extend the NLO calculations to include the resummation of extra “threshold” logarithmic terms to all orders in α_s . The log terms become important in the perturbative expansion at not very high energies because the initial partons have just enough energy to produce the high p_T parton

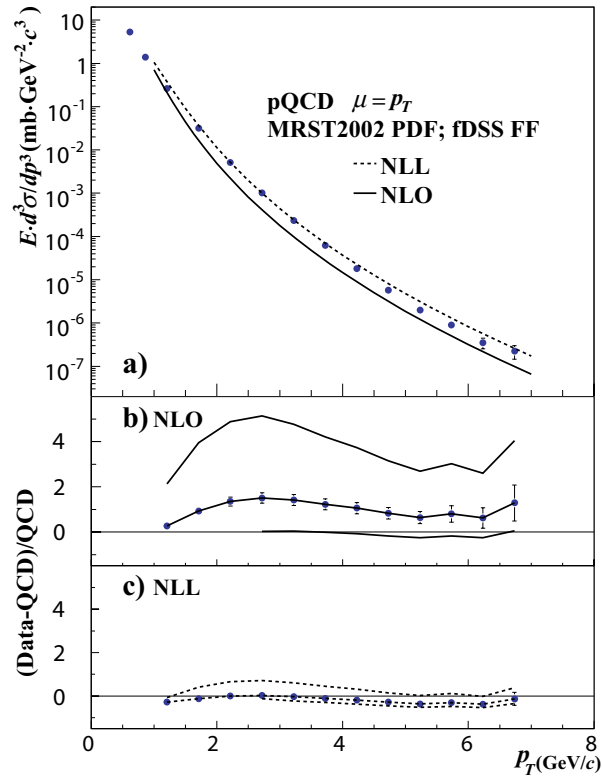


Figure 5.1: (a) The neutral pion production cross section at $\sqrt{s} = 62.4$ GeV as a function of p_T (circles) and the results of NLO (solid) and NLL (dashed) pQCD calculations for the theory scale $\mu = p_T$. (b) The relative difference between the data and NLO pQCD calculations for the three theory scales $\mu = p_T/2$ (upper line), p_T (middle line) and $2p_T$ (lower line); experimental uncertainties (excluding the 11% normalization uncertainty) are shown for the $\mu = p_T$ curve. (c) The same as b) but for NLL pQCD calculations.

that fragments into a final pion. See Sec. 2.3 about the higher order corrections. The MRST2002 parton distribution functions [39] and the fDSS set of fragmentation functions [91], which are extracted in NLO, are used in both NLO and NLL calculations. We have previously seen that the data are well described by NLO pQCD with a scale of $\mu = p_T$ at $\sqrt{s} = 200$ GeV [92, 93, 15]. In contrast, NLO calculations with the same scale underestimate the π^0 cross section at $\sqrt{s} = 62.4$ GeV. However, it does not necessarily mean that NLO fails at this energy, since NLO calculation agree with data within the theoretical uncertainties.

At the same time, it is known that NLO calculations are not always successful at describing low energy fixed target data [94], while NLL calculations have been successful [35]. The NLL calculations have a smaller scale dependence and describe our data

well with $\mu = p_T$. The scale dependence is expected to be smaller when the effect from truncation in the perturbative expansion is smaller. However, as noted in [36], subleading perturbative corrections to the NLL calculation may be significant. Therefore, we decided not to choose one from another, and we show comparisons to both NLO and NLL at a scale of $\mu = p_T$.

The data and the pQCD calculations agree well at this energy and the data can be interpreted in pQCD framework.

5.2 Results of the double helicity asymmetries

Figure 5.2 presents the measured double helicity asymmetry in π^0 production versus p_T . A scale uncertainty of 14% in $A_{LL}^{\pi^0}$ due to the uncertainty in beam polarizations is not shown. The other systematic uncertainties are negligible, as discussed in the previous chapters and checked using a technique to randomize the sign of bunch polarization.

Figure 5.2 also shows a set of A_{LL} curves from pQCD calculations that incorporates different scenarios for gluon polarization within the GRSV parametrization of the polarized parton distribution functions [95, 45]. GRSV-std corresponds to the best fit to polarized-DIS data. The other three scenarios in Fig. 5.2 (GRSV-max, $\Delta G = 0$, and $\Delta G = -G$) are based on the best fit, but use the functions $\Delta g(x_g) = g(x_g)$, 0 , $-g(x_g)$ at the initial scale for parton evolution ($Q^2 = 0.4 \text{ GeV}^2$), where $g(x_g)$ is the unpolarized gluon distribution, and $\Delta g(x_g)$ is the difference between the distributions of gluons with the same and opposite helicity to the parent proton. In Fig. 5.2, we compare our asymmetry data with both NLO and NLL calculations. Although A_{LL} is smaller in NLL calculations compared to that in NLO calculations, the difference is smaller than that at Fermilab fixed-target energies [36]. Similar to our $\sqrt{s} = 200 \text{ GeV}$ results [13, 15], our $\sqrt{s} = 62.4 \text{ GeV}$ A_{LL} data do not support a large gluon polarization scenario, such as GRSV-max.

Figure 5.3 presents the measured A_{LL} versus x_T in π^0 production overlaid with the results at $\sqrt{s} = 200 \text{ GeV}$ [15]. Clear statistical improvement can be seen at higher x_T . For the measured p_T range 2–4 GeV/c, the range of x_g in each bin is broad and spans the range $x_g = 0.06 - 0.4$, as calculated by NLO pQCD [55]. Thus our data set extends the sensitive x_g range of ΔG and also overlaps the previous measurements, providing measurements with the same x_g but at a different scale.

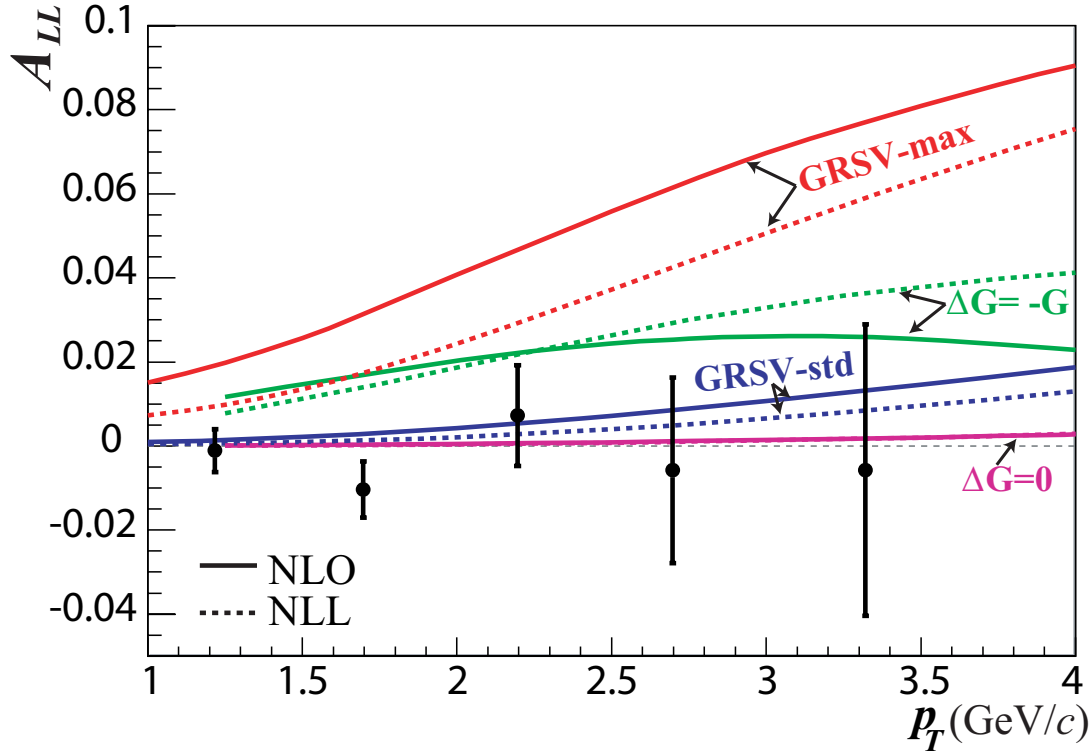


Figure 5.2: The double helicity asymmetry for neutral pion production at $\sqrt{s} = 62.4$ GeV as a function of p_T (GeV/ c). Error bars are statistical uncertainties, with the 14% overall polarization uncertainty not shown; other experimental systematic uncertainties are negligible. Four GRSV theoretical calculations based on NLO pQCD (solid curves) and on NLL pQCD (dashed curves) are also shown for comparison with the data (see text for details). Note that the $\Delta G = 0$ curves for NLO and NLL overlap.

5.3 Global analysis of polarized PDFs

Our results are already included in some of the global analysis. We introduce AAC results in section 5.3.1, and DSSV results in section 5.3.2.

5.3.1 AAC global analysis

Asymmetry Analysis Collaboration (AAC) included the preliminary version of the results in their analysis [96]. The polarized gluon PDF by the AAC group is shown in Fig. 5.4. AAC provided positively and negatively polarized gluon solutions separately in [43]. The existence of two solutions can be understood by combining Eq. 2.38 and Eq. 2.2, and

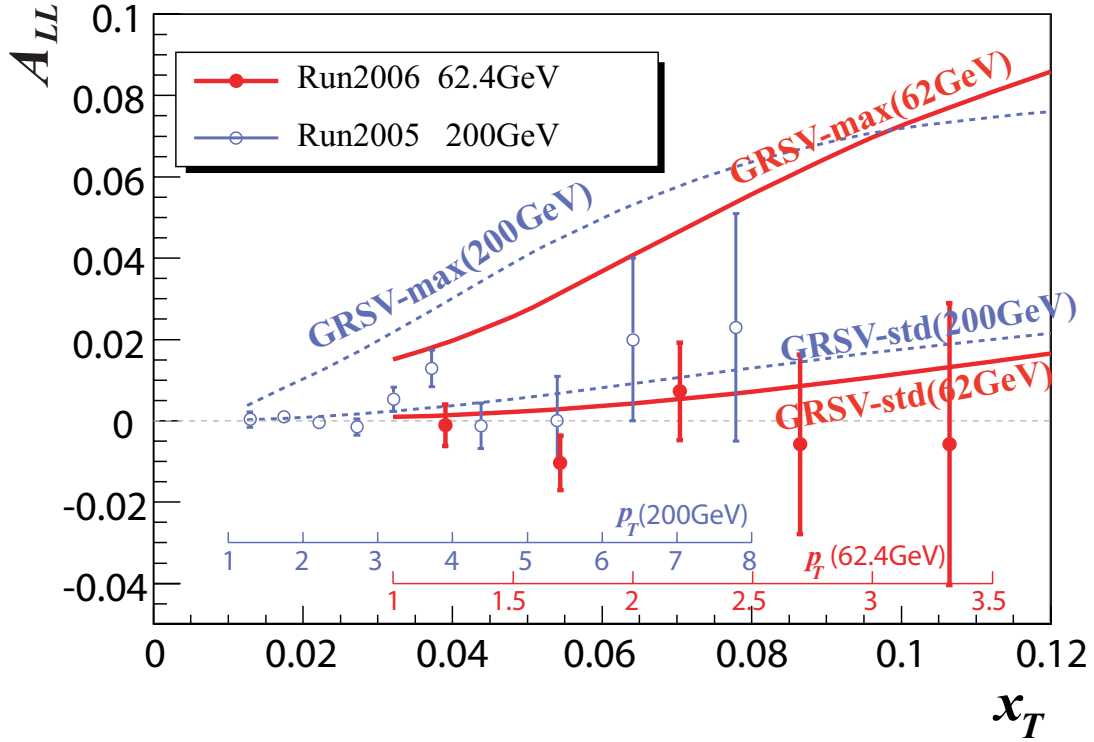


Figure 5.3: Double helicity asymmetries for neutral pion production at $\sqrt{s} = 62.4$ GeV and 200 GeV as functions of x_T . Error bars are statistical uncertainties, with the 14% (9.4%) overall polarization uncertainty for $\sqrt{s} = 62.4$ GeV (200 GeV) data which are not shown. Two GRSV theoretical calculations based on NLO pQCD are also shown for comparison with the data (see text for details.)

rewriting it as

$$A_{LL} \sim \frac{1}{\sigma} (\Delta g \Delta g \cdot \hat{a}_{LL}^{gg} \hat{\sigma}^{gg} + \Delta g \Delta q \hat{a}_{LL}^{gq} \hat{\sigma}^{gq} + \Delta q \Delta q \hat{a}_{LL}^{qq} \hat{\sigma}^{qq}), \quad (5.1)$$

where Δg and Δq are the polarized PDFs for gluons and quarks respectively, and \hat{a}_{LL} ($\hat{\sigma}$) are the partonic A_{LL} (cross sections) for processes indicated by the superscripts. The fragmentation functions were omitted for simplicity. It is a quadratic equation in terms of Δg and it makes A_{LL} not sensitive to the sign of Δg . (According to pQCD calculations, contribution of qg exceeds that from gg for $p_T > 2$ GeV/ c (3 GeV/ c) at $\sqrt{s} = 62.4$ GeV (200 GeV) and thus high p_T A_{LL} have some sensitivity to the sign.)

AAC is the first polarized PDF analysis group to add uncertainty on PDF results. Assignment of uncertainties on PDFs is not straight forward since some of the experimental uncertainties are correlated. PDF analysis is based on various experimental observables

p_T [GeV/c]	$\langle p_T \rangle$ [GeV/c]	background ratio	$A_{LL}^{\pi^0}$
1.0 – 1.5	1.21	0.35	$(-1.1 \pm 5.1) \times 10^{-3}$
1.5 – 2.0	1.70	0.17	$(-10. \pm 6.7) \times 10^{-3}$
2.0 – 2.5	2.20	0.10	$(0.7 \pm 1.2) \times 10^{-2}$
2.5 – 3.0	2.70	0.056	$(-0.6 \pm 2.2) \times 10^{-2}$
3.0 – 4.0	3.32	0.041	$(-0.6 \pm 3.5) \times 10^{-2}$

Table 5.1: Results for $\pi^0 A_{LL}$.

Data sets	ΔG
DIS only	0.47 ± 1.1
DIS + 62.4 GeV	0.26 ± 0.39
DIS + 200 GeV	0.37 ± 0.40
DIS + 62.4 GeV + 200 GeV	0.26 ± 0.31

Table 5.2: AAC results of the first moment of the polarized gluon PDFs obtained with various data sets.

from different experimental groups and treating correlated uncertainties in mathematically correct way is very difficult. Therefore, the statistical and systematic uncertainties are added in quadrature, and all uncertainties are treated as uncorrelated, which overestimates the uncertainties. This also applies for DSSV analysis described in the next section. AAC utilized Hessian method to assign uncertainty. It determines the uncertainty from the dependence of χ^2 near its global minimum based on a Taylor expansion and keeping only the leading term. This assumes a quadratic form in the displacements of all parameters from their optimum values. On the other hand, Lagrange multiplier method, which is used by DSSV described in the next section, does not use the assumption. It was recently realized that the Hessian method tends to produce slightly larger uncertainty compared to the Lagrange multiplier method for polarized gluon distribution. Therefore, the uncertainty by AAC and DSSV cannot be compared directly, but the uncertainties by the same group can be directly compared and discussed.

We only show positively polarized gluon solution in Fig. 5.4 since a negatively polarized gluon solution is not available. The black curve shows the polarized gluon PDF ($xg(x)$) and its uncertainty obtained with DIS data only. It has a huge uncertainty as in the figure. The blue curve and the blue shaded area show $xg(x)$ and its uncertainty when the results of $\pi^0 A_{LL}$ at $\sqrt{s} = 62.4$ GeV are added in addition to the DIS data sets. Significant improvement in the uncertainty, and slight decrease in the central value can be observed. The figure is one of the proofs of the fact that the polarized pp collisions work as a powerful tool to investigate the gluon polarization inside the proton. For the

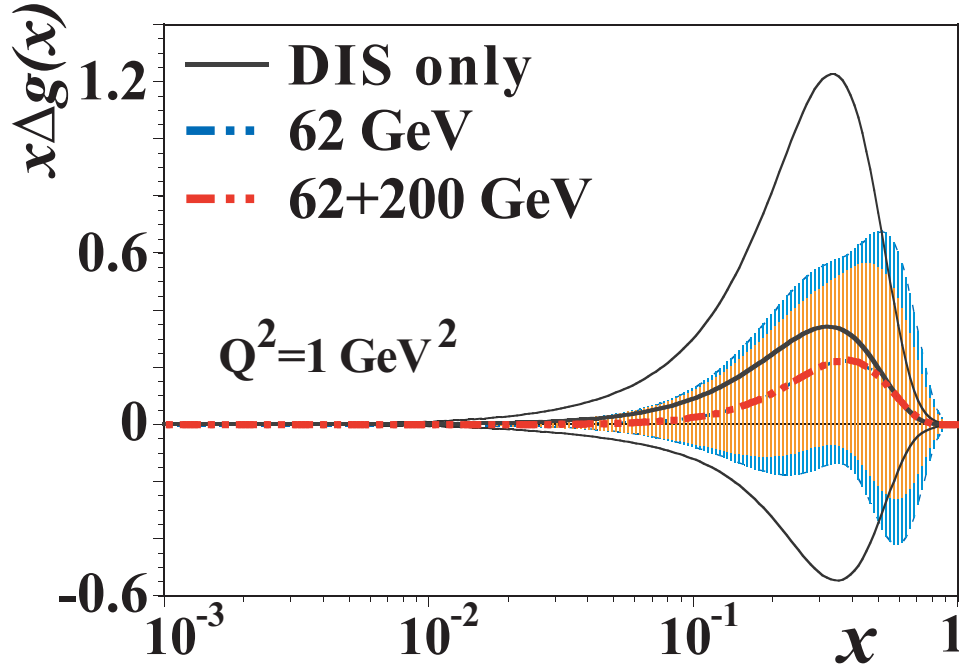


Figure 5.4: AAC results of the polarized gluon PDF. The black curves show the central value and the uncertainties of the pol-gluon PDF obtained with DIS data sets only. The blue curve and the shaded area shows the PDF obtained with DIS and 62.4 GeV data. The red curve and the shaded area shows the results obtained with DIS, 62.4 GeV and 200 GeV data. The blue and the red lines are overlapped.

red curve and the red shaded area, the results of $\pi^0 A_{LL}$ at $\sqrt{s} = 200$ GeV in Run 2005 are also added. The uncertainty slightly decreased but the central shape does not show significant change from the one with $\sqrt{s} = 62.4$ GeV data. The first moments of gluon polarizations with the various data sets are summarized in Table 5.2.

5.3.2 DSSV global analysis

The DSSV group included the preliminary version of our results in their global analysis [97]. It also includes PHENIX $\pi^0 A_{LL}$ preliminary results at $\sqrt{s} = 200$ GeV in Run 2006 [98], STAR jet A_{LL} [22] preliminary results, and semi-inclusive DIS data which is sensitive to the flavor decomposition of the quark spin. Some authors of the DSSV group were involved in GRSV, whose results are compared with our measurements in Sec. 5.2. Their polarized gluon PDF is shown in Fig. 5.5. The green band represent the uncertainty of the PDF at the level of $\Delta\chi^2 = 1$, and the yellow band corresponds to that at the level of $\Delta\chi^2/\chi^2 = 2\%$. In unpolarized PDF analysis, it is customary to assign uncertainties

with $\Delta\chi^2/\chi^2 = 2\%$ or 5% to account for large χ^2 which may come from theoretical uncertainties or unaccounted experimental uncertainties. Therefore, uncertainty corresponds to $\Delta\chi^2/\chi^2 = 2\%$ is also provided. (The 2% increase in χ^2 roughly corresponds to 2.8σ in this case since the χ^2 of the fit is $\chi^2 = 392.6$ with $\text{DOF} = 441$.)

The first moment of the DSSV best fit, and the integrals truncated at $x_{\min} = 0.001$ with uncertainties at the levels of $\Delta\chi^2 = 1$ and $\Delta\chi^2/\chi^2 = 2\%$ in Table 5.3. Below $x_{\min} = 0.001$, there is no constraining data set. Therefore, the deviation between the full and the truncated integral is from extrapolation to $x = 0$.

In Fig. 5.5, GRSV-max, GRSV-std and GRSV-min ($\Delta G = -G$), which are introduced in Sec. 5.2, are overplotted for $x\Delta g(x)$. The central value and uncertainty of DSSV $\Delta g(x)$ is smaller than the GRSV-std, which is the best fit in GRSV. And the uncertainty is considerably smaller compared to the allowed range of GRSV parametrization.

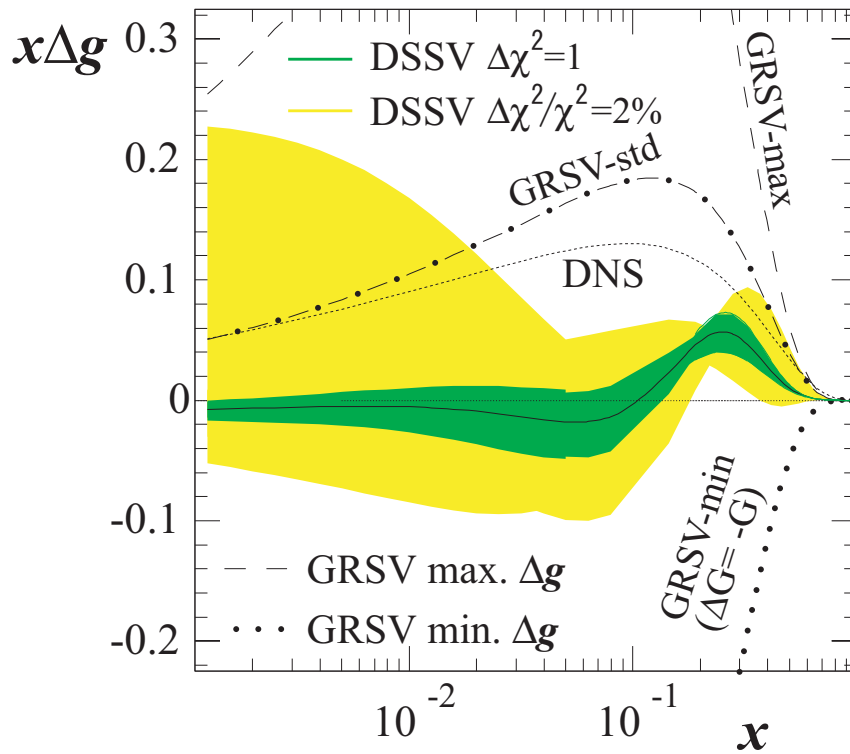


Figure 5.5: DSSV polarized PDFs. The green bands correspond to $\Delta\chi^2 = 1$ and the yellow bands correspond to $\Delta\chi^2/\chi^2 = 2\%$.

Figure 5.6 displays $\Delta g/g$ obtained by the DSSV together with that extracted from Semi-inclusive DIS (SDIS) experiments by SMC [7], HERMES [5, 6], and COMPASS [9]. The SDIS results are extracted at LO and are based on Monte Carlo simulations, while the DSSV results since the DSSV are extracted at NLO. Therefore, they cannot be directly

	$x_{min} = 0$	$x_{min} = 0.001$		
	best fit	$\Delta\chi^2 = 1$	$\Delta\chi^2/\chi^2 = 2\%$	
$\Delta u + \Delta\bar{u}$	0.813	0.793	$+0.011$ -0.012	0.793 $+0.028$ -0.034
$\Delta d + \Delta\bar{d}$	-0.458	-0.416	$+0.011$ -0.009	-0.416 $+0.035$ -0.025
$\Delta\bar{u}$	0.036	0.028	$+0.021$ -0.020	0.028 $+0.059$ -0.059
$\Delta\bar{d}$	-0.115	-0.089	$+0.029$ -0.029	-0.089 $+0.090$ -0.080
$\Delta\bar{s}$	-0.057	-0.006	$+0.010$ -0.012	-0.006 $+0.028$ -0.031
Δg	-0.084	0.013	$+0.106$ -0.120	0.013 $+0.702$ -0.314
$\Delta\Sigma$	0.242	0.366	$+0.015$ -0.018	0.366 $+0.042$ -0.062

Table 5.3: The first moments of DSSV PDFs, $\int_{x_{min}}^1 \Delta f(x)$ at $Q^2 = 10 \text{ GeV}^2$.

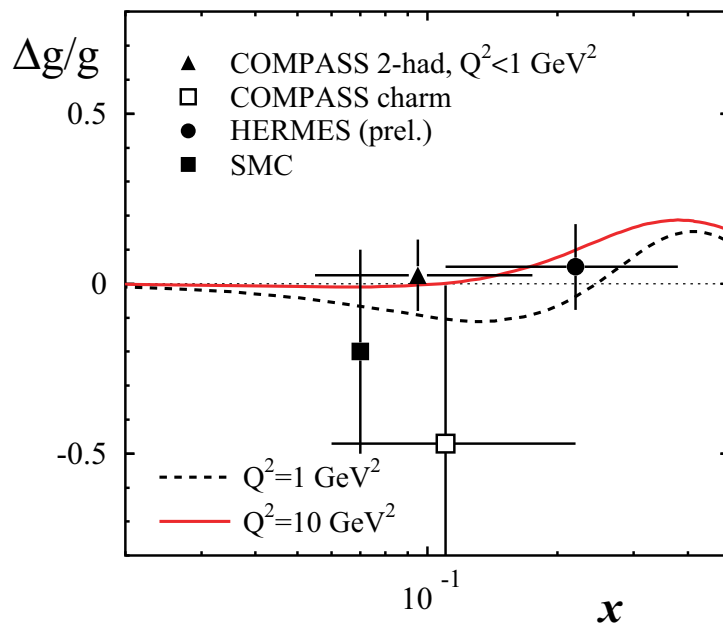


Figure 5.6: Comparison of $\Delta g/g$ obtained by the DSSV group with extracted $\Delta g/g$ from photon-gluon fusion by SMC, HERMES, and COMPASS.

compared with each other. NLO calculations for these processes are still not available and these data are not included in the DSSV analysis.

5.4 Further study on the spin structure of the proton

PHENIX have published the results of $\pi^0 A_{LL}$ (Run 2003 [13], Run 2004 [14], Run 2005 [15, 16]) at $\sqrt{s} = 200$ GeV, and $\pi^0 A_{LL}$ at $\sqrt{s} = 62.4$ GeV [75] (Run 2006, which this thesis is based on). Recently PHENIX published $\pi^0 A_{LL}$ at $\sqrt{s} = 200$ GeV extracted from the data collected in Run 2006 [98]. It was demonstrated that $\pi^0 A_{LL}$ at $\sqrt{s} = 62.4$ GeV [75] alone gave significant constraint on Δg . DSSV performed global analysis including this data, together with the results of $\pi^0 A_{LL}$ at $\sqrt{s} = 200$ GeV [98], and jet A_{LL} [22, 99] provided by STAR, and obtained new set of PDFs with much smaller uncertainty than the previously allowed range of Δg .

A_{LL} of π^0 with higher statistics will add further constraint on Δg thus accumulating data is one of the important effort which should be made. In Run 2009, we plan to collect data with integrated luminosity of about 50 pb^{-1} at $\sqrt{s} = 200$ GeV which is three times larger statistics than that in Run 2006. In addition, we have a plan to take data at $\sqrt{s} = 62.4$ GeV in Run 2010. These data are expected to reduce the uncertainty for the sensitive x range ($0.02 < x_g < 0.4$). Figure 5.7 displays the uncertainty of Δg obtained by the DSSV group (Fig. 5.7 top) and expected uncertainties when RHIC Run 2009 data are added (Fig. 5.7 bottom).

However, the large uncertainty of 1st moment comes from lower x where no measurement exists. Collecting data at $\sqrt{s} = 500$ GeV will extend the lower limit of the x range by a factor of about 2.5. An order of smaller x range can be investigated via A_{LL} of J/ψ detected with the forward muon spectrometers of PHENIX. However, the production mechanism of J/ψ is still not well understood. The mechanism should be studied to extract information on Δg . Lower x range, down to a few times 10^{-4} , can be investigated with a future facility called e-RHIC [100]. e-RHIC will be the world's first polarized electron-proton DIS collider which consists of the existing polarized proton ring at RHIC and an electron ring which will be installed. Electron energy of 10 GeV and proton energy of 250 GeV are expected. At low x , the logarithmic derivative of the structure function g_1 in Q^2 is proportional to the negative of Δg .

A_{LL} of other final state observables such as $\pi^{+,-}$ [18, 19], and direct photon [20, 21] are also important since those have different systematics compared to π^0 . The gg process which hides the sign of Δg is common in π^+ and π^- . Therefore, the difference is more sensitive to the sign of Δg than π^0 . Direct photon production is dominated by $qg \rightarrow q\gamma$ process and is sensitive to the sign of Δg . Luminosity growth of RHIC and the acceptance extension by the PHENIX detector upgrade with Silicon Vertex Tracker (SVT) provide information on x dependence of Δg via two particle correlations such as γ +jet. (γ is detected with EMCAL and jet is detected with SVT.)

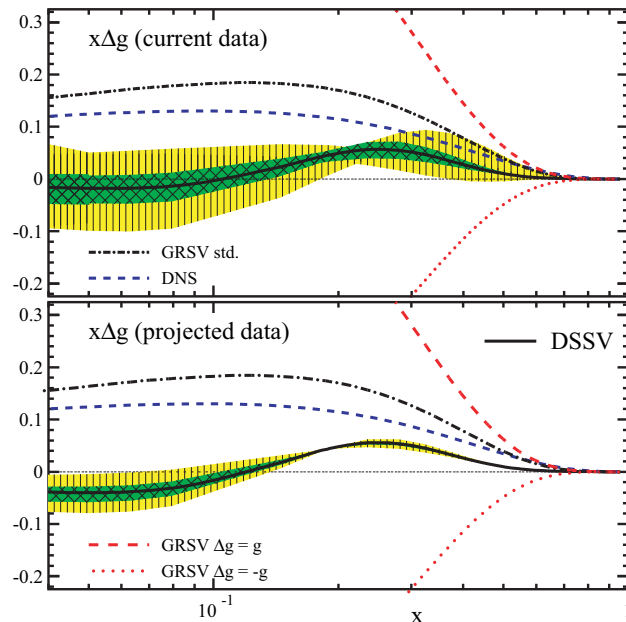


Figure 5.7: Upper panel: $x\Delta g$ at $\mu^2 = 10\text{GeV}^2$ from the NLO global analysis by DSSV [97], which includes RHIC Run 2005 data at $\sqrt{s} = 200\text{ GeV}$ and $\sqrt{s} = 62.4\text{ GeV}$. The green band corresponds to $\Delta\chi^2 = 1$ and the yellow band shows $\Delta\chi^2/\chi^2 = 2\%$. Lower panel: Expected uncertainty band with RHIC Run 2009 at $\sqrt{s} = 200\text{ GeV}$ (50 pb^{-1} with a polarization of 60%.)

It is still possible that ΔG explains the missing piece of proton spin but the missing piece might not be fully explained by the gluons. The other candidate and only one left is the orbital angular momentum (OAM) of partons. Siverson function, which is a correlation between a parton's transverse momentum and the proton spin vector, contains information of OAM in the proton. The gluon Siverson function can be accessed via transverse single spin asymmetries of pions and D meson production in pp collisions [101, 102].

The polarized sea quark distributions are also not well determined. It can be studied with W boson production in polarized pp collisions at $\sqrt{s} = 500\text{ GeV}$. The integrated luminosity of about 300 pb^{-1} is expected to be achieved by Run 2013 and $\sim 3000\text{ }W^+$ events and $\sim 3000\text{ }W^-$ events are expected to be collected.

Chapter 6

Conclusion

We have measured double helicity asymmetry A_{LL} of inclusive mid-rapidity π^0 production in polarized pp collisions at $\sqrt{s} = 62.4$ GeV. Its kinematical coverage was $p_T = 1-4$ GeV/ c and $|\eta| < 0.35$. It is sensitive to gluon polarization in the proton since gluon interacts at leading order in π^0 production in polarized pp collisions. In addition to A_{LL} , single helicity asymmetry A_L , and double transverse spin asymmetry A_{TT} have been measured. We have also presented the unpolarized cross section, obtained from the same data set.

The experiment was performed with the PHENIX detector, with the polarized proton beams provided by RHIC at BNL in the United States. The data used in this thesis were taken from Jun. 6 to 20 (two weeks) during Run 2006. The analyzed data sample has the integrated luminosity of 40 nb^{-1} , with average polarization of 48%. π^0 production was measured through its two photon decay mode. The photons were detected by the PHENIX EMCal. High- p_T photon trigger which is constructed by the signals from EMCal was used to collect the data sample. The measured A_{LL} are consistent with zero within statistical uncertainties. Major source of the systematic uncertainty is the scale uncertainty of 14% which comes from the beam polarizations. Double transverse spin asymmetry A_{TT} was also measured to obtain the systematic uncertainty from the residual transverse components of the beam polarizations. The maximal possible A_{TT} effect on A_{LL} was obtained to be $< 0.15 \cdot \delta A_{LL}$ in all p_T bins, where δA_{LL} denotes the statistical uncertainty of A_{LL} . Single spin asymmetry A_L , which is expected to be negligible at this energy, was measured for diagnostics and is consistent with zero within the statistical uncertainties. Other systematic uncertainties are small compared to the statistical uncertainty, which is confirmed by a technique to randomize the sign of bunch crossing polarization.

Comparisons of unpolarized cross section results to NLO and NLL theoretical calculations were performed. NLO and NLL agree with the data within theoretical uncertainties. Therefore, the data can be interpreted in pQCD framework to obtain information of Δg .

The A_{LL} results extend the sensitivity to the polarized gluon distribution in the proton to higher x_g compared to the previous measurements at $\sqrt{s} = 200$ GeV. AAC and

DSSV global analyses show that our data have strong constraint power on Δg beyond the traditional polarized DIS data. The data do not support a large gluon scenario, such as GRSV-max. An NLO global pQCD analysis by DSSV group included the present data in this thesis, and obtained an integral of $\Delta g(x)$ to be $\int_{0.001}^1 \Delta g(x) dx = 0.013_{-0.120}^{+0.106}$ for $\Delta\chi^2 = 1$ and $0.013_{-0.314}^{+0.702}$ for $\Delta\chi^2/\chi^2 = 2\%$ at $\mu^2 = 10 \text{ GeV}^2$. The uncertainty was significantly reduced compared to what is obtained with polarized DIS data only. For more precise determination of Δg , it is important to accumulate more data. In Run 2009, we plan to collect data with integrated luminosity of 25 pb^{-1} at $\sqrt{s} = 200 \text{ GeV}$ with beam polarizations of 65%. We also plan to take data at $\sqrt{s} = 62.4 \text{ GeV}$ in Run 2010. These data are expected to reduce the uncertainty and provide us further information on the spin structure of the proton.

Acknowledgments

I would like to express profound gratitude to Dr. Ken'ichi Imai, who is the leader of the experimental Nuclear and Hadronic physics group (NH). His words were always full of passion for physics and I felt deep understanding of nature inside him that always stimulated my work. He has read my thesis carefully and given me useful suggestions. I am deeply grateful to Dr. Naohito Saito, who has been my supervisor. I learned not only physics but also scientific approach through discussions and every day conversations. He has read my thesis thoroughly and the discussion with him was vital in completing the thesis.

I cannot thank enough Dr. Yuji Goto who was the tutor at BNL. I would like to express my gratitude to the members of π^0 working group: Dr. Alexander Bazilevsky and Dr. Kieran Boyle. Discussion with them was beneficial and I was able to polish the analysis working with them. I would like to thank Dr. Hideto Enyo who is the chief scientist of Radiation Laboratory at RIKEN for his support. I also would like to thank the members of RIKEN BNL Research Center (RBRC): Dr. Yasuyuki Akiba, Dr. Gerry Bunce, Dr. Abhay Deshpande, and Dr. Kensuke Okada. I would like to thank the PHENIX collaborators, and the staff of Collider Accelerator Department at BNL. Without them the experiment would not be possible.

I would like to thank the members of the paper preparation group (PPG087): Dr. Ken Barish, Dr. Alexander Bazilevsky, Dr. Robert Bennett, and Dr. Yuji Goto. I also would like to thank the members of the internal review committee (IRC087): Dr. Ed Kinney, Dr. Vassili Papavassiliou, and Dr. Henner Buesching.

I always enjoyed working and discussing with Dr. Manabu Togawa during my stay at BNL. I learned a lot about physics and PHENIX-related matters. I also learned how to cook miso soup from him. I would like to thank Dr. Yoshinori Fukao and Dr. Kenichi Nakano. Discussion with them was helpful in writing the thesis. I would like to thank the staff of the NH group: Dr. Tomofumi Nagae, Dr. Tetsuya Murakami, and Dr. Kiyoshi Tanida. I also would like to thank colleagues from the NH group: Dr. Hiromi Inuma, Mr. Kohei Shoji, Mr. Seishi Dairaku, Mr. Kenichi Karatsu, and Mr. Katsuro Nakamura.

I would like to thank the administrators of the PHENIX Computing Center in Japan (CCJ): Dr. Yasushi Watanabe, Dr. Satoshi Yokkaichi, Dr. Soichiro Kametani, Dr. Tomoaki Nakamura. The analysis was done on CCJ and it was very effective with their

supports.

I would like to thank Dr. Werner Vogelsang, Dr. Marco Stratmann, and Dr. Masanori Hirai who has kindly provided theoretical calculations.

Appendix A

z -dependent BBC-efficiency

A.1 Overview

The procedure to obtain z (vertex position)-dependent BBC-efficiency is explained in this section. The procedure used for the data at $\sqrt{s} = 62.4$ GeV (which the thesis is based on) is explained and the results are presented in this chapter.

A.2 z -dependent BBC-efficiency at $\sqrt{s} = 62.4$ GeV

A.2.1 Procedure with WCM and vernier scan

The collision vertex distribution at PHENIX IP is calculated with the beam profiles of the Blue and the Yellow beams. Then it is compared with the measured vertex distribution with BBC at PHENIX and BBC efficiency is found.

The collision vertex distribution at PHENIX IP is calculated as

$$V(z) \propto \int \int \int dx dy dt D^B(x, y, z, t) \cdot D^Y(x, y, z, t), \quad (\text{A.1})$$

where D^B and D^Y are the beam densities for the Blue and the Yellow beams, respectively. The beam densities can be written as

$$D^B(x, y, z, t) = D_x^B(x) \cdot D_y^B(y) \cdot D_z^B(z - ct), \quad (\text{A.2})$$

for the Blue beam, and

$$D^Y(x, y, z, t) = D_x^Y(x) \cdot D_y^Y(y) \cdot D_z^Y(z + ct), \quad (\text{A.3})$$

for the Yellow beam. Transverse beam profiles are measured by the van der Meer technique or the vernier scan. In a vernier scan, the transverse widths of the beam overlap σ_x, σ_y

are measured by sweeping one beam across the other in small steps while monitoring the BBC trigger rate. Figure A.1 displays the horizontal and the vertical beam profiles. (Each plot has four points at zero since a scan starts from zero and go back to zero when a scan in one direction was finished.) The obtained profiles are well reproduced by Gaussians, thus $D_x(x)$, and $D_y(x)$ are written as

$$D_x(x) = \frac{1}{\sigma_x \sqrt{2\pi}} \exp\left(-\frac{(x - x_0)^2}{2\sigma_x^2}\right), \quad (\text{A.4})$$

$$D_y(x) = \frac{1}{\sigma_y \sqrt{2\pi}} \exp\left(-\frac{(y - y_0)^2}{2\sigma_y^2}\right), \quad (\text{A.5})$$

$$(\text{A.6})$$

where σ_x and σ_y are the widths of transverse beam profiles. The hour glass effect is taken into account by changing the widths as

$$\sigma_{x(y)}^2(z) = \sigma_{x(y)}^2 \cdot \left(1 + \frac{z^2}{\beta^{*2}}\right), \quad (\text{A.7})$$

where β^* is beam focusing parameter. The longitudinal beam profiles were measured with Wall Current Monitors (WCMs) as in Fig. A.2.

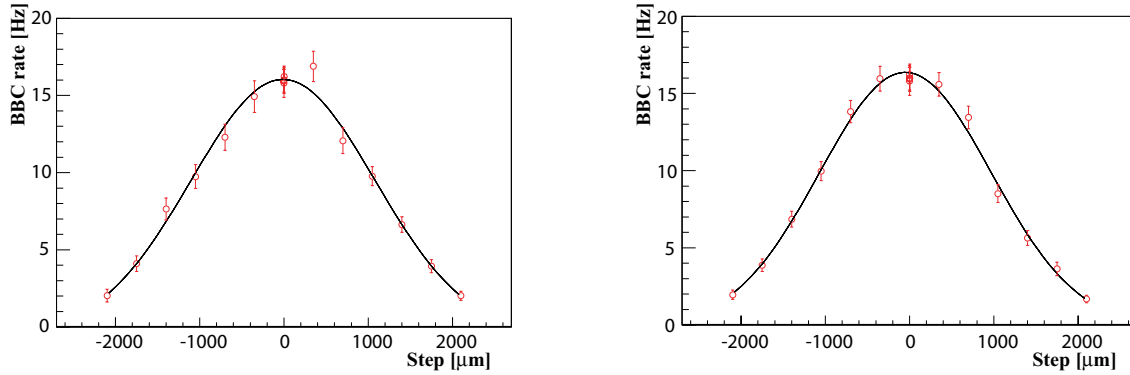


Figure A.1: Horizontal (Left) and vertical (right) beam profiles measured with the vernier scan. The horizontal axis shows the step size of the beam displacement in μm . The vertical axis is the BBC trigger rate.

A.2.2 Results at $\sqrt{s} = 62.4$ GeV

The vertex distribution was simulated according to Eq. A.1, using the information explained above. The BBC vertex resolution of $\sigma_z^{BBC} = 2$ cm was used in the simulation.

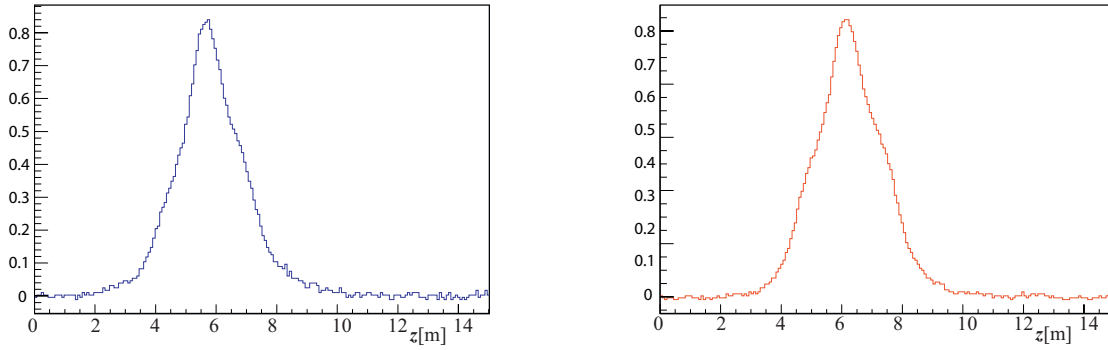


Figure A.2: Longitudinal beam profile measured with WCM for the Blue (Left) and for the Yellow (Right) beams.

The z -dependence of BBC efficiency is well represented as a Gaussian with a width of σ_{eff}^{BBC} . Figure A.3 displays the vertex distribution measured with BBC overlapped with the simulated results. The three plots show how the distribution changes with different σ_{eff}^{BBC} in the simulations. The left plot was with $\sigma_{eff}^{BBC} = 85$ cm, and the middle was with $\sigma_{eff}^{BBC} = 95$ cm, and the right was with $\sigma_{eff}^{BBC} = 105$ cm. As shown in the figure, the distribution is sensitive to the BBC efficiency. The z -dependent BBC efficiency was obtained to be $\sigma_{eff}^{BBC} = 95 \pm 10$ cm ($\Delta\chi^2 = 9$).

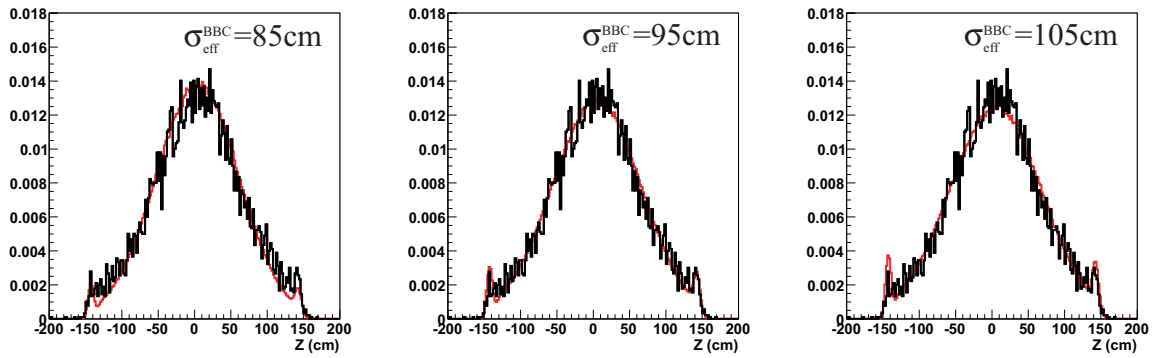


Figure A.3: Comparison of the z vertex distributions measured with BBC (Black) and calculated with monte carlo (Red) for $\sigma_{eff}^{BBC} = 85$ cm, $\sigma_{eff}^{BBC} = 95$ cm, $\sigma_{eff}^{BBC} = 105$ cm(right). The calculation for $\sigma_{eff}^{BBC} = 95$ cm is most compatible with the measured distribution.

Appendix B

EMC clustering algorithm

B.1 PbSc

In PbSc, instead of summing all of the energies deposited in towers in a cluster, the sum is performed only for the core towers as explained in Sec. 4.5.2. Then the core tower energy E^{core} was corrected to obtain the cluster energy E_{corr}^{core} . The correction was divided into three pieces. One is the correction from core energy to cluster energy, which is dependent on the incident angle of the photon. The function used for the correction is,

$$E_{\text{angle-corr}}^{core} = \frac{E^{core}}{a(1 - b \sin^4(\theta) \times (1 - c \cdot \log(E^{core})))}, \quad (\text{B.1})$$

$$a = 0.918, \quad (\text{B.2})$$

$$b = 1.35, \quad (\text{B.3})$$

$$c = 0.003, \quad (\text{B.4})$$

where E^{core} is the core energy of the target cluster, θ is the impact angle of the incident photon, and $E_{\text{angle-corr}}^{core}$ is the corrected core energy. The parameters a, b and c were obtained with the test experiments. Fig. B.1 displays the correction factor ($C^{clus} = E_{corr}^{core}/E^{core}$). (Although the plot is for $E^{core} = 1$ GeV, the energy dependence is negligible at the energies of interest.) The impact angle θ is less than 24 deg. The core energy is about 90% of the cluster energy, and the angle dependence correction is less than 4%.

The correction factor for shower leakage (C^{leak}) and attenuation in the fibers (C^{att}) are obtained as

$$C^{leak} = \frac{1}{2 - \sqrt{1 + d \cdot \log^2(1 + E_{\text{angle-corr}}^{core})}}, \quad (\text{B.5})$$

$$d = 0.0033, \quad (\text{B.6})$$

$$C^{att} = \frac{1}{\exp(\log(E_{\text{angle-corr}}^{core}) \cdot X_0/\lambda)}, \quad (\text{B.7})$$

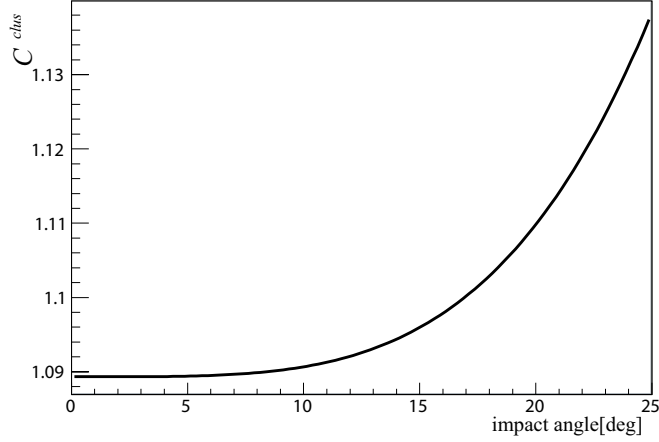


Figure B.1: The correction factor from core energy to cluster energy, including angle dependence, C^{clus} .

$$X_0 = 2 \text{ cm}, \quad (\text{B.8})$$

$$\lambda = 120 \text{ cm} \quad (\text{B.9})$$

where X_0 is the radiation length, and λ is the attenuation length in the fiber. Then the corrected energy E_{corr}^{core} becomes

$$E_{corr}^{core} = C^{leak} C^{att} E_{angle-corr}^{core}. \quad (\text{B.10})$$

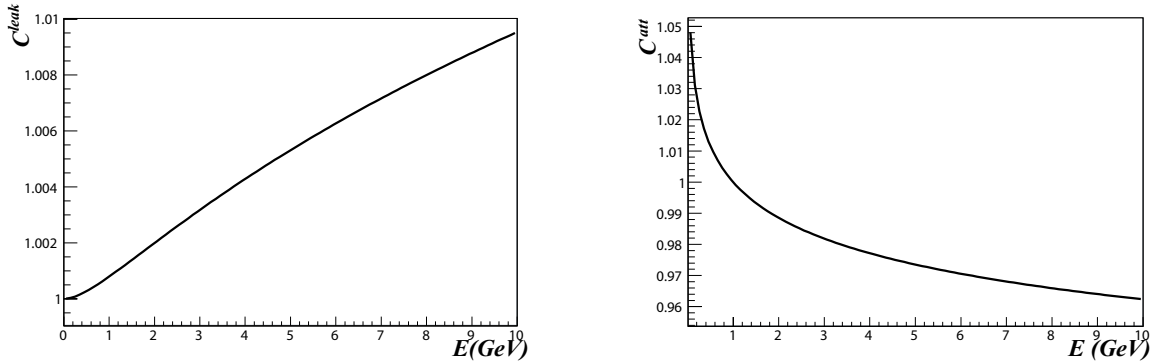


Figure B.2: The correction factors for shower leakage, C^{leak} (Left), and for attenuation in the fibers, C^{att} (Right).

B.2 PbG1

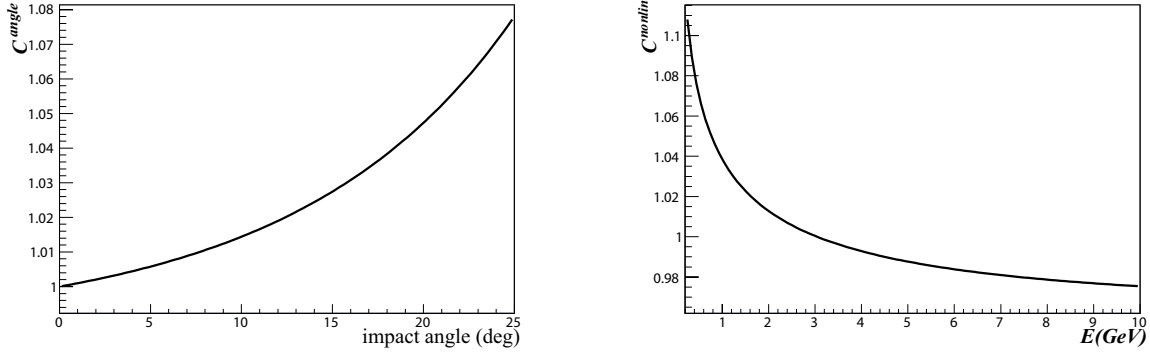


Figure B.3: The correction factors for angle dependence, C^{angle} (Left), and for non-linearity, C^{nonlin} (Right).

The correction factors for angle dependence, C^{angle} and non linearity, C^{nonlin} are calculated as

$$C^{angle} = \frac{1}{a(\exp(b\theta) - 1) + 1}, \quad (\text{B.11})$$

$$a = -0.012043, \quad (\text{B.12})$$

$$b = 0.077908 \cdot 180/\pi, \quad (\text{B.13})$$

and

$$C^{nonlin} = a + b \log(E) + c \log^2(E), \quad (\text{B.14})$$

$$a = 1.0386, \quad (\text{B.15})$$

$$b = -0.041423, \quad (\text{B.16})$$

$$c = 0.006064. \quad (\text{B.17})$$

Then the cluster energy, E , is corrected as

$$E^{corr} = C^{angle} C^{nonlin} E, \quad (\text{B.18})$$

where E^{corr} is the corrected energy of the cluster.

Appendix C

Some information on pol-PDFs

C.1 Q^2 evolutions of parton contributions to the proton spin

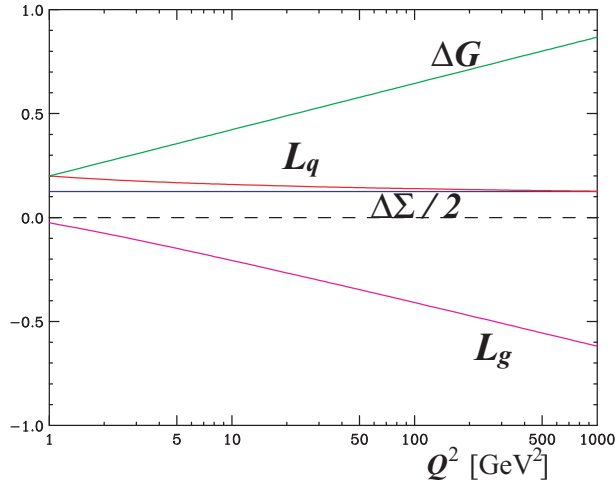


Figure C.1: Toy calculation of the Q^2 evolutions of the contributions to the proton spin at leading order. [103]

Figure. C.1 displays toy calculation of the Q^2 evolutions of the contributions to the proton spin at leading order [103]. $\Delta\Sigma$ is the sum of quark spin contributions, L_q and L_g is the orbital angular momentum of quarks and gluons respectively, ΔG is the gluon spin contribution. The calculation was performed assuming $\Delta\Sigma = 0.25$, $\Delta G = L_q = 0.2$, $L_g = -0.025$ at an initial scale $Q_0 = 1$ GeV. The rise of $\Delta G \propto \log Q^2$ is compensated by an opposite evolution of L_g . At $Q^2 \rightarrow 0$, $\frac{1}{2}\Delta\Sigma + L_q$ and $\Delta G + L_g$ become roughly

equal [104].

C.2 DSSV polarized PDFs

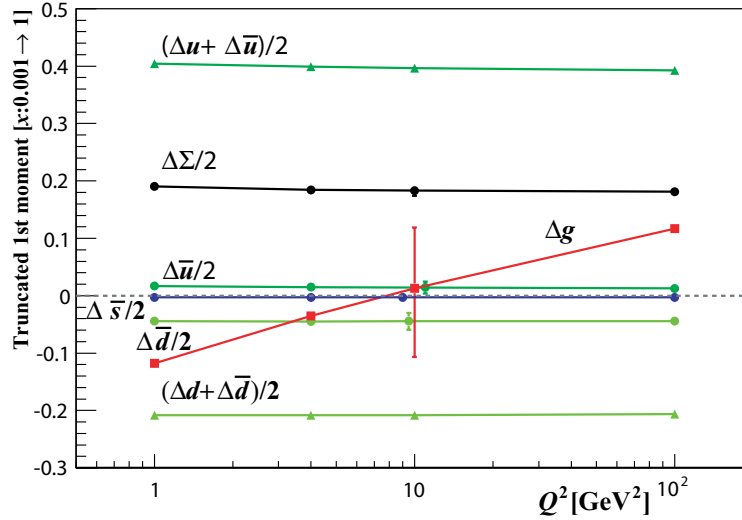


Figure C.2: Truncated 1st moments of polarized PDFs by the DSSV group vs Q^2 . The lines between the points for different Q^2 are straight lines and are drawn only for a guide. Some of the points at $Q^2 = 10 \text{ GeV}^2$ are shifted for clear separations. The uncertainties corresponds to $\Delta\chi^2 = 1$ are only plotted for $Q^2 = 10 \text{ GeV}^2$.

Figure C.2 displays truncated 1st moments of polarized PDFs ($\int_{0.001}^1 dx f(x)$) by the DSSV group.

C.3 GRSV

$Q^2 [\text{GeV}^2]$	Δu	Δd	$\Delta \bar{q}$	Δg	$\Delta \Sigma$
1	0.861	-0.405	-0.063	0.420	0.204
5	0.859	-0.406	-0.064	0.708	0.197
10	0.859	-0.406	-0.064	0.828	0.197

Table C.1: 1st moments of polarized PDFs by the GRSV group [45]. GRSV-std.

$Q^2[\text{GeV}^2]$	GRSV-max	GRSV-std	GRSV-0	GRSV-min
0.4	1.256	0.240	0	-1.256
1	1.894	0.420	0.070	-1.763
4	2.795	0.668	0.160	-2.495

Table C.2: 1st moments of polarized gluon PDFs for various scenarios by the GRSV group [55].

Appendix D

Subprocess cross sections for $gg \rightarrow q\bar{q}$ and $gg \rightarrow gg$

The cross sections of parton parton interactions for center of mass system (CMS) at LO, when they are purely strong interactions, are given by [105],

$$\frac{d\hat{\sigma}}{d\hat{t}} = \frac{\pi\alpha_s^2}{\hat{s}^2} \overline{|M|^2}, \quad (\text{D.1})$$

where \hat{s} , \hat{t} , and \hat{u} (which appears later) are the Mandelstam variables for the parton-parton interactions, $\hat{\sigma}$ is the cross section of interest, α_s is the strong coupling constant, and $\overline{|M|^2}$ is the spin-averaged matrix element squared. The matrix elements for $gg \rightarrow q\bar{q}$ and $gg \rightarrow gg$ are,

$$gg \rightarrow q\bar{q} : \overline{|M|^2} = \frac{9}{64} \cdot \frac{8}{3} \left(\frac{4\hat{u}^2 + \hat{t}^2}{9\hat{u}\hat{t}} - \frac{\hat{u}^2 + \hat{t}^2}{\hat{s}^2} \right) \quad (\text{D.2})$$

$$gg \rightarrow gg : \overline{|M|^2} = \frac{9}{2} \left(3 - \frac{\hat{u}\hat{t}}{\hat{s}^2} - \frac{\hat{u}\hat{s}}{\hat{t}^2} - \frac{\hat{s}\hat{t}}{\hat{u}^2} \right) \quad (\text{D.3})$$

Figure D.1 displays the spin-averaged matrix element squared for these subprocesses as a function of $\cos\theta^*$, where θ^* is the scattering angle at CMS. The cross sections for $gg \rightarrow gg$ is larger than that for $gg \rightarrow q\bar{q}$ by about three orders of magnitude.

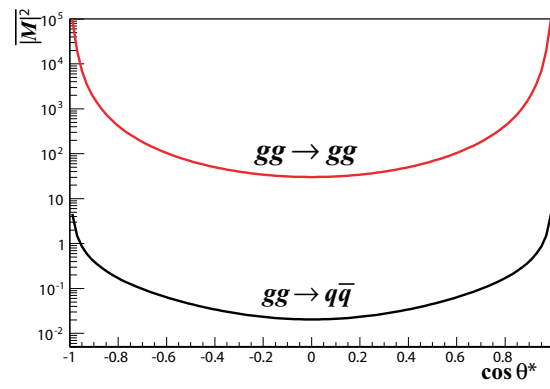


Figure D.1: The spin-averaged matrix element squared $|\overline{M^2}|$ for $gg \rightarrow q\bar{q}$ and $gg \rightarrow gg$.

Bibliography

- [1] J. Ashman *et al.* (European Muon), Phys. Lett. **B206**, 364 (1988).
- [2] J. Ashman *et al.* (European Muon), Nucl. Phys. **B328**, 1 (1989).
- [3] A. Airapetian *et al.* (HERMES), Phys. Rev. **D75**, 012007 (2007), [hep-ex/0609039](#).
- [4] V. Y. Alexakhin *et al.* (COMPASS), Phys. Lett. **B647**, 8 (2007), [hep-ex/0609038](#).
- [5] A. Airapetian *et al.* (HERMES), Phys. Rev. Lett. **84**, 2584 (2000), [hep-ex/9907020](#).
- [6] P. Liebing (HERMES), AIP Conf. Proc. **915**, 331 (2007).
- [7] B. Adeva *et al.* (Spin Muon (SMC)), Phys. Rev. **D70**, 012002 (2004), [hep-ex/0402010](#).
- [8] E. S. Ageev *et al.* (COMPASS), Phys. Lett. **B633**, 25 (2006), [hep-ex/0511028](#).
- [9] M. Alekseev *et al.* (COMPASS) (2008), [0802.3023](#).
- [10] Y. S. Derbenev *et al.*, Part. Accel. **8**, 115 (1978).
- [11] S. Y. Lee, *Spin Dynamics and Snakes in Synchrotrons* (World Scientific, 1997).
- [12] G. Bunce, N. Saito, J. Soffer, and W. Vogelsang, Ann. Rev. Nucl. Part. Sci. **50**, 525 (2000), [hep-ph/0007218](#).
- [13] S. S. Adler *et al.* (PHENIX), Phys. Rev. Lett. **93**, 202002 (2004), [hep-ex/0404027](#).
- [14] S. S. Adler *et al.* (PHENIX), Phys. Rev. **D73**, 091102 (2006), [hep-ex/0602004](#).
- [15] A. Adare *et al.* (PHENIX), Phys. Rev. **D76**, 051106 (2007), [0704.3599](#).
- [16] Y. Fukao (PHENIX), *Ph.D thesis. Double helicity asymmetry for π^0 production in polarized $p + p$ collisions at $\sqrt{s} = 200$ GeV: Implications for the polarized gluon distribution in the proton.* (2007).
- [17] D. G. d'Enterria, J. Phys. **G31**, S491 (2005), [nucl-ex/0411049](#).

- [18] M. Astrid, talk given at the 18th International Spin Physics Symposium (SPIN 2008), University of Virginia, USA. (2008).
- [19] F. Ellinghaus (PHENIX) (2008), [arXiv:0808.4124](#).
- [20] S. S. Adler *et al.* (PHENIX), *Phys. Rev. Lett.* **98**, 012002 (2007), [hep-ex/0609031](#).
- [21] R. Bennett (PHENIX), Talk given at the 18th International Spin Physics Conference (SPIN2008), University of Virginia, USA (2008).
- [22] B. I. Abelev *et al.* (STAR), *Phys. Rev. Lett.* **100**, 232003 (2008), [arXiv:0710.2048](#).
- [23] A. Kocoloski (STAR), *AIP Conf. Proc.* **1149**, 277 (2009), [0905.1033](#).
- [24] F. Halzen and A. D. Martin, *Quarks and Leptons* (Wiley, 1984).
- [25] R. Devenish and A. C-Sarkar, *Deep Inelastic Scattering* (Oxford university press, 2005).
- [26] A. V. Manohar, [hep-ph/9204208](#) (1992).
- [27] J. D. Bjorken, *Phys. Rev.* **179**, 1547 (1969).
- [28] J. Callan, Curtis G. and D. J. Gross, *Phys. Rev. Lett.* **22**, 156 (1969).
- [29] B. Povh, K. Rith, C. Scholz, and F. Zetsche, *Teilchen und Kerne* (Springer, 1994).
- [30] K. Abe *et al.* (E143), *Phys. Rev.* **D58**, 112003 (1998), [hep-ph/9802357](#).
- [31] P. L. Anthony *et al.* (E155), *Phys. Lett.* **B458**, 529 (1999), [hep-ex/9901006](#).
- [32] R. Mertig and W. L. van Neerven, *Z. Phys.* **C70**, 637 (1996), [hep-ph/9506451](#).
- [33] W. Vogelsang, *Phys. Rev.* **D54**, 2023 (1996), [hep-ph/9512218](#).
- [34] G. Sterman, *Nucl. Phys.* **B281**, 310 (1987).
- [35] D. de Florian and W. Vogelsang, *Phys. Rev.* **D71**, 114004 (2005), [hep-ph/0501258](#).
- [36] D. de Florian, W. Vogelsang, and F. Wagner, *Phys. Rev.* **D76**, 094021 (2007), [arXiv:0708.3060](#).
- [37] J. C. Collins *et al.*, *Factorization of Hard Process in QCD in Perturbative Quantum Chromodynamics* (World Scientific, 1989).
- [38] J. Pumplin *et al.*, *JHEP* **07**, 012 (2002), [hep-ph/0201195](#).

- [39] A. D. Martin, R. G. Roberts, W. J. Stirling, and R. S. Thorne, Eur. Phys. J. **C35**, 325 (2004), [hep-ph/0308087](#).
- [40] M. Gluck, E. Reya, and A. Vogt, Eur. Phys. J. **C5**, 461 (1998), [hep-ph/9806404](#).
- [41] S. J. Brodsky and G. R. Farrar, Phys. Rev. Lett. **31**, 1153 (1973).
- [42] C. Amsler *et al.* (Particle Data Group), Phys. Lett. **B667**, 194 (2008).
- [43] M. Hirai, S. Kumano, and N. Saito, Phys. Rev. **D74**, 014015 (2006), [hep-ph/0603213](#).
- [44] M. Hirai, S. Kumano, and N. Saito (Asymmetry Analysis), Phys. Rev. **D69**, 054021 (2004), [hep-ph/0312112](#).
- [45] M. Gluck, E. Reya, M. Stratmann, and W. Vogelsang, Phys. Rev. **D63**, 094005 (2001), [hep-ph/0011215](#).
- [46] E. Leader, A. V. Sidorov, and D. B. Stamenov, Eur. Phys. J. **C23**, 479 (2002), [hep-ph/0111267](#).
- [47] N. Cabibbo, Phys. Rev. Lett. **10**, 531 (1963).
- [48] F. E. Close and R. G. Roberts, Phys. Rev. Lett. **60**, 1471 (1988).
- [49] F. E. Close and R. G. Roberts, Phys. Lett. **B316**, 165 (1993), [hep-ph/9306289](#).
- [50] J. D. Bjorken, Phys. Rev. **148**, 1467 (1966).
- [51] C. Amsler *et al.* (Particle Data Group), Phys. Lett. **B667**, 200 (2008).
- [52] J. Blumlein and H. Bottcher, Nucl. Phys. **B636**, 225 (2002), [hep-ph/0203155](#).
- [53] E. Leader, A. V. Sidorov, and D. B. Stamenov, Phys. Lett. **B462**, 189 (1999), [hep-ph/9905512](#).
- [54] E. Leader, A. V. Sidorov, and D. B. Stamenov, Phys. Rev. **D58**, 114028 (1998), [hep-ph/9807251](#).
- [55] W. Vogelsang, *private communications*.
- [56] A. Zelenski *et al.*, Hyperfine Interactions **127**, 475 (2000).
- [57] P. Sona, Energia Nucleare **14**, 295 (1967).
- [58] L. H. Thomas, Phil. Mag. **3**, 1 (1927).

- [59] V. Bargmann, L. Michel, and V. L. Telegdi, Phys. Rev. Lett. **2**, 435 (1959).
- [60] M. Froissart and R. Stora, Nucl. Instrum. Meth. **7**, 297 (1960).
- [61] T. Roser, AIP Conference Proceedings **187**, 1442 (1988).
- [62] B. W. Montague, Phys. Rep. **113**, 1 (1984).
- [63] O. Jinnouchi *et al.*, RHIC/CAD Accelerator Physics Note **171** (2004).
- [64] H. Okada *et al.*, Phys. Lett. **B638**, 450 (2006), [nucl-ex/0502022](#).
- [65] Y. Fukao *et al.*, Phys. Lett. **B650**, 325 (2007), [hep-ex/0610030](#).
- [66] K. Adcox *et al.* (PHENIX), Nucl. Instrum. Meth. **A499**, 469 (2003).
- [67] M. Allen *et al.* (PHENIX), Nucl. Instrum. Meth. **A499**, 549 (2003).
- [68] C. Adler *et al.*, Nucl. Instrum. Meth. **A470**, 488 (2001), [nucl-ex/0008005](#).
- [69] L. Aphecetche *et al.* (PHENIX), Nucl. Instrum. Meth. **A499**, 521 (2003).
- [70] G. David *et al.*, IEEE Trans. Nucl. Sci. **45**, 705 (1998).
- [71] CERNLIB, *Geant3*.
- [72] M. M. Aggarwal *et al.* (WA98), Phys. Rev. Lett. **81**, 4087 (1998), [nucl-ex/9806004](#).
- [73] M. S. Emery *et al.*, IEEE Trans. Nucl. Sci. **44**, 374 (1997).
- [74] S. S. Adler *et al.* (PHENIX), Nucl. Instrum. Meth. **A499**, 560 (2003).
- [75] A. Adare *et al.* (PHENIX), Phys. Rev. **D79**, 012003 (2009), [arXiv:0810.0701](#).
- [76] C. Amsler *et al.* (Particle Data Group), Phys. Lett. **B667**, 587 (2008).
- [77] S. Arnold, K. Goeke, A. Metz, P. Schweitzer, and W. Vogelsang, Eur. Phys. J. ST **162**, 31 (2008).
- [78] C. Amsler *et al.* (Particle Data Group), Phys. Lett. **B667**, 364 (2008).
- [79] A. L. S. Angelis *et al.* (CERN-Columbia-Oxford-Rockefeller), Phys. Lett. **B79**, 505 (1978).
- [80] C. Kourkoumelis *et al.* (R-806), Phys. Lett. **B84**, 271 (1979).
- [81] A. L. S. Angelis *et al.* (CMOR), Nucl. Phys. **B327**, 541 (1989).

- [82] T. Akesson *et al.* (Axial Field Spectrometer), Sov. J. Nucl. Phys. **51**, 836 (1990).
- [83] C. Kourkoumelis *et al.* (R-806), Zeit. Phys. **C5**, 95 (1980).
- [84] A. G. Clark *et al.* (CSZ), Phys. Lett. **B74**, 267 (1978).
- [85] F. W. Busser *et al.* (CCRS), Nucl. Phys. **B106**, 1 (1976).
- [86] K. Eggert *et al.* (ACHM), Nucl. Phys. **B98**, 49 (1975).
- [87] F. W. Busser *et al.* (CCR), Phys. Lett. **B46**, 471 (1973).
- [88] F. W. Busser *et al.* (CCRS), Phys. Lett. **B55**, 232 (1975).
- [89] M. Banner *et al.* (Saclay), Nucl. Phys. **B126**, 61 (1977).
- [90] B. Alper *et al.* (British-Scandinavian), Nucl. Phys. **B100**, 237 (1975).
- [91] D. de Florian, R. Sassot, and M. Stratmann, Phys. Rev. **D75**, 114010 (2007), [hep-ph/0703242](https://arxiv.org/abs/hep-ph/0703242).
- [92] H. Torii (PHENIX), *Ph.D thesis. Midrapidity Neutral-Pion Production in Proton-Proton Collisions at $\sqrt{s} = 200$ GeV* (2004).
- [93] S. S. Adler *et al.* (PHENIX), Phys. Rev. Lett. **91**, 241803 (2003), [hep-ex/0304038](https://arxiv.org/abs/hep-ex/0304038).
- [94] P. Aurenche, M. Fontannaz, J. P. Guillet, B. A. Kniehl, and M. Werlen, Eur. Phys. J. **C13**, 347 (2000), [hep-ph/9910252](https://arxiv.org/abs/hep-ph/9910252).
- [95] B. Jager, A. Schafer, M. Stratmann, and W. Vogelsang, Phys. Rev. **D67**, 054005 (2003), [hep-ph/0211007](https://arxiv.org/abs/hep-ph/0211007).
- [96] M. Hirai, *private communications*.
- [97] D. de Florian, R. Sassot, M. Stratmann, and W. Vogelsang, Phys. Rev. Lett. **101**, 072001 (2008), [arXiv:0804.0422](https://arxiv.org/abs/0804.0422).
- [98] A. Adare *et al.* (PHENIX), Phys. Rev. Lett. **103**, 012003 (2008), [arXiv:0810.0694](https://arxiv.org/abs/0810.0694).
- [99] D. Staszak (STAR), Nucl. Phys. **A827**, 210c (2009), [arXiv:0902.1345](https://arxiv.org/abs/0902.1345).
- [100] C. Aidala *et al.*, *A high luminosity, high energy electron-ion-collider (erhic white paper)* http://www.phenix.bnl.gov/WWW/publish/abhay/Home_of_EIC/NSAC2007/070424_EIC.pdf (2007).
- [101] M. Anselmino, U. D'Alesio, S. Melis, and F. Murgia, Phys. Rev. **D74**, 094011 (2006), [hep-ph/0608211](https://arxiv.org/abs/hep-ph/0608211).

- [102] M. Anselmino, M. Boglione, U. D'Alesio, E. Leader, and F. Murgia, *Phys. Rev.* **D70**, 074025 (2004), [hep-ph/0407100](#).
- [103] M. Stratmann and W. Vogelsang, *J. Phys. Conf. Ser.* **69**, 012035 (2007), [hep-ph/0702083](#).
- [104] X.-D. Ji, J. Tang, and P. Hoodbhoy, *Phys. Rev. Lett.* **76**, 740 (1996), [hep-ph/9510304](#).
- [105] E. Leader, *Spin in Particle Physics* (Cambridge University Press, 2001).